An Investigation into Stability of Palladium-Based Catalysts for Oxygen Reduction

A Thesis Submitted by

Olukemi Adegbola

For the Degree of Doctor of Philosophy

Supervisor: Professor Keith Scott

School of Chemical Engineering and Advanced Materials

Newcastle University

May 2018

Abstract

Although platinum-based catalysts are regarded as the most active and stable catalysts for oxygen reduction reaction (ORR) in the polymer electrolyte membrane fuel cell (PEMFC), platinum's prohibitive cost and scarcity limits its widespread use for commercial applications. Therefore, the cheaper and more available palladium has been extensively researched as an alternative to platinum. Although palladium has also been reported to have a lower stability than platinum under acidic fuel cell conditions, most of the research on palladium-based catalysts have focussed on improving its ORR activity rather than its stability.

In this research, the ORR activity and stability of palladium-based catalysts were studied with a view of enhancing both. Palladium-based catalysts were synthesised by modifying palladium with gold and iridium well as metal oxides such as TiO_2 and WO_3 known to be stable in acid. The catalysts investigated were PdAu/C, Pd_3Au/C, PdIr/C, PdIrAu/C, PdIr/TiO_2-C and PdIr/WO_3-C. The catalysts were evaluated for ORR by voltammetry in a three-electrode cell and were characterised with techniques such as XRD, TEM and XPS to relate their physical properties to their electrochemical behaviour; before and after durability studies.

The catalysts were synthesised using a polyol method with ethylene glycol as a mild reducing agent that yielded small nanoparticles around 5 nm. The electrochemical surface areas obtained were 15.5, 6.2 and 2.5 m^2g^{-1} for the Pd/C, Pd_3Au/C and PdAu/C catalysts respectively. The stability tests indicated that gold-modified PdAu/C and Pd_3Au/C had higher stability than unmodified Pd/C catalyst as they retained 38 %, 31% and 11 % of their initial chronoamperometric currents respectively over a two-hour period.

In comparison to Pd/C, PdIr/C exhibited at least a two-fold increase in stability; measured by the percentage of initial electrochemical surface area (ECSA) retained by the catalysts after potential cycling. *Ex-situ* XPS and TEM analyses after the potential cycling revealed that the alloying interaction between palladium and iridium reduced palladium's surface oxidation and particle agglomeration and hence improved PdIr/C's stability. The use of TiO_2-modified support on palladium-iridium nanoparticles resulted in an enhancement of activity and stability, with PdIr/TiO_2-C having a specific activity of 0.52 $mAcm^{-2}$ and a 61 % ECSA retention; a two- and a three -fold increase compared to PdIr/C's 0.23 $mAcm^{-2}$ and 20 %.

In summary, this study found the modification of palladium nanoparticles with gold and iridium could enhance its ORR stability in acid environment and that a further stability enhancement could be obtained by modifying the carbon support with acid-stable oxides such as TiO_2 and WO_3.

Table of Contents

List of Figures

List of Tables

Symbols and Nomenclature

α   electron transfer coefficient

C   concentration of dissolved oxygen (mol cm^{-3})

D   diffusion coefficient of oxygen (cm^2 s^{-1})

F   Faraday's constant (9.648 x 10^4 $Cmol^{-1}$)

I   overall current density (mA cm^{-2})

i_k kinetic current density (mA cm^{-2})

i_l limiting current density (mA cm^{-2})

i_o exchange current density (mA cm^{-2})

n   number of electrons

η   overpotential (mV)

R   gas constant (8.314 J mol^{-1})

T   temperature (K)

V   kinematic viscosity of electrolyte (cm^2 s^{-1})

Ω   rotation speed (rad s^{-1})

CB   Carbon black

CS Catalyst support

CV Cyclic voltammetry/cyclic voltammogram

ECSA Electrochemical surface area

EDX   Energy dispersive x-ray spectroscopy

EC   Electrocatalyst

HRTEM High resolution transmission electron microscopy

LSV   Linear sweep voltammetry/ linear sweep voltammogram

OCP   Open circuit potential

ORR   Oxygen reduction reaction

PdCOM Commercial sample of 20 % Pd/C

PtCOM Commercial sample of 20 % Pt/C

PEMFC   Polymer electrolyte membrane fuel cell

RDE   Ring disk electrode

RRDE   Rotating ring disk electrode

TEM   Transmission electron microscopy

Vulcan   Vulcan XC72R

XRD   X-ray diffraction

XPS   X-ray photoelectron spectroscopy

Acknowledgments

Chapter 1. Introduction

1.1 Background

Fuel cells are electrochemical devices for the direct conversion of chemical to electrical energy from the chemical reaction of a fuel with oxygen or other oxidizing agents. Fuel cells were first demonstrated in 1839 by Sir William Grove using oxygen, hydrogen with an acid electrolyte and platinum electrodes [1]. Although they have been around for a long time, the current need for more environmentally-friendly energy production has generated intense research interest in fuel cells.

A fuel cell generally consists of an anode and a cathode separated by an electrolyte. The fuel (typically hydrogen but can be hydrocarbons in some fuel cells) is oxidised at the anode while oxygen is reduced at the cathode. The electrons generated from the anode then flow through an external circuit to the cathode [2]. The main types of fuel cells along with their operational characteristics such as the operating temperature, fuel and electrolyte used are listed below in Table 1.

Table 1: Types of fuel cells and some of their properties.

Fuel Cell Type	Fuel	Electrolyte	Operating Temperature (℃)
Alkaline Fuel Cell	Hydrogen	Potassium Hydroxide	40-90
Direct Methanol Fuel Cell	Methanol	Polymer	60-130
Molten Carbonate Fuel Cell	Hydrocarbons	Molten Carbonate such as Lithium or Potassium carbonate	650
Phosphoric Acid Fuel Cell	Hydrogen	Phosphoric Acid	150-200
Polymer Electrolyte Membrane Fuel Cell	Hydrogen	Polymer	40-90
Solid Oxide Fuel Cell	Hydrocarbons	Solid Oxides such as zirconia	800-1000

In comparison with other fuel cells, polymer electrolyte membrane fuel cells (PEMFC) are especially useful in transport and portable power generation as they possess no major moving parts and can operate at relatively low temperatures (less than 100 ℃). Although the large scale commercial use of PEMFCs is highly desirable, the technology is still limited by cost and durability[3].

A PEMFC unit consists of anode, cathode and an electrolyte. The fuel, hydrogen is externally supplied to the anode, while air or oxygen is supplied to the cathode. The anode and cathode are separated by a solid polymer electrolyte which allows the transport of ions across it. The electrolyte is a proton-conducting polymer electrolyte membrane, usually a perfluoro-sulfonic acid polymer such as Nafion® [4]. At the anode, hydrogen is oxidised to generate electrons and protons. Protons migrate through the electrolyte to the cathode while electrons flow from the anode to the cathode through an external circuit to generate current. At the cathode, protons, electrons and oxygen combine to form water[5, 6].

Reactions occurring in a PEMFC are shown below:

Anode reaction, hydrogen oxidation reaction (HOR):

$$H_2 \rightarrow 2H^+ + 2e^- \tag{1.1}$$

Cathode reaction, oxygen reduction reaction (ORR):

$$\frac{1}{2}O_2 + 2H^+ + 2e^- \rightarrow H_2O \tag{1.2}$$

The overall reaction is hydrogen reacting with oxygen to produce water and electricity:

$$H_2 + \frac{1}{2}O_2 \rightarrow H_2O + \text{Electricity} \tag{1.3}$$

1.2 Oxygen Reduction Reaction (ORR)

The direct reduction of oxygen to water is one of the most extensively studied reactions because of its immense importance in many processes including biological systems, electrochemical processes and energy generation [7, 8]. Oxygen reduction reaction is one of the key reactions in PEMFCs. Its slow kinetics results in the use of the expensive platinum-based catalysts for PEMFC operation [9].

Oxygen reduction reaction (ORR) involves the adsorption of oxygen onto the catalyst surface and the rate of breaking the O=O bond depends on the degree of oxygen's interaction with adsorption sites on catalyst surface as well as the rate of electron transfer[10]. The kinetics and

mechanism of the reaction are dependent on electrode properties as well as the presence of other adsorbed species[11]. Despite the extensive research on ORR, the detailed mechanism is still uncertain. Since the reaction involves the overall transfer of 4 electrons, 4 protons as well as the O=O bond cleavage, there are many possible elementary steps and mechanistic routes leading to the formation of different intermediates depending on the nature of electrode, electrolyte and catalyst used [12].

ORR is believed to proceed via two overall pathways; a direct 4-electron pathway and a peroxide 2-electron pathway. The direct 4-electron pathway involves several steps leading to formation of hydroxide ions in an alkaline environment or water in acidic environment [9]. The 2-electron pathway involves the formation of peroxide species which later decompose or undergo further reduction to give water. The main difference between the two reaction pathways is that peroxide species are formed in solution for the 2-electron pathway and this is not case for the direct 4-electron pathway[10].

The possible pathways for ORR in an acidic medium are shown below [13].

Direct 4-electron pathway:

$$O_2 + 4H^+ + 4e^- \rightarrow 2H_2O \qquad\qquad E^0 = 1.23 \text{ V} \qquad\qquad (1.4)$$

The peroxide pathway:

$$O_2 + 2H^+ + 2e^- \rightarrow H_2O_2 \qquad\qquad E^0 = 0.67 \text{ V} \qquad\qquad (1.5)$$
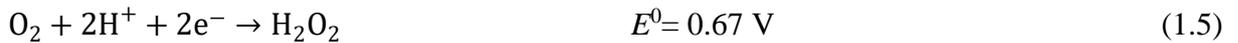
followed either by a further reduction,

$$H_2O_2 + 2H^+ + 2e^- \rightarrow 2H_2O \qquad\qquad E^0 = 1.76 \text{V} \qquad\qquad (1.6)$$

or a decomposition reaction,

$$H_2O_2 \rightarrow 2H_2O + O_2 \qquad\qquad\qquad\qquad (1.7)$$

In comparison, the 2-electron reduction pathway (equation 1.5) has a lower efficiency and also leads to the generation of hydrogen peroxide that can corrode the membrane of the PEMFC[14] ;therefore the 4-electron pathway (equation 1.4) is highly preferred for fuel cell applications. However, the actual reaction pathway followed is dependent on the catalyst used. Reactions using platinum and palladium catalysts are believed to mostly proceed by the direct 4-electron mechanism [15] while ORR with gold and mercury catalysts go via the peroxide forming pathway [16, 17].

During the reaction, interactions of oxygen with the transition metal catalyst surface occur through their molecular orbitals [18]. For platinum, its d orbitals interact with the π orbitals of oxygen involving the donation of electron density from oxygen's lone pairs in the π orbitals to an empty d metal orbital. This is followed by a back-donation of electron density from at least a partially filled d metal orbital to empty anti-bonding π^* orbitals of the oxygen. This platinum-oxygen interaction and the presence of electron density in oxygen's anti-bonding orbitals results in the lengthening and weakening of the O=O bond. Dissociative adsorption of oxygen can occur if the metal-oxygen interaction has an optimal binding energy [17, 19].

According to Norskov *et al.*, the ideal ORR catalyst should be able to bind oxygen with an intermediate strength: not too weakly so oxygen can bind to the catalyst, and not too strongly so products can desorb [20]. This brought about the idea of a volcano-type of relationship between a catalyst's ORR activity and the strength of its bond with oxygen. The group presented a volcano plot (Figure 1) for transition metals based on the metals' ORR activities and their oxygen adsorption energies. Their results showed that platinum, followed by palladium were the metals with the highest activity for ORR since they appear closest to the top of the volcano.
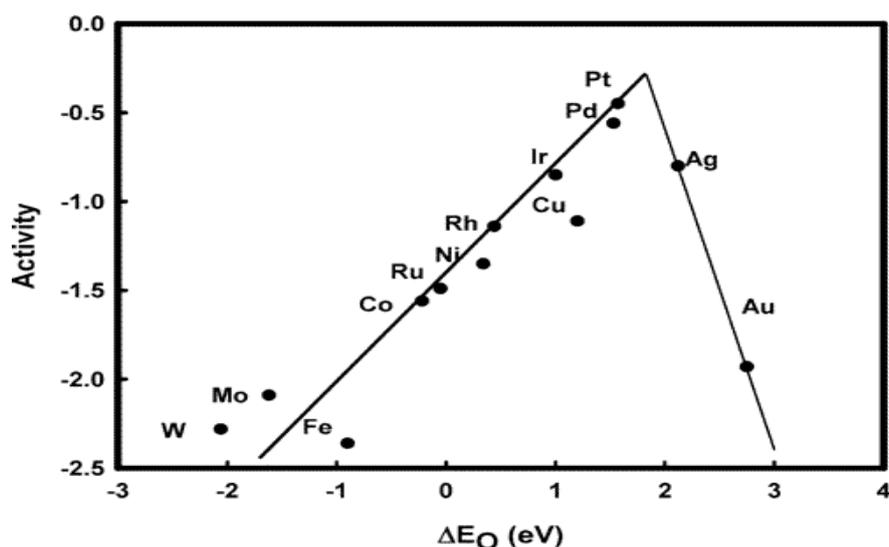
Figure 1: Volcano plot showing trends in ORR activity as a function of oxygen binding energy [20].

1.3 Alternatives to Platinum Catalysts for ORR

Electrochemical reactions in PEMFCs are usually catalysed with expensive platinum-based catalyst as it has been established from the volcano plot and found that platinum has the highest ORR activity [20]. Therefore, the use of platinum in fuel cells must be significantly reduced or eliminated if the technology is to be widely available commercially. The alloying platinum with other metals has been explored as a means of reducing the amount of platinum used in ORR

catalysis [21]. The alloying of platinum with first row transition metals especially cobalt [22-25], nickel [26-28] and iron [29-31] have been reported by several research groups to reduce the overall amount of platinum present in catalysts as well as increase platinum's catalytic activity. Although platinum's alloys with several metals have been investigated for ORR, platinum-cobalt alloys are the commonly investigated type in literature due to their reported high ORR activity [32].

Although decreasing the amount of platinum has led to a reduction of catalyst cost, there has also been extensive research over the past several decades on developing non-platinum ORR catalysts [33-36]. These alternatives include other noble metals and their alloys [37-40], carbon-based materials [41-43], transition metal compounds such as macrocyclic compounds [44-46], chalcogenides [47, 48] and nitrides [49-51].

1.4 Palladium and its Alloys in ORR

Palladium is an important noble metal in use in many industries in the areas of dental appliances, electrical appliances, jewellery and chemical catalysis especially the automotive emission catalysts [52, 53]. Palladium catalysts have also been used in organic fuel oxidation [54]. These have received a lot of attention because palladium has similar properties to platinum; same face-centred cubic crystal structure and similar atomic size. palladium-catalysed ORR has been reported to proceed via a direct 4-electron pathway mechanism similar to platinum [55]. Although palladium has been reported to have a lower ORR than platinum [33], it's about 50 % cheaper than platinum. Therefore, the use of palladium-based catalysts has been investigated as alternatives to platinum for ORR.

Catalytic activity of palladium and its alloys in ORR has been reported as early as in 1960s by Chaston *et al*. [56] with preparation of Pd/C by reducing palladium salts on activated charcoal. An impregnation method followed by reduction with hydrogen at 300 °C was used by Moreira *et al*. [57] to prepare carbon-supported palladium on activated carbon and Vulcan. Both catalysts were tested for ORR in a PEMFC operating at room temperature and a three-fold increase of current density was observed when catalyst support was changed from activated charcoal to Vulcan.

More recently, palladium-cobalt alloy catalysts for ORR were prepared by Savadogo *et al*. [58] in 2004 by sputtering. CV tests indicated that an alloy of 72 % palladium and 28 % cobalt was stable under acidic conditions as there was no major change in particle shape or size during testing. Stability of the alloys was attributed to an electronic stabilisation effect of cobalt on

palladium. The authors reported a current density of 0.58 mA cm^{-2} at 0.80 V for the Pd-Co alloy; more than double the value of 0.25 mA cm^{-2} reported for bulk platinum [58].

Fernandez *et al.* [59] studied the ORR activity of palladium with a combination of cobalt, gold and titanium. The catalysts were prepared by an impregnation method followed by reduction with hydrogen at 350 °C. Pd-Co (with 20 % cobalt) on carbon showed the highest activity comparable to platinum but its performance reduced after the cell was polarised at 200 mV for 12 hours. Its stability was later found to improve with the addition of gold. Pd-Ti and Pd-Co-Au supported on carbon were also reported to have activity similar or close to platinum for ORR. The group reported current densities at 0.5 V of 0.15, 0.16 and 0.1 Acm^{-2} for commercial Pt/C, Pd-Co-Au/C and Pd-Ti/C respectively at a cathode metal loading of 0.2 mgcm^{-2}. Although the Pd-Co-Au/C catalyst had higher ORR activity, the Pd-Ti/C catalyst had a better stability.

Raghuveer *et al.* [60] performed a comparative study of Pd-Co-Au catalysts prepared by two different methods; a reverse micro-emulsion method followed by reductive heat treatment, and an impregnation method followed by NaBH$_4$ reduction. Catalyst prepared with NaBH$_4$ had to be treated at 900 °C before forming a single phase and had an average particle size of 46 nm while the catalyst prepared by reverse microemulsion formed a single phase after heat treatment at 500 °C and had an average particle size of 35 nm. Higher activity was found for catalysts prepared by the reverse microemulsion method (current density of 0.05 A cm^{-2} at 0.5 V) than those prepared with NaBH$_4$ (current density of 0.03 Acm^{-2} at 0.5 V). This was attributed to a higher degree of alloying in the microemulsion samples at lower temperatures which ensured the particle sizes stayed small and the surface area high. Open-circuit voltage (OCV) of the reverse microemulsion sample was reported as 0.89 V which was comparable to value obtained for a commercial 20 % Pt/C sample at 60 °C.

In a comparative study of commercial platinum catalyst and carbon supported Pd-Co alloy for ORR, Mustain *et al.* [61] prepared alloys of the type of Pd-Co on carbon by reducing precursor metal salts with sodium bicarbonate followed by heat treatment in a mixture of H$_2$ and Ar. Catalysts were evaluated in a single 5 cm^2 PEMFC between 30 and 60 °C. They found an alloy of Pd$_3$Co/C to have a performance comparable to ETEK commercial 20% Pt/C. They reported current densities of 0.5 Acm^{-2} at 0.5V for the Pd$_3$Co/C and Pt/C. Although long term stability data of catalysts were not provided.

Zhang *et al.* [62] also studied carbon supported Pd-Co (35% Co) for ORR; studying the effect of reducing agent (using ethylene glycol, sodium borohydride and formaldehyde) and H$_2$ treatment (from 300- 700 °C) temperature on catalyst morphology and activity. They found 300

°C was the best temperature for heat treatment for all three catalysts. They found that catalysts synthesised from all three reducing agents catalysed ORR via a four-electron reduction mechanism. They reported average Tafel slope as 70 mVdecade^{-1} and suggested that the rate determining step was a one electron transfer process. Ethylene glycol was found to produce the smallest catalyst particle size (about 5 nm) after heat treatment and the catalyst prepared in it also had the highest electrochemical surface area and activity. However, measurements of ECSA were qualitative and the authors suggested that a quantitative estimation may not be feasible as the catalysts were not made of a pure metal. Better performance of the EG-synthesised Pd-Co/C was attributed to smaller particle size and lower degree of aggregation. Its current density was reported as 1.87 mAcm^{-2} at 0.7 V which was lower than that of a Pt/C catalyst recorded as 2.09 mA cm^{-2} at 0.7 V. Also, its OCV was 80 mV lower than platinum.

Shao *et al.* [63] investigated oxygen-reduction reaction (ORR) of palladium monolayers on various surfaces and on palladium alloys. Their activities were correlated with their d-band centres calculated by density functional theory (DFT). They found a volcano-type dependence of activity on the energy of the d-band centre of palladium monolayers, with Pd-Pt (111) at the top of the curve. They reported activity of Pd$_2$Co/C to be comparable to that of commercial Pt/C catalyst. The kinetics of ORR on Pd$_2$Co/C predominantly involved a four-electron step reduction with the first electron transfer being the rate-determining step. The activity was attributed to the downshift of the d-band centre of the palladium skin on alloy surface due to the strong surface segregation of palladium at high temperatures.

Highly active nanoparticles of Vulcan supported Pd-Fe alloy for ORR were reported by Shao *et al.* in 2006 [64]. Half-cell tests were performed in acidic medium; the current density for Pd$_3$Fe/C (5.0 mAcm^{-2}) showed its ORR activity was slightly higher than that of the commercial Pt/C catalyst (4.5 mA cm^{-2}) under same test conditions. It was prepared by reducing FeCl$_3$ on commercial Pd/C at 500 °C in H$_2$ atmosphere. The activity of the palladium-iron alloys was found to be related to the Pd-Pd bond distance: the shorter this bond distance, the higher the activity of the prepared catalyst.

In a similar work, Tarasevich *et al.* [65] also synthesised various palladium-iron alloys by pyrolysis at high temperatures. Pd$_3$Fe/C of 7-8 nm produced at 750 °C was found to be the most active alloy. Catalysts were evaluated for ORR activity in acidic media, current density was reported as 2.35 mA cm^{-2} at 0.7 V. This high activity was attributed to the stabilisation of palladium nanoparticles, despite the high temperature of pyrolysis during the catalyst synthesis as high temperature processing is usually associated with increase in particle size due to

agglomeration. The authors also suggested that high activity was possible because the iron's presence in the alloy hindered the formation of palladium oxide. However, the authors did not report stability tests of this alloy; a further publication was to be made.

Two research groups studied the ORR activity of palladium-copper catalysts prepared by two different methods. Wang *et al.* [66] prepared their catalysts by a co-impregnation method followed by hydrogen reduction while Fouda-Onana *et al.* [67] prepared theirs by sputtering on glassy carbon. However, both catalysts prepared had activities about four times lower than the commercial Pt/C. Later on Xu *et al.* [68] presented a different finding. They prepared a highly ORR active novel Pd-Cu nanocomposite through a galvanic replacement reaction. Electron microscopy showed its structure as being nanotubular mesoporous structure with a nanoporous shell, comprised of interconnected alloy nanoparticles with size about 3 nm. The catalyst was tested in a half-cell with 0.1 M $HClO_4$ solution for ORR. They reported an exchange current density about one and half times that of Pt/C. The high activity was attributed to the unique trimodal hollow bimetallic structure. However, the authors did not report stability tests. These opposing findings regarding the activity of palladium-copper alloys highlight the importance of catalyst morphology as the nanoparticles had low ORR activity while the tubular structure had a higher activity.

Walsh *et al.* [69] used scanning electrochemical microscopy for rapid screening activity of bimetallic catalyst for ORR in acidic media. The combination of metals used was based on a thermodynamic selection guide they previously reported [70]. The guide assumes the first metal breaks the O=O bond of O_2 while the other reduces the adsorbed oxygen atoms. This combined a metal that easily breaks O=O bond (highly negative Gibbs free energy for metal oxide formation) with another whose oxide easily reduces to water (positive potential for metal oxide reduction). They measured activities for bimetallic combinations that showed a synergetic electrocatalyst effect, this included Au-V, Ag-V, Pd-Mn and Pd-V. A 60:40 Pd-V/C alloy was found to be the most active.

Further investigation into the effect of heat treatment on Pd-V/C's catalytic activity and stability was reported in 2010 [71]. Various ratios of Pd-V were synthesised by reduction of metal chloride salts with $NaBH_4$ on Vulcan. These catalysts were then heat treated at a range of temperatures in 10 % hydrogen in argon. XRD and TEM were used for characterising the effect of heat treatment on particle morphology. It was found that high temperatures increased average particle size. Current measured for the most active catalyst prepared, 60:40 Pd-V was 0.31 mA cm^{-2} at 0.7 V and much lower than that of a 20% Pt/C catalyst. A loss of ECSA upon cycling

was revealed by an accelerated stability test, the extent of this loss was found to be dependent on the composition of catalyst. Electrocatalyst testing after stability tests showed a loss of activity and microscopic analysis showed major changes in particle dimensions and dispersion on the carbon support.

From the literature (details of significant publications are shown below in Table 2), it seems that enhancement can be obtained in the ORR activity of palladium by alloying with the first-row transition metals especially iron, nickel and cobalt to achieve high activities that might be better than platinum's depending on the synthetic method and catalyst morphology. The method of synthesis has an effect on the activities of synthesised nanoparticles and ethylene glycol was suggested as the best reducing agent. Heat treatment can also improve catalytic activity and small alloy nanoparticles can be obtained at temperatures as high as 750 °C. The improvement in palladium's ORR activities have been mostly attributed to the presence of other metals and their ability to modify palladium's electronic properties. The palladium-based catalysts reported were found to be stable under test conditions, although the authors did not discuss the long-term stability of their prepared catalysts. The addition of titanium and gold were found to improve the stability of palladium catalysts.

Table 2: Significant publications on palladium-based catalysts for ORR for PEMFCs.

Catalyst	Current Density	Operating Conditions	Reference
Pd-Co-Au/C	0.16 Acm^{-2} (single cell)	0.5 V, 60 ℃, H_2/O_2 0.2 mg cm^{-2} cathode	[59]
Pd-Ti/C	0.10 Acm^{-2} (single cell)	0.5 V, 60 ℃, H_2/O_2 0.2 mg cm^{-2} cathode	[59]
Pt/C	0.15 Acm^{-2} (single cell)	0.5 V, 60 ℃, H_2/O_2 0.2 mg cm^{-2} cathode	[59]
Pd$_3$Co/C	0.15 Acm^{-2} (single cell)	0.5 V, 60 ℃, H_2/O_2 0.2 mg cm^{-2} cathode	[61]
Pt/C	0.15 Acm^{-2} (single cell)	0.5 V, 60 ℃, H_2/O_2 0.2 mg cm^{-2} cathode	[61]
Pd$_3$Fe/C	5.0 mAcm^{-2} (cathode)	0.8V, room temperature 10 μg cm^{-2} of metal	[64]
Pt/C	4.5 mAcm^{-2} (cathode)	0.8V, room temperature 10 μg cm^{-2} of metal	[64]
Pd-Co/C	0.58 mAcm^{-2} (half-cell)	0.8V, sputtered electrode	[58]
Pt/C	0.25 mAcm^{-2} (half-cell)	0.8V, bulk electrode	[58]
Pd-Co/C	1.87 mAcm^{-2} (half-cell)	0.7V, 14.6 μg cm^{-2} of metal	[62]
Pt/C	2.09 mAcm^{-2} (half-cell)	0.7V, 14.6 μg cm^{-2} of metal	[62]
Pd$_3$Fe/C	2.35 mAcm^{-2} (half-cell)	0.7V, 12μg cm^{-2} of metal	[65]

1.5 Pourbaix Diagram for Palladium

Pourbaix diagrams are a pictorial representation of stability of metals over a range of potentials and pH. They are particularly useful in electrochemistry for studying the corrosion and

dissolution of metals as well as understanding redox properties and evaluating the existing state of a specie [72]. They are commonly used to provide information on regions of metallic stability, passivation and instability of an aqueous electrochemical system over a range of potentials and pH. In comparison to base metals, noble metals such as platinum and palladium exhibit high resistance to oxidation due to their high thermodynamic stability. Noble metals are able to adsorb oxygen or form reversible oxides on their surface in oxidising aqueous environment or under anodic potentials [73].

Palladium's Pourbaix diagram reveals a region (ca. 0.9 to 1.2 V) where palladium is subject to corrosion at low pH values. Palladium is often corroded and displays low stability during oxygen reduction studies as it is exposed to low pH and high anodic potentials [74]. Therefore, palladium is more prone to electrodissolution and oxidation than other noble metals like platinum [75]. Platinum usually displays a higher stability and corrosion resistance because its corrosion region in the Pourbaix diagram occurs at higher potentials (ca. 1.2 to 1.4 V).
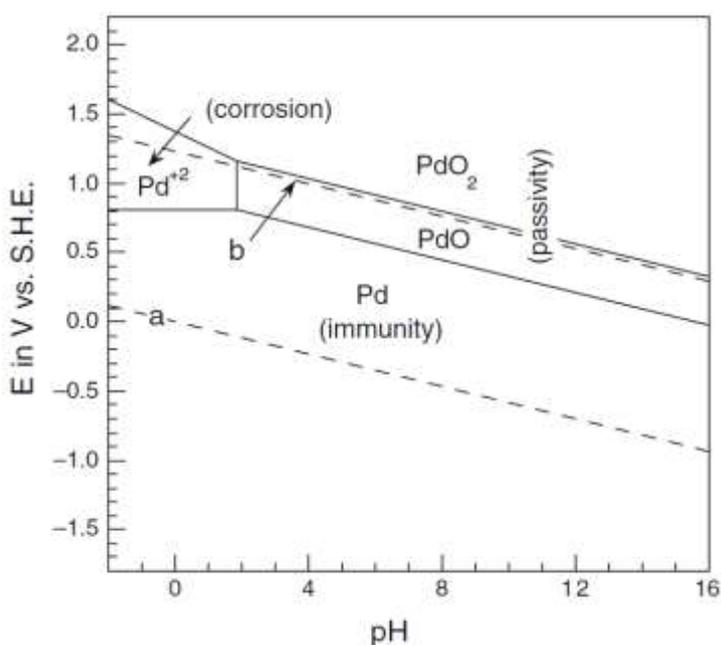
Figure 2: Pourbaix diagram for palladium at 25 °C [76].

In a typical PEMFC, the gradual loss of activity due to degradation of the platinum catalyst during operation is one of the main issues affecting PEMFCs [77]. Evidently, the use of a palladium catalyst would result in a more significant performance loss since palladium has a lower voltage cycling stability compared to platinum and would therefore be unsuitable for use as an ORR catalyst in PEMFCs.

The alloying of palladium with certain elements has been reported to be beneficial towards increasing palladium's ORR stability in acidic media [59, 63]. In this study, Pourbaix diagrams

were used to identify metals; gold [78] and iridium [79] that are acid-stable in the ORR potential regions. Gold and iridium were alloyed with palladium in an attempt to improve palladium's ORR stability and the resulting catalysts were studied for the oxygen reduction reaction.

The synthesised catalysts were supported on Vulcan; a carbon support subject to oxidation. Although Vulcan has been reported to be prone to corrosion under acidic fuel cell conditions at high potentials between 0.6 and 1.2 V [80], it has been suggested that the carbon support corrosion could be reduced by modifying the carbon surface with suitable metal oxides [81]. Therefore, Pourbaix diagrams were used to identify TiO_2 [82] and WO_3 [83]as acid-stable metal oxides; these were used to modify the Vulcan-support to form hybrid supports and the effect of these supports on the ORR of palladium-iridium catalysts was studied.

Also in this study, Palladium's Pourbaix diagram helped to identify that palladium was particularly more vulnerable to corrosion via palladium oxidation at potentials close to 0.96 V [73, 76], therefore the lower potentials from 0.87 to 0.4 V were used during stability tests so as to investigate another mechanism of catalyst degradation; particle size increase.

1.6 Catalyst Support for ORR

Carbon blacks (CB) are conventionally used as support materials because of their conductivity, high surface area, good chemical and electrochemical stability [84]. However, carbon blacks are made of carbon nanoparticles aggregated onto much larger particles. Diffusion of reactants and products can be impeded on the CB as they can only circulate between the carbon agglomerates or within carbon micropores causing major mass transfer limitations leading to low catalyst utilisation [85]. Also, carbon blacks undergo electrochemical oxidation into surface oxides and CO_2 at potentials near OCV (0.9-1.0 V) of a fuel cell with the oxidation rate increasing with potential [86]. Li *et al.* [87] reported that the presence of platinum nanoparticles on the carbon accelerated its corrosion rate. During this corrosion, catalyst particles became detached from the support. This led to particles aggregating to form larger particles hence reducing the catalysts surface area and performance. Also, carbon losses can reduce electronic continuity in the catalyst layer so the isolated catalyst particles can no longer participate in electrochemical reactions [88].

Therefore, the choice of catalyst support is crucial to performance in fuel cell operation as it determines the mass transfer and Ohmic resistance of the catalyst layer. The support can also influence catalyst's activity through an electronic or a geometric effect[89]. The support's electronic effect can modify the active sites on catalyst surface and hence its reactivity[90].

12

Also, the shape of the catalyst particles can be modified by the support [85]. Therefore, there has been research interest in the development of new catalyst supports.

To avoid the instability of carbon black supports, a range of materials have been investigated for use as support[91]. These can be broadly classified as carbon based and non-carbon-based supports. Nanostructured carbon-based materials have attracted research interest as support materials because of their good electrical and mechanical properties as well as pore textures, sizes and shapes. These materials include carbon nanotubes (CNTs) [92], nanofibres (CNFs) [88], carbon gels [93] and mesoporous carbon [94]. These materials are also relatively stable in acidic and alkaline media. Although, these nanostructured carbons do not prevent carbon corrosion, they have a lower oxidation rate due to their highly graphitic character[88]. Their porous structure can improve reactant and product diffusion while their crystalline structure can modify the supported metal's electronic properties to increase catalytic activity.

Non-carbon based supports have also been investigated so as to overcome the problem of carbon corrosion which is an issue for all carbon-based supports[95]. Materials such as metal oxides[96], tungsten carbide [97] and sulfated zirconia [98] have been investigated as alternatives to carbon based supports. Improvements have been reported in stability but their low conductivities limit their use in electrocatalysis.

1.7 Aim and Objectives of the Project

The primary aim of this project was to develop active and acid-stable palladium-based catalysts for oxygen reduction as suitable alternatives to platinum. The research objectives of the project were:

- to synthesise palladium-based catalysts by modifying palladium with acid-stable metals such as gold and iridium
- to characterise their physical and electrochemical properties
- to evaluate the effect of palladium-modification on ORR activity
- to study the stability of these catalysts when subjected to electrochemical degradation under potential cycling and potential holding conditions
- to evaluate the electrochemical effect of modifying the carbon-support with acid-stable metal oxides such as titanium and tungsten oxides
- to characterise the synthesised materials using spectroscopic as well as microscopic analytical methods.

These microscopic and spectroscopic analyses were to be used to determine surface species and the nature of the prepared catalysts to provide an insight into explaining their observed ORR

activities and stabilities. This work was aimed to be a systematic study of modifications to palladium's ORR stability by gold, iridium, titanium oxide and tungsten oxide.

Chapter 2. Experimental Methodology

This chapter introduces the general materials, as well as the characterisation techniques and analyses used in this work. The details of the experimental procedure for catalyst syntheses and voltammetry are described in the relevant results chapters.

2.1 Materials and Chemicals

$(NH_4)_2PdCl_4$ (Alfa Aesar, 97%), Ethylene glycol (Alfa Aesar, 99%), NaOH (Sigma Aldrich, 98%), IrCl3.3H2O (Alfa Aesar, 97%), $HAuCl_4.3H_2O$ (Sigma Aldrich, 98%), $NaH_2C_6H_5O_7$ (Sigma Aldrich, 99%), $Na_3C_6H_5O_7$ (Sigma Aldrich, 98%), $H_3[P(W_3O_{10})_4].H_2O$ (Sigma Aldrich, reagent grade), $Ti(OCH_2CH_2CH_2CH_3)_4$ (Sigma Aldrich, 97 %) H_2O_2 (Sigma Aldrich, 30 %) Vulcan XC72R (Cabot), Water (Milli-Q system filtered). All reagents were used as received. The quantities of the precursors used in preparing the catalysts are shown below in Tables 3, 4 and 5.

Table 3: Quantities of reagents used for preparing palladium-gold catalysts.

Catalyst	PdAu/C	Pd$_3$Au/C	Pd/C
$(NH_4)_2PdCl_4$	69.57 mg	104.45 mg	136.29 mg
$HAuCl_4.3H_2O$	2250.5 µL	1275.5µL	-
$Na_3C_6H_5O_7$	470.6 mg	617.8 mg	679.8 mg

Table 4: Quantities of reagents used for preparing palladium-iridium catalysts.

Catalyst	PdIr/C	PdIrAu/C	PdIr/TiO$_2$-C	PdIr/WO$_3$-C
$(NH_4)_2PdCl_4$	69.57 mg	62.62mg	69.57 mg	69.57 mg
$IrCl_3.3H_2O$	47.28 mg	42.55 mg	47.28 mg	47.28 mg
$NaH_2C_6H_5O_7$	315.82 mg	310.22 mg	315.82 mg	315.82 mg
$HAuCl_4.3H_2O$		516 µL		

Table 5: Quantities of reagents used for preparing tungsten oxide-carbon and titanium oxide-carbon composites.

Support	WO$_3$-C	TiO$_2$-C
Phosphotungstic acid	224.46 mg	-
Ti-tbutoxide	-	439.53 mg
Vulcan	750 mg	750 mg

2.2 Physical Characterisation Techniques

2.2.1 X-ray Diffraction (XRD)

X-ray diffraction is an analytical technique for the determination of a material's crystal lattice; providing phase identification as well as unit cell dimensions for a bulk material[99]. X-rays produce a diffraction pattern when they hit a regular array of atoms as the x-ray's wavelength is in a similar order of magnitude as the spacing between the atom's crystal planes. This diffraction pattern observed is based on Bragg's law[100].

$$n\lambda = 2d \sin \theta \tag{2.1}$$

where λ is the wavelength of the monochromatic x-rays, d is the distance between n layers of atoms in a crystal and θ is the Bragg angle. The Bragg angles are measured for a series crystal lattice planes[101]. A detector counts the x-rays diffracted from a sample over a range of Bragg angles. A material is then identified based on the intensities of x-rays diffracted at particular Bragg angles[100].

In this study, XRD was used to determine the formation of an alloy. This was done by comparing the Bragg angles of the bimetallic and ternary catalysts with those obtained from pure palladium and data from the international centre for diffraction data (ICDD) database. A shift in Bragg angles indicated alloy formation while two individual set of Bragg angles obtained for a bimetallic catalyst meant no alloy formation[102].

Crystallite sizes were estimated from the full width at half maxima of Pd (220) peaks around 68°. This peak was selected it was considered not to be influenced by the carbon support[103]. A broad carbon peak at 25° was seen for all catalysts[62]. Crystallite sizes were estimated using the Scherrer equation[104].

$$D = k\lambda/FWHM \cos\theta \qquad\qquad\qquad\qquad\qquad\qquad (2.2)$$

where D is crystallite size in Å, k is a constant 0.89 for spherical particles, λ is 1.5418 Å, FWHM is full width at half maximum measured for the (220) peak at Bragg angle θ.

XRD patterns were obtained for the catalysts by irradiating the samples with Cu-Kα x-ray with a characteristic wavelength of 1.5418 Å at Newcastle University using a PANalytical X'Pert Pro MPD with a fitted X'celerator. Diffraction data were collected from 0 to 100° Bragg angles. Phase identification and the full-width at half maxima measurements were carried out using PANalytical high score plus software alongside the ICDD database and X'pert data viewer for all samples.

2.2.2 Transmission Electron Microscopy (TEM)

Transmission electron microscopy is an analytical technique used to observe nanometric material. It works like a microscope but uses high electron beam with much smaller wavelengths to provide a significantly higher resolution than light microscopes. An image is obtained when the electrons pass through the sample. Since metal particles and carbon particles absorb electrons differently, they present a contrasting image with the metals appearing much darker than the carbon[105].

High resolution transmission electron microscopy can be used to measure even smaller ranges, such as the interplanar lattice spacing, *d* on individual particles. This information can be used to identify the particular particles as *d*-spacing is characteristic for a material[106].

In this study, TEM images were used to estimate the particle sizes of synthesised particles, it also provided information on catalyst morphology and agglomeration of particles. This information is useful since electrochemical surface area and catalyst activity is usually linked to particle sizes[107]. The particle size distribution for the catalysts were obtained by measuring the diameter of over 100 random particles supported on carbon and an average was reported. The diameters were measured using the Image-J software.

The TEM as well as EDX analyses were done at Leeds University electron microscopy and spectroscopy centre. The instrument used was FEI Tecnai TF20 FEGTEM field emission gun TEM/STEM fitted with HAADF detector, Oxford Instruments INCA 350 EDX system/80 mm X-Max SDD detector and Gatan Orius SC600A CCD camera.

2.2.3 Energy Dispersive X-ray Spectroscopy (EDX)

Energy dispersive x-ray spectroscopy is an analytical technique that can determine the elemental composition of a sample when irradiated with an electron beam. This excitation causes characteristic x-ray emissions in the sample. A detector measures and quantifies the emitted x-rays; leading to elemental composition information[108].

In this study, EDX was used to determine the elemental compositions of the prepared catalysts; giving metal to carbon ratios. EDX analysis were done alongside TEM analysis at Leeds University as the TEM machine had the x-ray detector fitted.

2.2.4 X-ray Photoelectron Spectroscopy (XPS)

X-ray photoelectron spectroscopy (XPS) is an analytical technique used in studying the surface composition of materials. When the x-rays interact with the atoms on the surface of material being studied, electrons are emitted from the top layers (1- 10 nm). These electrons are ejected with characteristic kinetic energies that is related to the energy level where the electron was ejected from as well as the energy of the incident photon[109]. The recorded spectrum is made up from the number of ejected electrons over a range of energies. These energies and their intensities is then used for identification and quantification of the surface elements. Chemical shifts are observed in the spectra of an element as a result of different bonding environments, providing information on the oxidation states [110].

In this study, XPS was used to study the electronic structures and compositions of the catalysts as-prepared and after catalysts have been subjected to degradation tests. It was hoped that trends in catalyst activities and stabilities can be explained by the surface analysis. XPS analysis was done using a Kratos Axis Nova spectrometer at Newcastle University. The as-prepared catalysts were mounted on a copper double-sided adhesive tape. The catalysts collected from the electrode tip after degradation were drop-casted onto aluminium foil. The spectra were recorded at room temperature and irradiated with monochromatic Al Kα source with energy of 1486.6 eV run at 15 kV and 10 mA. Pass energies of 20 eV and 160 eV were used for recording individual element regions and survey spectra respectively.

Peak fitting of XPS spectra peaks were done using CasaXPS software. The curves were fitted after a Shirley background subtraction using a mixture of Gaussian and Lorentzian line shapes. The metallic and non-metallic peaks were fitted with asymmetric and symmetric Gaussian-Lorentzian line shapes respectively[111]. All XPS spectra were energy scale calibrated with respect to the C 1s peak at 284.4 eV[112].

2.3 Electrochemical Characterisation and Techniques

2.3.1 Electrochemical Evaluation

The catalyst ink was prepared by mixing 5 mg of carbon supported catalyst with 162 µL of water, 800 µL of ethanol and 38 µL Nafion®. The mixture was placed in the ultrasonic bath for 30 minutes. A 5 µL drop of catalyst ink was deposited onto the glassy carbon tip and then dried for 15 minutes. The catalyst loading on the electrode was 0.2 mg cm^{-2} for all catalyst tested. The voltammetry data were recorded using an AutoLab PGSTAT30 potentiostat and analysed with GPES software. All experiments were carried out at room temperature.

Half-cell evaluations were carried out using a three-electrode cell consisting of a glassy carbon rotating ring-disk electrode with a 4 mm diameter tip and area 0.1256 cm^{-2} area and a platinum ring with area of 01884 cm^2. The potential applied to the platinum ring was 1.2 V (vs NHE). The counter electrode was 7.5 cm long platinum wire with 0.5 cm diameter. The reference electrode was an Ag/AgCl electrode (209 mV Vs NHE). The potentials referred to in this study are referenced to the normal hydrogen electrode (NHE).

For all electrochemical experiments, the electrolyte, 75 mL of 0.5 M H$_2$SO4 was saturated either with nitrogen or oxygen before experiments. The gas was bubbled into the solution at a flow rate of about 30 cm^{3}min^{-1} for 30 minutes before each experiment. During the chronoamperometry and potential cycling experiments, a lower flow rate of about 15 cm^{3}min^{-1} was used to ensure that gas saturation was maintained throughout the experiment. The details of the experimental potential ranges and scan rates are described in the relevant chapters for each voltammetric experiment.

2.3.2 Linear Sweep and Cyclic Voltammetry

An electrochemical reaction usually involves: transport of reactants to the electrode surface, adsorption of the reactants onto the electrode, charge transfer and transport of the products from the electrode. Cyclic voltammetry is the most commonly used technique for studying electrochemical reactions. It measures an electrode's current response to applied potential. During the experiment, the potential is scanned from a potential value to a switching potential and back in the opposite direction to the starting potential. The cyclic voltammogram trace is obtained by plotting a graph of current against the applied voltage. It can be used to study catalyst behaviour in different potential regions. This can provide useful information on kinetics and mechanisms of electrochemical reactions. The electrochemical behaviour of an electrode can be investigated by linear sweep voltammetry (LSV).

During the LSV experiment, a selected potential range is scanned linearly over time to obtain a current-potential curve. The scan usually begins at a potential where no electrochemical reactions are occurring and hence no current is observed. After the start of the scanning to higher or lower potentials, an anodic or cathodic current is observed when the potential is high or low enough to cause the oxidation or reduction of an active electrochemical species. This current increases as the reaction kinetics becomes faster until it reaches a peak value and then starts to decrease. The highest current value is reached when the potential reaches a value at which all the reduced or oxidized form of the active electrochemical material is used up. When the potential reaches the set limit, it changes direction and scans towards the second set limit. During this second potential scan, the oxidized or reduced species react again to give another cathodic or anodic current peak. The full current-potential curve is called is the cyclic voltammogram.

The cyclic voltammogram of an electrode without any active species in the electrolyte is characteristic of that electrode. Therefore, the modification of the electrode material, for instance by alloying it with another metal, would lead to a change in the current-potential curve recorded. This makes cyclic voltammetry a very useful tool in electrochemical analysis[5].

Cyclic voltammetry measures changes in current and these current changes can be related to ongoing electrochemical processes such as a reduction or an oxidation. This principle can be used to calculate the total charge needed for a reduction or an oxidation. The total charge along with number of electrons transferred in the process can be used to calculate an electrochemical surface area. Since these electrochemical reactions take place on the surface at an atomic level, the electrochemically active surface area is much larger than the geometric area. For potential catalysts, the electrochemical surface area is often used for their characterisation since other parameters such as current and reaction rates are measured relative to it. In this study, the electrochemical surface area is used to assess catalyst's durability as a more stable catalyst is expected to retain a higher percentage of its initial surface area when subjected to degradation. As shown in Figure 3 below, the CV of a palladium catalyst comprises of three potential regions. In the positive sweep, hydrogen desorption on palladium starts at potentials more positive than 0 V (0.05 to 0.3 V). This is followed by the double layer charging region observed between 0.32 and 0.7 V. Then the oxide region starts with surface oxidation of palladium at about 0.75 V to 1.2 V. In the reverse scan, a reduction of these surface oxides starts from 1.2 V to lower potentials and the peak of Pd-O reduction is seen at 0.7 V, followed by a double layer region from 0.55 to 0.35 V and hydrogen adsorption takes place from 0.3 to 0.05 V.
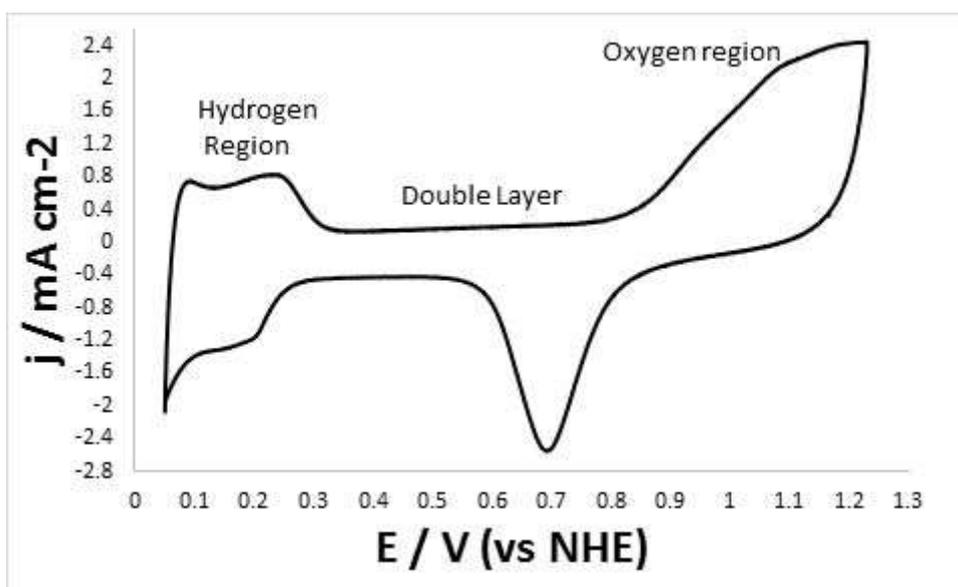
Figure 3: Cyclic voltammogram for a sample of prepared palladium on carbon catalyst, recorded in N_2-saturated 0.5 M H_2SO_4 at a scan rate of 100 mVs^{-1}.

From literature, it is known that 210 μC of charge in the hydrogen adsorption or desorption area corresponds to 1 cm^{-2} electrochemical surface area (ECSA) for palladium and platinum electrodes [113]. Therefore, the measurement of hydrogen adsorption or desorption charge can be used to calculate a catalyst's ECSA. Although, it is more common to calculate the ECSA from the charge in Pd-O reduction peak as this often a better-defined area. 420 μC of charge in the Pd-O reduction peak corresponds to 1cm^{-2} of ECSA for platinum and palladium electrodes.

2.3.3 Three-electrode Cell

This is made up of the working, counter and reference electrodes. The working electrode is usually made from glassy carbon, gold or platinum. The counter electrode is typically a platinum sheet or coil. For ORR studies, the cathodic reaction is being investigated. The catalyst being studied is deposited on the working electrode. The working electrode together with the counter electrode forms a circuit as the counter electrode balances the charges added or removed by the working electrode. A schematic diagram of the 3-electrode cell set up used in this study is shown in Figure 4.

Oxidation of water to oxygen and protons occurs at the counter electrode while oxygen reduction occurs at the working electrode. As only the ORR is of interest in this study, the area of the counter electrode is much larger than that of the working electrode so that the anodic reaction does not become the limiting reaction. A reference electrode is used to minimise the electrolyte's resistance on the working electrode's potential and it measures potential at the working electrode. This reference electrode is usually placed in a Luggin capillary so that the

tip can be placed very close to the working electrode as shown below. This short distance minimises the electrolyte resistance without blocking access to the working electrode's surface by the reactants [5]. Ag/AgCl (0.209 V vs NHE) was the reference electrode employed in this study.

In this study, the working electrode employed was a rotating ring-disk electrode. The rotating ring-disk electrode used was a rotating glassy carbon disk with an additional platinum ring around this disk. While the rotating disk's rotation resulted in a controllable flux of electrolyte (containing dissolved oxygen) over the catalyst deposited on the electrode, the platinum ring held at 1.2 V (vs NHE) measured the current associated with the production of peroxide intermediates. For each catalyst, a series of LSV experiments involving changing electrode rotation rates (400, 625, 900, 1225 and 1600 rpm) were recorded. The results were extrapolated to infinite rotation speed so as to eliminate mass transport effects and evaluate reaction kinetics in the catalysts. The information from the disk and ring electrodes was used to study if oxygen reduction on the catalysts proceeded via the 2 or 4 electron pathway.
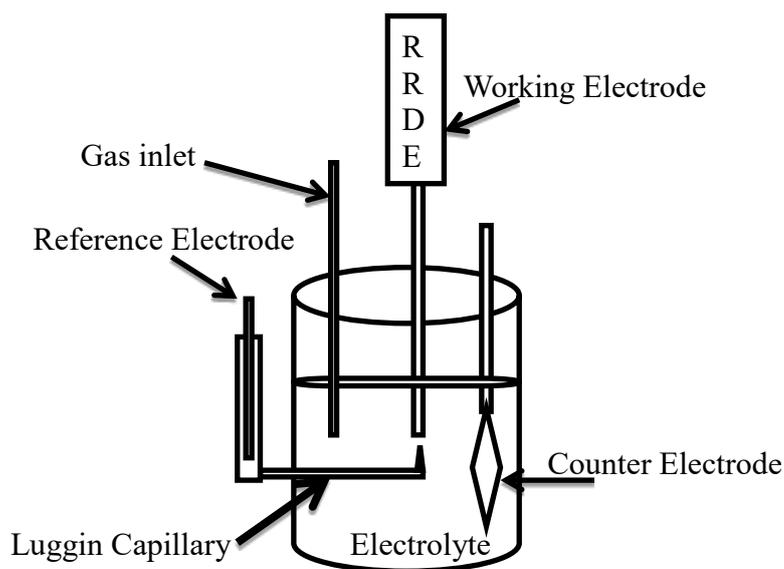
Figure 4: Schematic diagram of a 3-electrode cell.

2.3.4 Tafel Analysis

The Butler-Volmer equation describes an exponential relationship between the current density, overpotential and exchange current density in the absence of mass transport effect and at high overpotentials. This equation is shown below.

$$i = i_0 \left[\exp\left[\frac{-\alpha F \eta}{RT}\right] - \exp\left[\frac{\alpha F \eta}{RT}\right] \right] \tag{2.3}$$

Where i is the overall current density, i_0 is the exchange current density, η is the overpotential, α is the transfer coefficient, F is the Faraday constant, R is the gas constant and T is temperature.

Rearranging the equation gives the overpotential as shown below

$$\eta = \left[\frac{RT}{\alpha F}\right] \ln i_0 - \left[\frac{RT}{\alpha F}\right] \ln i \tag{2.4}$$

This can be rewritten as:

$$\eta = \left[\frac{2.3RT}{\alpha F}\right] \log i_0 - \left[\frac{2.3RT}{\alpha F}\right] \log i \tag{2.5}$$

Assuming $a = \left[\frac{2.3RT}{\alpha F}\right] \log i_0$ and b= $\left[\frac{-2.3RT}{\alpha F}\right]$ (2.6)

then equation (2.6) can be simplified as

$$\eta = a + b \log i \tag{2.7}$$

Equation (2.7) is the Tafel equation.

From experimental data of currents at various overpotentials, a plot of log i against η (Tafel plot) can be obtained. The Tafel plot can be used to calculate the Tafel slope, b. The transfer coefficient, α, which relates to the reaction mechanism can be calculated using equation (2.6). Also, extrapolation of the graph to zero overpotential yields the log of i_0. i_0, the exchange current density is measured relative to the electrochemical surface area and relates to the rate at which an electrochemical reaction occurs for a given electrode. In this study, calculation of exchange current density was used as a measure of a catalyst's ORR activity.

2.3.5 Koutecky-Levich Analysis

The Koutecky-Levich equation describes the relationship between the overall current density and the rotation speed of the working electrode.

$$\frac{1}{i} = \frac{1}{i_k} + \frac{1}{B\sqrt{\omega}} \tag{2.8}$$

Where i is the overall current density, i_k is the kinetic current density, ω is the rotation speed and B is a constant dependent on the oxygen diffusivity, concentration and on the viscosity of the electrolyte. Koutecky-Levich plots can be obtained from experimental data by plotting i^{-1} against $\omega^{-1/2}$, where i is the overall current density and ω is the rotation speed, at a given potential value. The extrapolation of the linear region of the plots to infinite rotation speed allows for the determination of the kinetic current, i_k.

Another form of the Koutecky-Levich equation describes the relationship between the overall current density and the currents with and without mass transport effects.

$$\frac{1}{i} = \frac{1}{i_k} + \frac{1}{i_l}$$

(2.9)

Where i is the overall current density, i_k is the kinetic current density and i_l is the limiting current density. i_l can be expressed as shown below

$$i_l = 0.62nFCD^{\frac{2}{3}}V^{\frac{-1}{6}}\omega^{\frac{1}{2}}$$

(2.10)

Where i_l is the limiting current density, n is the number of electrons transferred, F is the Faraday constant 96845 Cmol^{-1}, C is the concentration of dissolved oxygen (1.03x10^{-3}M), D is the diffusion coefficient of oxygen (2.1x10^{-5}cm^{2}s^{-1}), V is the kinematic viscosity of the electrolyte solution (1.1x10^{-2} cm^{2}s^{-1}) and ω is the rotation speed in rads^{-1}. The values of n can be obtained for the catalysts from experimental data by plotting i_l vs $\omega^{1/2}$. The number of electron transferred can be used for determining the reaction pathway[114].

Chapter 3. Palladium-Gold Bimetallic Particles as Oxygen Reduction Catalysts

3.1 Introduction

Platinum-based catalysts are usually considered the most suitable for ORR in acidic media due to platinum's high ORR activity, good stability and its ability to perform the direct 4-electron reduction of oxygen to water [115]. Gold is a cheaper noble metal with a similar mass and crystal structure to platinum. In contrast to platinum, gold has a lower ORR activity and undergoes oxygen reduction mainly via the 2-electron reduction mechanism [116, 117] in acidic media. In a comparative study, 795 mV was reported as the reduction peak potential for Pt/C and only 265 mV for Au/C [118]. Shao *et al.* used density functional theory to calculate ORR activities of palladium monolayer on various elements and palladium on gold was found to be active, although with lower activity than palladium on platinum [119]. The authors correlated this activity to a modification of palladium d-band centres by these elements.

Gold has also been reported to be able to modify and enhance the ORR properties of platinum and palladium. For instance, Zhang *et al.* [120] reported that the modification of a platinum catalyst with gold resulted in the stabilisation of the catalyst. Pt/C and gold-modified Pt/C were subjected to 30,000 cycles of potential cycling between 0.6 and 1.1 V, with the LSVs recorded both catalysts before and after the degradation test. The gold-modified Pt/C and the unmodified Pt/C showed half-wave potential degradation of 5 and 39 mV respectively. The authors suggested that gold was able to increase platinum's oxidation potential and hence improve its stability. Palladium-gold nanowires on carbon were reported to exhibit enhanced activity of 0.40 mAcm^{-2} when compared to palladium nanowires on carbon (0.12 mAcm^{-2}) and commercial platinum nanoparticles on carbon (0.20 mAcm^{-2}) respectively[121]. The authors suggested that the addition of gold was able to stabilise palladium against dissolution and oxidation by suppressing the formation of Pd-O at potentials of up to 0.9 V. Although an enhancement of activity was observed, stability data for the catalysts were not presented.

The addition of gold to a palladium-cobalt catalyst was found to improve its activity compared to Pd/C [59] in acidic media. The improvement in activity was attributed to an electronic modification of the palladium with gold and cobalt. Rao *et al.* [122] also reported an enhancement in ORR for a PdCoAu/C catalyst compared to Pd/C. At 0.8 V, current densities of 1.32 mAcm^{-2} and 0.15 mAcm^{-2} were recorded for PdCoAu/C (heat-treated at 800 °C) and as-prepared Pd/C respectively. Shim *et al.* prepared a series of catalysts featuring a palladium shell on a core of Au/C and found a catalyst PdAu/C with Au:Pd ratio of 1:0.61 to have the highest

ORR activity in acid, comparable to that of Pt/C [123]. Half-wave potentials were reported to be 0.771 V and 0.731 vs NHE for the PdAu/C and Pt/C catalysts respectively. This catalyst was found to be stable as it was able to maintain its original activity in terms of onset potential, half-wave potential and limiting current when subjected to 50 consecutive RDE voltammograms recorded in an oxygen-saturated 0.5M sulphuric acid.

Although catalysts based on pure gold have low ORR activity in acidic media, the literature suggests that the alloying of gold to palladium can result in enhancement of palladium's ORR activity and stability. Even though gold has a lower ORR activity in acid, it has a high electrochemical stability[73]. From its Pourbaix diagram, it can be observed that gold is resistant to oxidation over a large range of pH values as well as higher potentials. Gold was selected for use in this study because of this stability at low pH values and high potentials.

3.2 Synthesis of Palladium-Gold Bimetallic Catalysts

Electrocatalysts were prepared a simultaneous co-reduction of the palladium precursor, $(NH_4)_2PdCl_4$ and the gold precursor $HAuCl_4.3H_2O$ in ethylene glycol. In a typical synthesis, appropriate quantities of the precursor salts (shown in Chapter 2) were added to a 10 mL solution of trisodium citrate in deionised water to obtain palladium to gold compositions of 1:1 and 3:1(weight ratio of palladium to gold). 1M solution of NaOH was added dropwise so as increase the pH to 11. This mixture was added dropwise to a flask containing a nitrogen-saturated sonicated suspension of 200 mg Vulcan in 75 mL ethylene glycol. The reaction was heated to 120 °C and refluxed at this temperature for 3 hours while being constantly stirred. After cooling down, the carbon-supported catalyst was separated from the reaction by centrifuging. Catalyst was extensively washed with deionised water and ethanol. It was dried at 80 °C in the oven overnight. The resulting solid was ground with a mortar. A catalyst containing palladium only on carbon (Pd/C) was also synthesised by the same method using only the palladium precursor.

3.3 X-ray Diffraction (XRD) Analysis of Palladium-Gold Bimetallic Catalysts

The X-ray diffraction patterns of the palladium-gold (PdAu/C and Pd_3Au/C) and the palladium (Pd/C) catalysts are shown in Figure 5. The broad peak at 25° was assigned to carbon from the support for all catalysts[113]. For all three catalysts, the diffraction peaks at 2θ values of ca. 40.1°, 46.5°, 67.9°, 81.9° and 86.4° were attributed to the (111), (200), (220), and (311) crystal planes of palladium respectively [124]. Additional peaks were seen at 38.1°, 44.3°, 64.4°, 77.3° and 81.5° for the 2 gold-containing samples PdAu/C and Pd_3Au/C. These were assigned to the (111), (200), (220), and (311) crystal planes of gold respectively [124]. These diffraction

patterns reveal individual palladium and gold phases; no alloy phases were observed. This is in good agreement with the work of Chen *et al.* where alloy formation between palladium and gold was only observed after a heat-treatment at 200 °C was applied to the synthesised palladium-gold catalyst [124]. The average crystallite sizes for palladium and gold particles were estimated from the full-width at half maximum of the palladium (220) and gold (220) peaks using the Scherrer equation [100]. The 220 peaks were used for crystallite size calculations because they are considered to not be influenced by diffraction peaks corresponding to the carbon support [124]. The calculated sizes were 7.2 nm (palladium) and 8.7 nm (gold), 4.9 nm (palladium) and 9.2 nm (gold) for the PdAu/C and Pd₃Au/C catalysts respectively. The crystallite size for the pure palladium catalyst Pd/C was also found to be 4.3 nm.
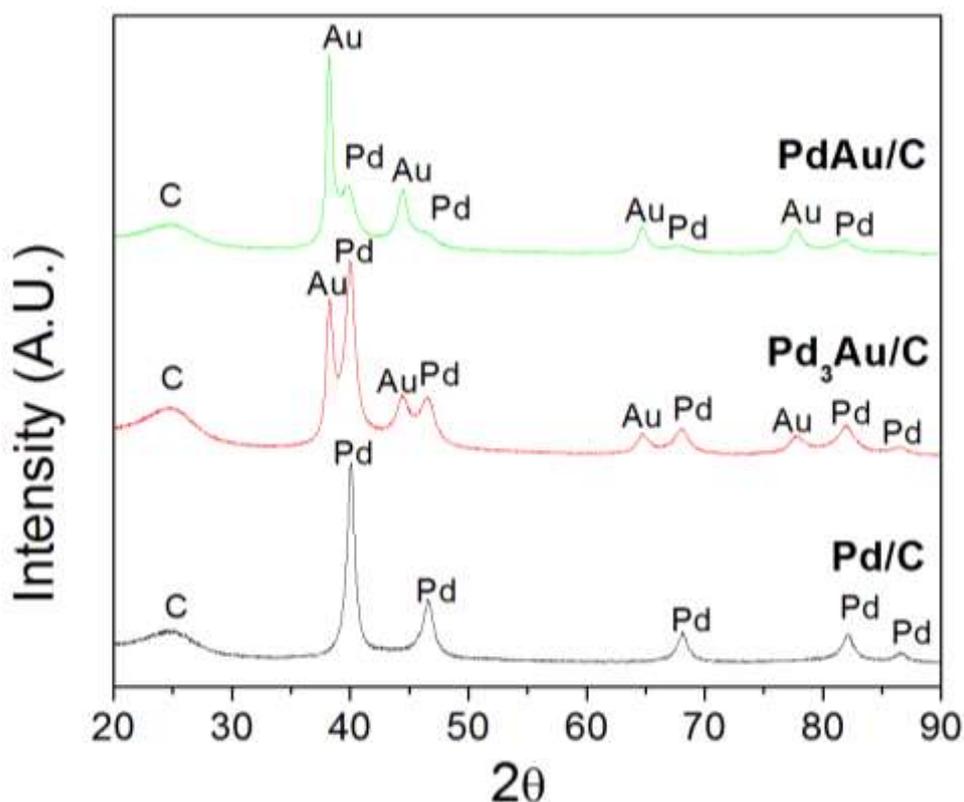
Figure 5: X-ray diffraction patterns obtained for the Pd/C, Pd₃Au/C and PdAu/C catalysts. Reflections labelled 'c, 'Pd' and 'Au' correspond to carbon, palladium and gold respectively.

3.4 TEM and EDX Characterisation of Palladium-Gold Catalysts

Transmission electron microscopy was used to obtained images for the three catalysts; the images showed that spherical metal particles were dispersed on the carbon support without much agglomeration for the three catalysts. The particle size distribution was obtained for each catalyst by measuring the sizes of over 100 randomly selected particles. The TEM images as well as the particle size distributions obtained for the three catalysts are shown in Figures 6, 7 and 8. The average particle sizes were 7.5 nm, 6.8 nm and 5.4 nm for PdAu/C, Pd₃Au/C and

Pd/C catalysts respectively. The measured average particle sizes were in good agreement with those calculated from the XRD peaks using the Scherrer equation.
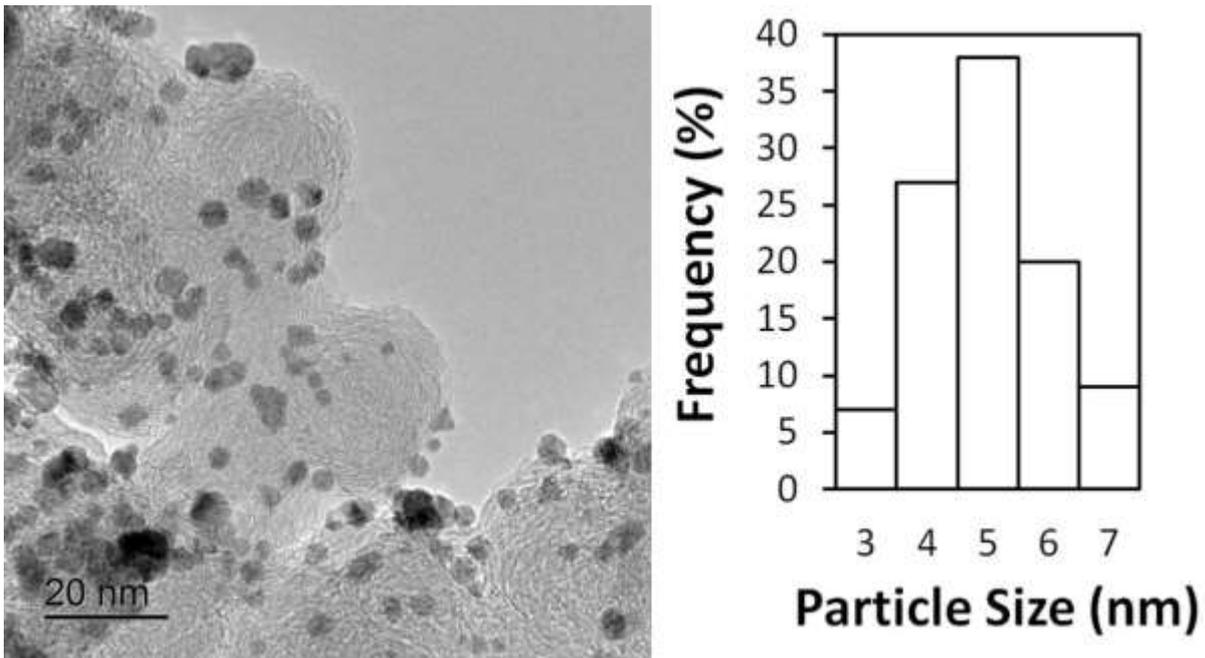
Figure 6: TEM image obtained for Pd/C and its corresponding particle size distribution showing particles of about 5 nm.
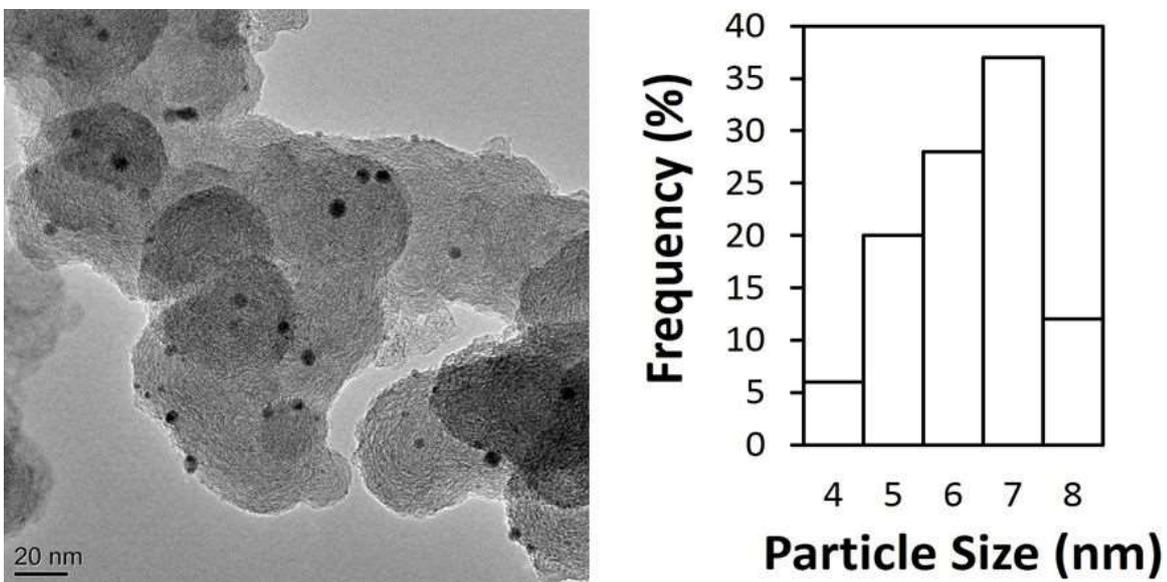
Figure 7: TEM image obtained for Pd₃Au/C and its corresponding particle size distribution showing well-dispersed particles.
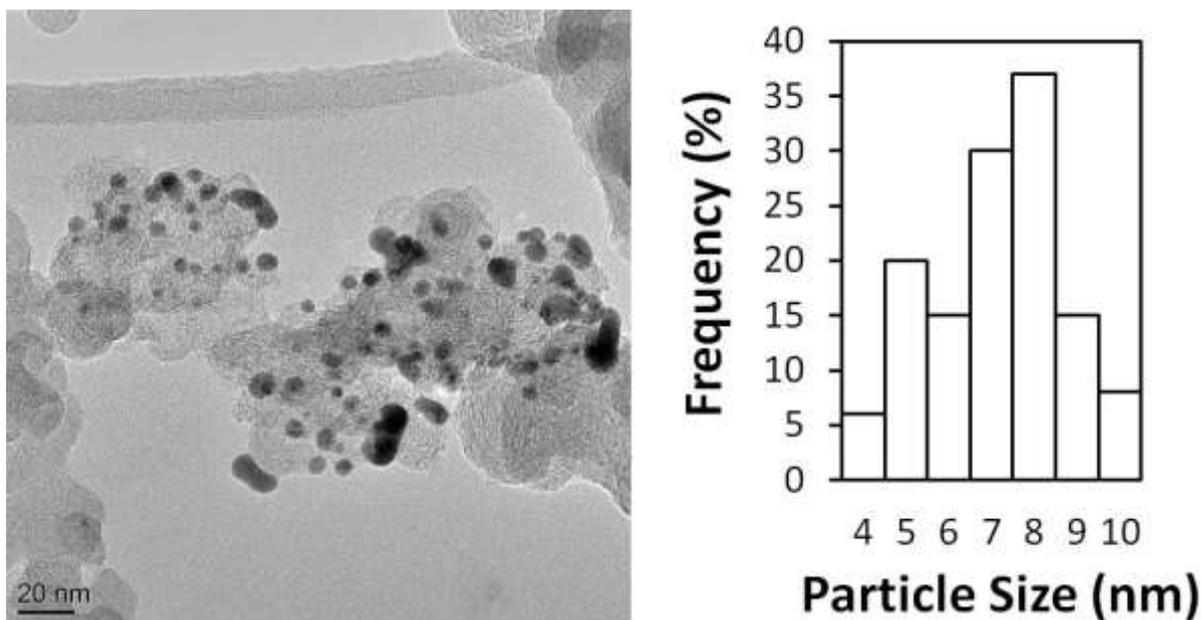
Figure 8: TEM image obtained for PdAu/C and its corresponding particle size distribution showing a mixture of smaller and larger particles.

High resolution images of nanoparticles on Pd$_3$Au/C and Pd/C catalysts were also obtained. Fast Fourier transform was used to measure the lattice space. In the pure palladium catalyst, the interplanar spacing between the lattice planes was measured to be 0.22 nm. This was found to correspond to the (111) plane of face-centred cubic palladium [124]. The same interplanar spacing of 0.22 nm was observed in the Pd$_3$Au/C catalyst as well as an additional spacing of about 0.24 nm corresponding to gold (111) plane [125] showing the presence of palladium and gold in the Pd$_3$Au/C.
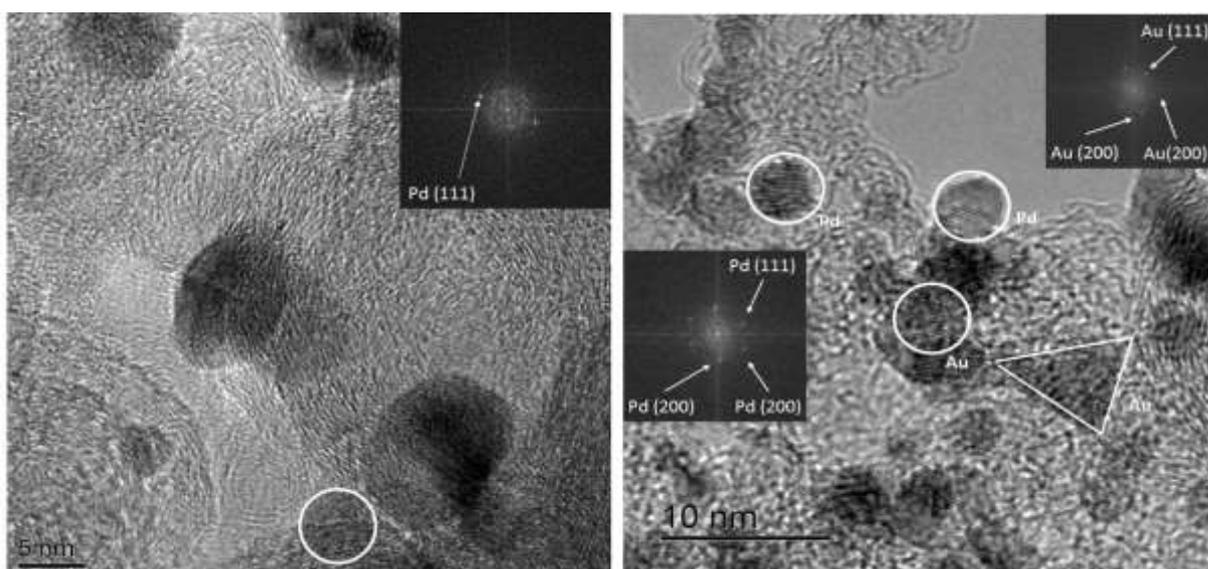
Figure 9: High resolution image obtained for Pd/C and Pd$_3$Au/C showing lattice planes for palladium and gold.

29

According to the preparation procedure, complete deposition of palladium and gold precursors on the support would yield 20 % weight metal catalysts. The average weight percentages of metal were obtained from EDX measurements at 5 different spots on each sample so as to get a good average value. The average values for palladium and gold in Pd/C, Pd₃Au/C and PdAu/C are presented in Table 6. The values obtained were close to the expected values; indicating a complete precursor reduction and deposition of metal particles on the support.

Table 6: EDX metal weight average, average particle sizes estimated from XRD and TEM analysis for PdAu/C, Pd₃Au/C and Pd/C catalysts.

Catalyst	XRD Estimated Crystallite Size (nm)		TEM Average Particle Size (nm)	EDX Metal Average	
	Pd (nm)	Au (nm)		Pd (% wt.)	Au (% wt.)
PdAu/C	7.2	8.7	7.5	10.8	11.5
Pd₃Au/C	4.9	9.2	6.8	16.2	5.8
Pd/C	4.3	-	5.4	21.4	-

It was observed from Table 6 that the estimated crystallite sizes from XRD were slightly higher than the average particle sizes measured from TEM. This may be as a result of some smaller nanoparticles not being so visible in the TEM images and therefore were not included in the average particle size calculation while they are detected in XRD peaks used for estimating the crystallite sizes. An increase in particle size with increasing amount of gold in the catalysts was also observed. This could be due to an initial fast reduction of gold, followed by a slower reduction of palladium on the gold since gold has a higher redox potential than palladium [126].

3.5 Cyclic Voltammetry (CV) Characterisation of the Palladium-Gold Catalysts

PdAu/C, Pd₃Au/C and Pd/C were subjected to cyclic voltammetry so as to study their electrochemical behaviour and redox processes. A cyclic voltammogram of the prepared 20 % palladium on carbon (Pd/C) recorded between 0.05 V and 1.2V at a scan rate of 100 mVs⁻¹ is shown in Figure 10. In the positive sweep, hydrogen desorption was observed from 0.05 to 0.3 V, followed by the double layer region between 0.32 and 0.7 V and surface oxide formation was observed between 0.75 and 1.2 V. In the reverse scan, reduction of surface oxide was observed from 1.2 V to about 0.6 V, with Pd-O reduction observed from 0.82 V (reduction peak

centred around 0.7 V), followed by a double layer region from 0.55 to 0.35 V and hydrogen adsorption region between 0.3 to 0.05 V. These observations are consistent with those reported for Pd/C in literature [113, 127].
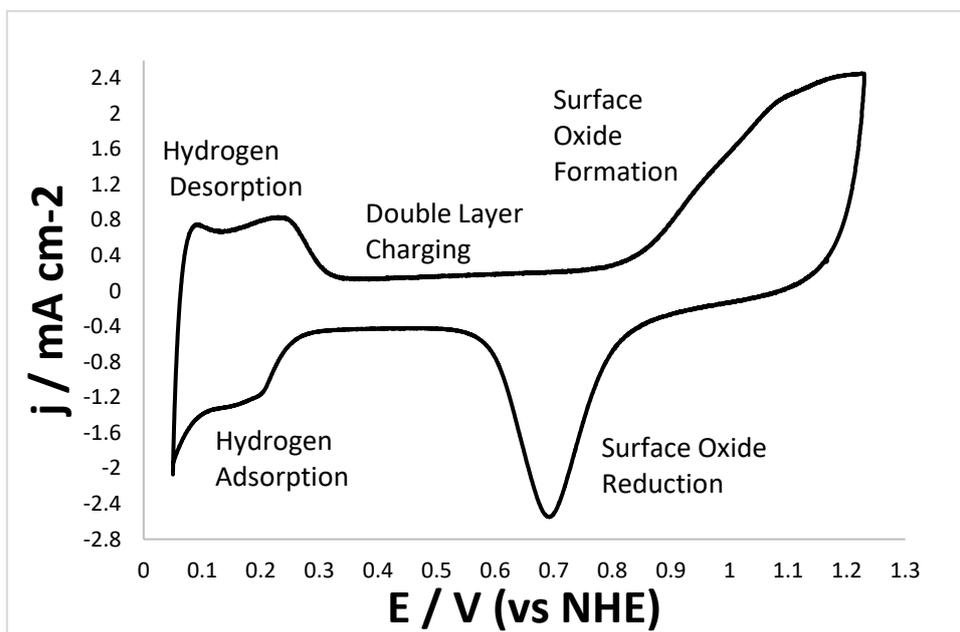
Figure 10: Cyclic voltammogram of Pd/C in N_2-saturated 0.5 M H_2SO_4 at a scan rate of 100 mVs^{-1}.

Cyclic voltammograms recorded for the three catalysts (Pd/C, PdAu/C and Pd_3Au/C) at a scan rate of 20 mVs^{-1} are shown in Figure 11. The overall shape of CVs obtained for the two palladium-gold catalysts were similar to that recorded for the palladium on carbon catalyst. All three catalysts showed hydrogen adsorption and desorption peaks at low potentials (ca. 0.05 V to 0.3 V), double layer region (ca. 0.4 V to 0.7 V) and surface-oxide formation peaks (ca. 0.8 V to 1.2 V). No additional oxidation or reduction peaks were seen for the gold containing samples. This observation is in agreement with Hsu's work where the CVs obtained for their gold-palladium catalysts were similar to that of the palladium catalyst in acid[128]. In contrast to palladium, it has been reported that surface oxide formation starts at higher potential for gold and the actual oxidation peak for gold is observed at higher potentials ca. 1.4 V [129].

Although no redox peak is seen for gold in the PdAu/C and Pd_3Au/C CV, an increased anodic current was seen in the surface-oxide formation region between 0.9 V and 1 V in comparison to the palladium catalyst. A similar increase in anodic current in the surface-oxide formation region attributed to the start of surface oxide formation on gold has been reported for palladium-gold electrodes by Lukaszewski [130] and Hsu [128].Therefore, the increased anodic current

observed for PdAu/C and Pd$_3$Au/C was attributed to the onset of surface oxide formation on gold.
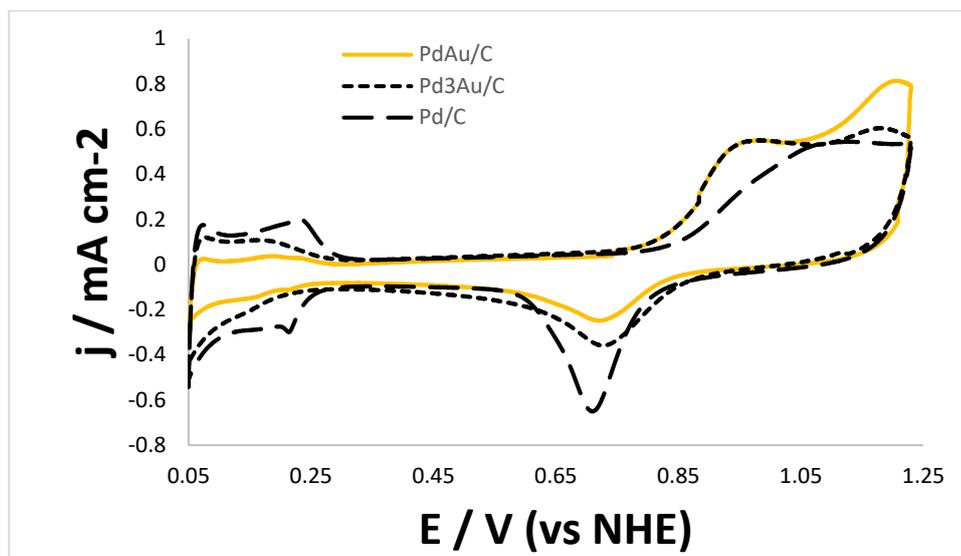
Figure 11: Cyclic voltammograms for PdAu/C, Pd$_3$Au/C and Pd/C catalysts in N$_2$-saturated 0.5 M H$_2$SO$_4$ at a scan rate of 20 mVs^{-1}.

In comparison to the Pd/C catalyst, the surface-oxide reduction peaks for the palladium-gold catalysts were observed to have shifted to higher potentials (from 0.71 V to 0.74 V for Pd/C). A similar shift has been previously reported by Lukaszewski and Czerwinsk [131] for their palladium-gold electrodes. This shift was attributed to the presence of gold in palladium-gold catalysts as discussed by Xing [132].

From the CVs shown in Figure 11, it can be observed that current associated with hydrogen adsorption and desorption reduced with decreasing amount of palladium in the catalysts. This decrease was thought to be because the current associated with the hydrogen peaks would only be due to palladium hydrogen desorption since gold electrodes have been reported to not show peaks corresponding to either hydrogen adsorption and desorption[133].

Electrochemical surface area (ECSA) were calculated for the three catalysts by integrating the charge under the palladium-oxide reduction peak and comparing it to the charge density of 420 µC cm^{-2} reported for the reduction of a monolayer of PdO on palladium [133]. The ECSA values obtained were 15.5, 6.2 and 2.5 m^{2}g^{-1} for the Pd/C, Pd$_3$Au/C and PdAu/C catalysts respectively. The catalyst Pd/C with the smallest particle size (5.4 nm) had the biggest ECSA, followed by Pd$_3$Au/C (6.8 nm). A relatively low value was obtained for PdAu/C, even though it had a similar average particle size (7.5 nm) to Pd$_3$Au/C (6.8 nm). This suggests that the higher amount of gold in the PdAu/C caused a reduction in the overall surface oxygen adsorbed and hence the

area under the oxide reduction peak used for ECSA measurement. Gold has been reported to hinder the hydrogen adsorption as well as oxide reduction on palladium [134]. This is consistent with Damjanovic's observation that in contrast to palladium, gold's surface has a low coverage of oxygenated-species at oxygen reduction potentials [135]. A decrease in the electrochemical surface area with increasing gold quantities in a series of PdAu/C catalysts has also been reported by Erikson [134].

The ECSA values were also obtained for commercial samples of 20 % Pd/C and 20% Pt/C as 25.8 and 57.2 m^2g^{-1} respectively. These samples were denoted PdCOM and PtCOM for the commercial palladium and platinum samples respectively.

3.6 Oxygen Reduction Activity Studies of Palladium-Gold Catalysts

Each catalyst's activity was evaluated from the onset potential, Tafel slope and exchange current density. These parameters determined for the synthesised catalysts were compared with results from commercially bought 20 % palladium on carbon (denoted PdCOM) and 20 % platinum on carbon (denoted PtCOM).

The open circuit potential (OCP) of each catalyst was measured as soon as the electrode was placed in the electrolyte (oxygen-saturated 0.5 M H_2SO_4). Three linear sweep voltammograms (LSV) were recorded from a potential 30 mV higher than OCP to a lower potential of 0.2 V a t a scan rate of 5 mVs^{-1}. All reported parameters were calculated from data obtained from the third voltammogram recorded.
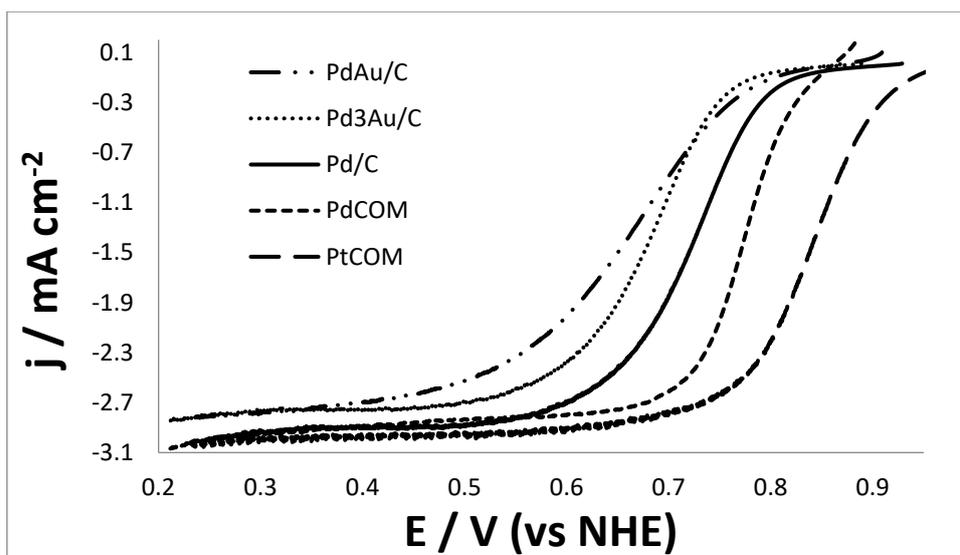
Figure 12: Linear sweep voltammograms for PdAu/C, Pd₃Au/C and Pd/C compared with the commercial palladium and platinum at 400 rpm and scan rate of 5 mVs⁻¹.

Figure 12 compares the linear sweep voltammograms recorded for the prepared PdAu/C, Pd$_3$Au/C and Pd/C catalysts alongside commercial 20 % Pd/C and 20 % Pt/C (PdCOM and PtCOM). All catalysts displayed the three regions typically associated with an ORR polarisation curve; the area under kinetic control, the mixed kinetic-diffusion area and the area under diffusion control. Low current densities were observed in the kinetic-control region; indicating slow ORR kinetics at high potential (ca. 0.9 V). The scans progressed to lower potentials, where the increase in reaction rates were observed as increasing current densities in the mixed control region (ca. 0.85 to 0.65 V). The increasing current densities reached a maximum for each catalyst in the diffusion-controlled region (ca. 0.5 V and lower). Onset potentials were 0.86, 0.87, 0.87 and 0.89 V for PdAu/C, Pd$_3$Au/C, Pd/C and PdCOM catalysts respectively. The commercial platinum catalyst had an onset of 0.97 V which was about 100 mV more positive than that of any of the palladium-based catalysts.

The commercial Pt/C gave the highest current at highest potentials overall as expected since platinum is widely reported in literature for its high ORR activity. Among the palladium-based catalyst, commercial Pd/C gave the best activity. Its higher activity is related to its higher ECSA compared to the other palladium-based catalysts. The PdAu/C had the lowest activity; this low activity is ascribed to the presence of higher amounts of gold present in the sample. Gold and gold based catalysts have been reported to possess low activity towards ORR [126].

3.7 Koutecky-Levich Analysis on Palladium-Gold Catalysts

ORR activity of different catalysts is often evaluated and compared using the Koutecky-Levich plots. Kinetic current and hence specific and mass activities of catalysts can be obtained from a plot of the inverse of overall current against the inverse of rotation speed. Data for the Koutecky-Levich plots is taken from a set of LSVs at different rotation rates so as to calculate the current without the mass-transport effect (kinetic current). The set of 5 consecutive LSVs obtained for Pd/C, PdCOM and PtCOM are shown in Figures 13, 14 and 15.

In contrast to the LSV obtained for the commercial Pt/C catalyst, Pd$_3$Au/C, prepared Pd/C and commercial palladium on carbon (PdCOM) presented very unstable voltammograms.
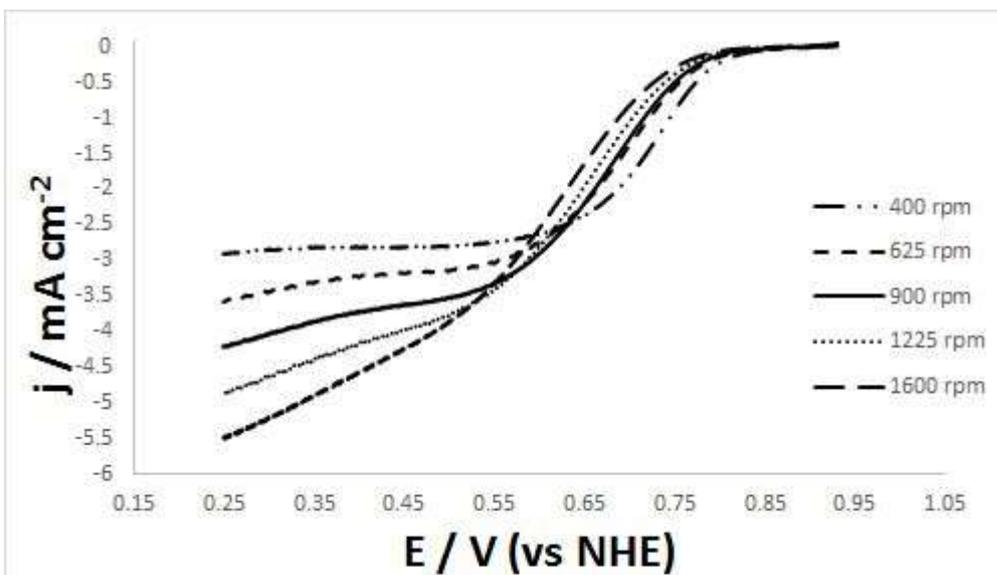
Figure 13: Linear sweep voltammograms for Pd/C catalyst at a scan rate of 5 mVs^{-1} and rotation rates of 400, 625, 900, 1225 and 1600 rpm.
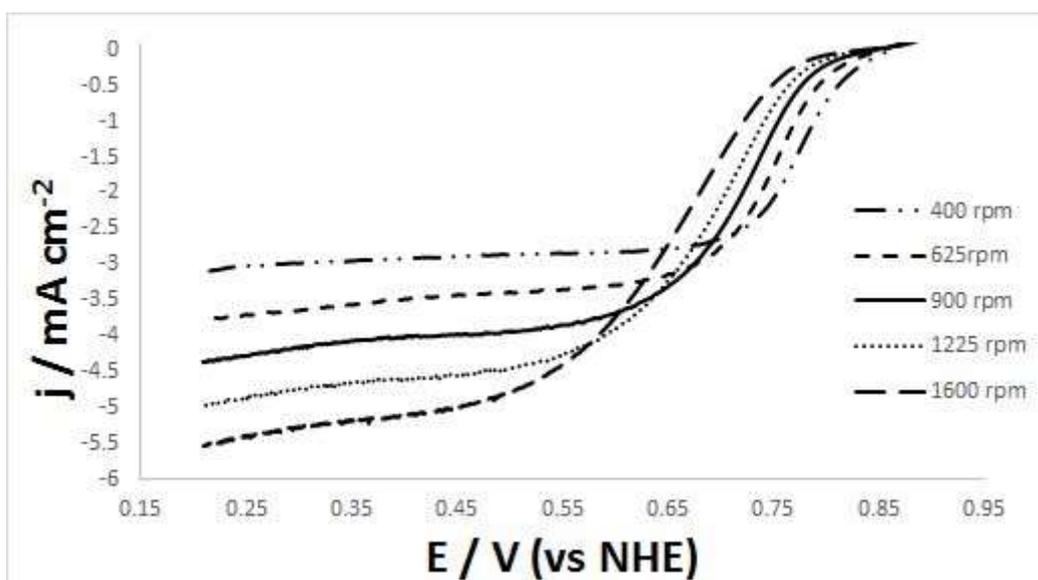
Figure 14: Linear sweep voltammograms for commercial palladium (PdCOM) catalyst at a scan rate of 5 mVs^{-1} and rotation rates of 400, 625, 900, 1225 and 1600 rpm.
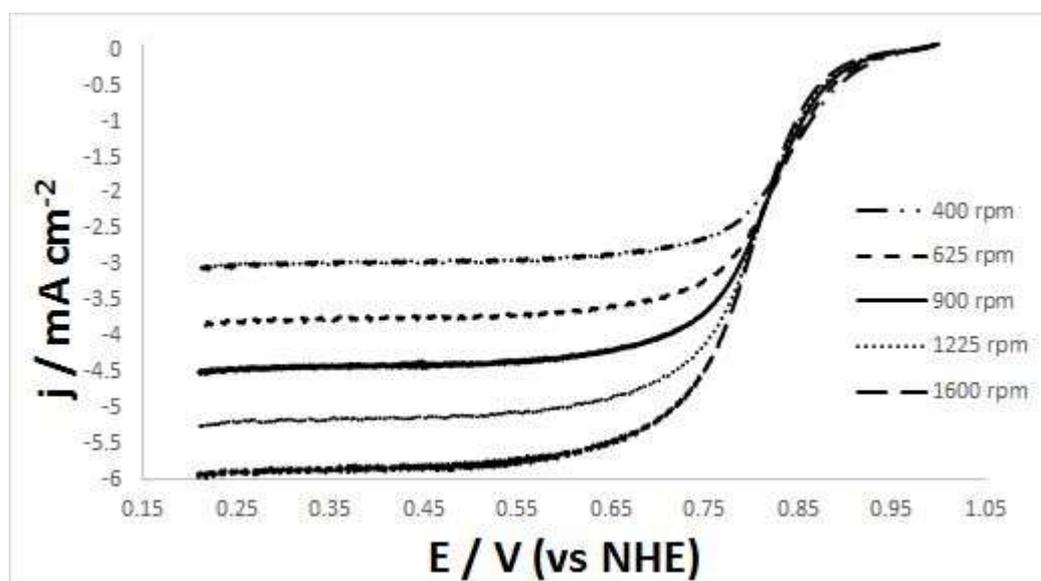
Figure 15: Linear sweep voltammograms for commercial platinum (PtCOM) catalyst at a scan rate of 5 mVs^{-1} and rotation rates of 400, 625, 900, 1225 and 1600 rpm.

It was observed that polarisation curves obtained for the catalysts with higher palladium ratios (Pd$_3$Au/C, Pd/C and commercial PdCOM) showed marked variations to the expected curves over the course of recording the set of 5 consecutive voltammograms as a result of rapidly decreasing electrochemical surface area. The loss of electrochemical surface area is indicative of the low stability of palladium-based catalysts in acid media. This resulted in the variations of successive polarisation curves; especially in the region under mixed kinetic and diffusion control. This is consistent with literature reports of palladium hayving a lower stability than platinum in acidic media [114, 136]. Villulas and Pires [137] reported a similar loss of activity and shape change during recording polarisation curves for a palladium catalyst. Koutecky-Levich analysis could not be done for these catalysts as any results obtained from these would be highly inaccurate due to the changes in activity observed in the mixed kinetic- diffusion region during recording of the polarisation curves.

3.8 Tafel Analysis of Palladium-Gold Catalysts

The Tafel plot describes the relationship between kinetic current density and overpotential. Therefore, Tafel analysis was used in evaluating the ORR activity of the catalysts to measure the rate of increase in overpotential with current density. The plot is obtained by plotting potential against the logarithm of mass transport corrected current density as shown in Figure 16 for the commercial platinum.

For this analysis, data points for the Tafel plots were taken from the recorded LSVs for the five catalysts (PdAu/C, Pd$_3$Au/C, Pd/C, PdCOM and PtCOM) at 400 rpm and scan rate of 5 mVs^{-1}.

A mass transport effect correction was applied to the current density values. All Tafel plots were linear and used to calculate the Tafel slope and exchange current density for each catalyst as shown in Table 7.
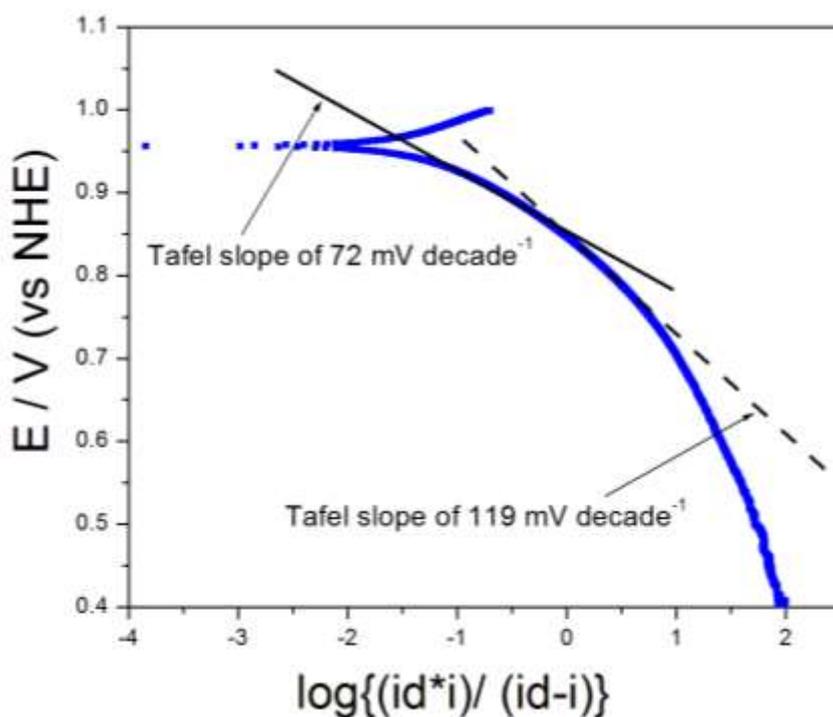
Figure 16: Tafel plot obtained for the commercial Pt/C catalyst showing two Tafel slopes of 72 and 119 mVdecade^{-1}.

The commercial platinum catalyst showed two Tafel slopes; 72 and 119 mV decade^{-1} at the low current density region (0.93 to 0.87 V) and high current density region (0.86 to 0.76 V) respectively as shown in Figure 16. Tafel slopes of 60 and 120 mV decade^{-1} are characteristic for ORR on platinum electrodes at low and high current density regions respectively[12, 138]. This change in Tafel slope has been attributed to changes in surface coverage of electrode by adsorbed oxygen intermediates, with Tafel slopes of 60 and 120 mV decade^{-1} obtained at high and low surface oxide coverage conditions respectively. An initial one electron transfer to oxygen molecule was reported to be the rate-determining step in both Tafel regions [139, 140].
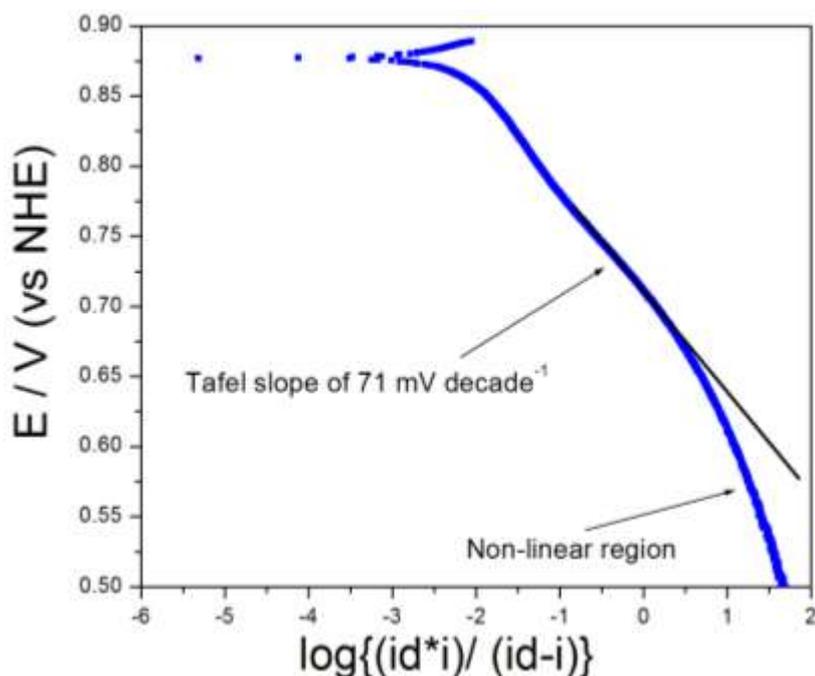
Figure 17: Tafel plot obtained for the Pd/C catalyst showing a single Tafel slope and a non-linear region.

The purely palladium catalysts (Pd/C and PdCOM) had single Tafel slopes close to 60 mV decade^{-1}; values of 60-70 mV decade^{-1} has been reported in literature for palladium and palladium-based catalysts in acid [37, 62, 67, 141]. The palladium catalysts had a single Tafel slope as a non-linear region was observed for palladium in the high current density region as shown in Figure 17. The linear region for the Pd/C was observed between 0.76 and 0.69 V, a non-linear region was observed at potentials lower than 0.69 V.

Oxygen reduction on palladium electrodes in H_2SO_4 has been reported to proceed via a mechanism similar to that of platinum since they both usually have the same Tafel slopes [15]. The low Tafel slope of 60 mV decade^{-1} was reported by Damjanovic *et al.* [135] to correspond to ORR taking place on an oxide-covered platinum electrode while Hoare[142] reported a Tafel slope of 102 mV decade^{-1} for ORR on a palladium electrode that had been oxidised and then reduced. This is consistent with Tafel slopes of 60 and 120 mV decade^{-1} obtained at high and low surface oxide coverage for platinum. Therefore, it can be concluded that the low Tafel slopes (71, 59 and 72 mV decade^{-1}) found for the Pd/C, PdCOM and PtCOM respectively were as a result of ORR taking place on the oxide-covered palladium and platinum while the second higher Tafel slope (119 mV decade^{-1}) for the commercial Pt/C catalyst was due to ORR on a mostly oxide-free platinum.

The palladium-gold catalysts (PdAu/C and Pd$_3$Au/C) exhibited single Tafel slopes of 61 and 72 mV decade^{-1} respectively. These values obtained are similar to those of Pd/C and PdCOM and were attributed to ORR taking place at high oxide coverage of the palladium surface.

Table 7: Tafel Slopes and exchange current density values obtained for PdAu/C, Pd$_3$Au/C, Pd/C, commercial Pd/C and Pt/C catalysts.

Catalyst	Tafel slope (mVdecade^{-1})	Exchange Current Density (Acm^{-2})
PdAu/C	61	3.7x10^{-14}
Pd$_3$Au/C	72	8.9x10^{-14}
Pd/C	71	6.2x10^{-12}
PdCOM	59	2.4x10^{-11}
PtCOM	72	5.5x10^{-10}
	119	4.2x10^{-8}

The exchange current densities were calculated by extrapolating the Tafel plots to the electrode equilibrium potential for each catalyst using the real or the electrochemical surface area. Pd$_3$Au/C had an exchange current density value about 2 times higher than the value obtained for PdAu/C. This could be due to the presence of higher amounts of palladium in Pd$_3$Au/C as palladium is more active for ORR than gold in acid. Exchange current density for commercial Pd/C catalyst was about 2 times higher than that of the prepared Pd/C catalyst with similar amounts of metal. This could be due to the larger particle sizes and hence a smaller ECSA on Pd/C .The value obtained for the commercial Pd/C was close to values reported by Alvarez *et al*. [113] and Gnanamuthu *et al*. [143] in order of (10^{-11} Acm^{-2}). The commercial Pt/C catalyst had the highest exchange current density as expected, with its exchange current density at the high current density region being about 1.5 times the order of magnitude of the commercial Pd/C. Exchange current density for the commercial Pt/C at high current density region (low oxide-coverage) was nearly twice the order of magnitude of its value in the low current density region (high oxide-coverage); indicating that ORR is more facile on the oxide-free platinum. A similar observation of a higher exchange current density at the high current density region (Tafel slope close to 120 mV decade^{-1}) for platinum has been reported in literature [37, 144].

The calculated exchange current density values for platinum are in good agreement with those reported in literature; in order of 10^{-7} and 10^{-10} Acm^{-2} at the high and low current density regions respectively [37, 145].

3.9 Quantification of Hydrogen Peroxide Generated for Palladium-Gold Catalysts

It is desirable for the catalysts to undergo oxygen reduction via a direct 4-electron route pathway and produce the lowest amount of hydrogen peroxide possible. While the oxygen reduction is ongoing at the disk, the platinum ring around the disk held at a voltage of 1.2 V oxidises the generated peroxide intermediates to oxygen. Therefore, this current associated with peroxide oxidation occurring on the platinum ring(ring current) can be used to monitor, quantify and compare the amounts of peroxide intermediates produced during ORR for each catalyst [146].The ring current obtained for PdAu/C, Pd$_3$Au and Pd/C are shown along with those obtained for the commercial palladium and platinum catalysts at a rotation rate of 400 rpm in Figure 18. The Pt/C catalyst had the lowest ring current while the PdAu/C had the highest current meaning they produced the lowest and highest amounts of peroxide intermediate respectively. Also, all the palladium and palladium-based catalysts generally had higher ring currents than Pt/C. PdAu/C had the highest amount of peroxide intermediates detected. This observation were not surprising as ORR on gold electrodes have been reported to proceed via the 2-electron pathway involving the production of peroxides [39] in acidic media.
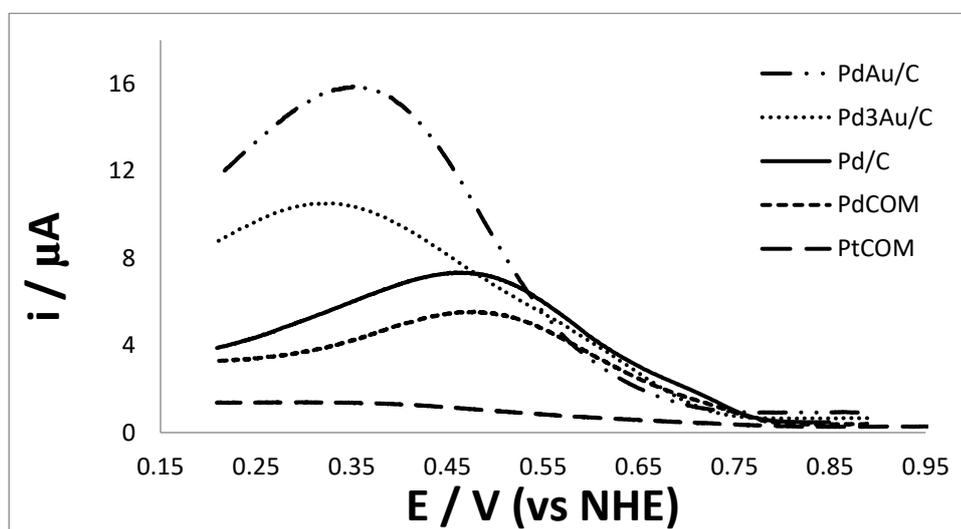
Figure 18: Ring currents obtained for the PdAu/C, Pd$_3$Au/C and Pd/C catalysts compared with the commercial palladium and platinum at 400 rpm and a scan rate of 5 mVs^{-1}.

The percentage of peroxide produced during the ORR was quantified from Equation 3.1.

% H$_2$O$_2$ = 2x (I$_R$/N)/I$_D$+ I$_R$/N $\hspace{4cm}$ (3.1)

Where I_R is the ring current, I_D is the disk current and N is the collection efficiency 37 % (as supplied by manufacturer). The percentage peroxide generated were measured at 0.4 V. The percentage peroxide produced were 2.1 %, 7.1 %, 7.9 %, 21.3 % and 35.7 % for the PtCOM, PdCOM, Pd/C, Pd_3Au/C and PdAu/C catalysts respectively. The percentage peroxide generated by ORR on platinum has been reported to be around 2 % [147] and 7 % for palladium on Vulcan [148]. Palladium based catalysts have been reported to generally produce more peroxide intermediates than platinum [149].

3.10 Cyclic Voltammetry (CV) Stability Studies of Palladium-Gold Catalysts

Cyclic voltammetry was used for studying the stability of the three catalysts. This was done by recording 100 consecutive cyclic voltammograms for each catalyst at a scan rate of 100 mVs^{-1} from 0.05 V to 1.2 V in nitrogen. The results were compared to results obtained from using commercial 20 % Pd/C (PdCOM) and 20% Pt/C (PtCOM). The effect of this cycling on the ECSA was monitored to provide information on catalyst stability. The more stable catalyst was expected to retain a higher percentage of its initial ECSA after cycling.
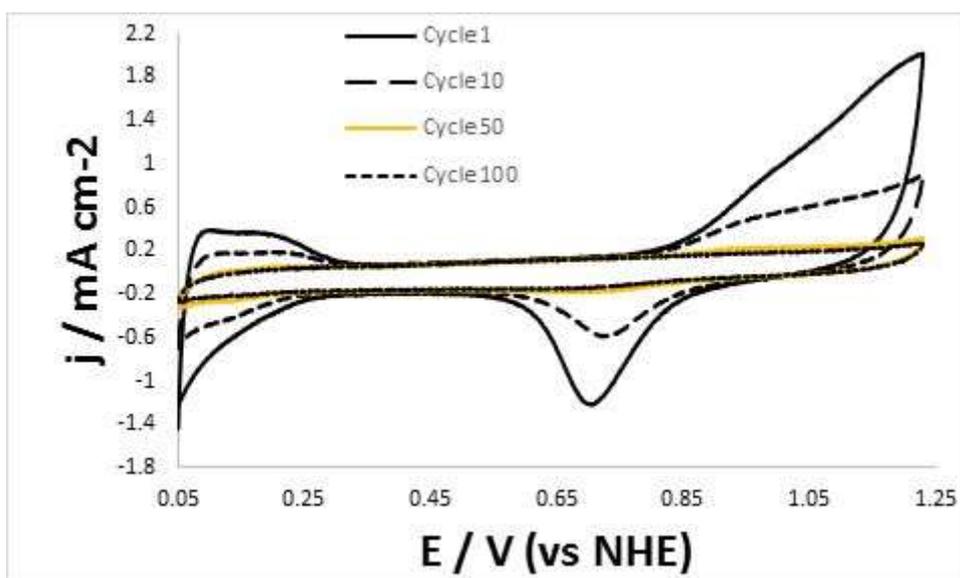
Figure 19: First, tenth, fiftieth and hundredth cyclic voltammograms obtained for PdAu/C catalyst during 100 cycles recorded at 100 mVs^{-1}.

During the 100 cycles for PdAu/C (voltammograms shown in Figure 19 for cycles 1, 10, 50 and 100), a dramatic change was observed in the overall shape of the CVs. In the first 10 cycles, a significant decrease in peak size was seen in hydrogen adsorption and desorption area as well as in the oxide reduction area. The catalyst had lost most of its palladium electrochemical features by the fiftieth cycle. For its hundredth cycle, the recorded voltammogram showed electrochemical behaviour that was similar to a gold electrode; where no oxidative or reductive

current was observed at the potential range used for this study (0.05 to 1. 2 V v NHE). This is consistent with a similar change to a palladium-gold catalyst observed by Lukaszewski [131] during potential cycling in H_2SO_4. The authors attributed this behaviour to selective dissolution of palladium from the catalyst leading to a gold-enrichment on the surface. Li *et al.* also observed that segregation of gold to the surface of a palladium-gold catalyst as a result of gold's lower surface energy relative to palladium [150].
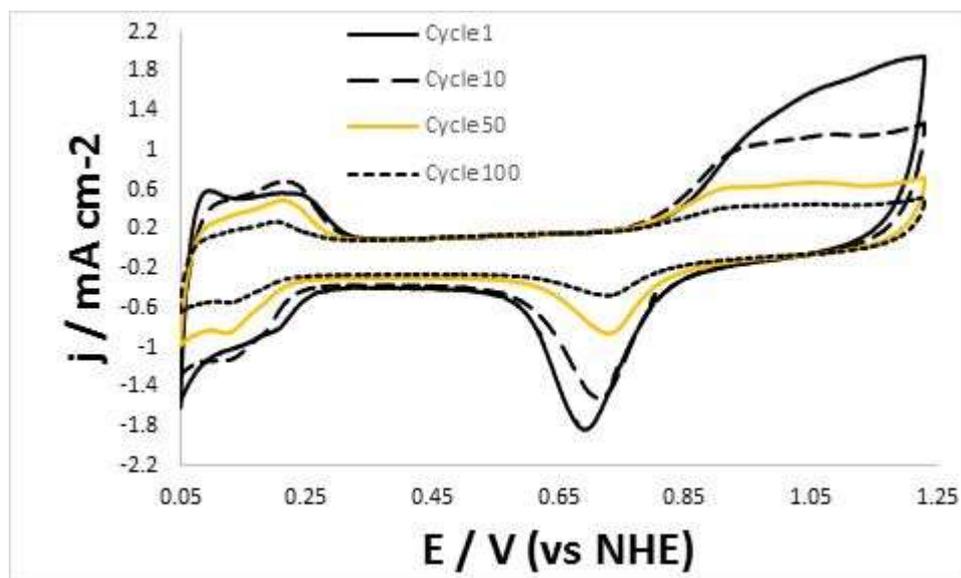
Figure 20: First, tenth, fiftieth and hundredth cyclic voltammograms obtained for Pd₃Au/C catalyst during 100 cycles recorded at 100 mVs⁻¹.

A continuous decrease of current was observed in the areas corresponding to hydrogen adsorption/desorption and oxygen reduction for Pd_3Au/C as shown in Figure 20 from the first to the last cycle. Although the characteristic palladium peaks in the catalyst decrease in size, they are still visible through to the hundredth cycle. This is in contrast to the PdAu/C catalyst that had lost all its palladium features after the first 50 cycles.
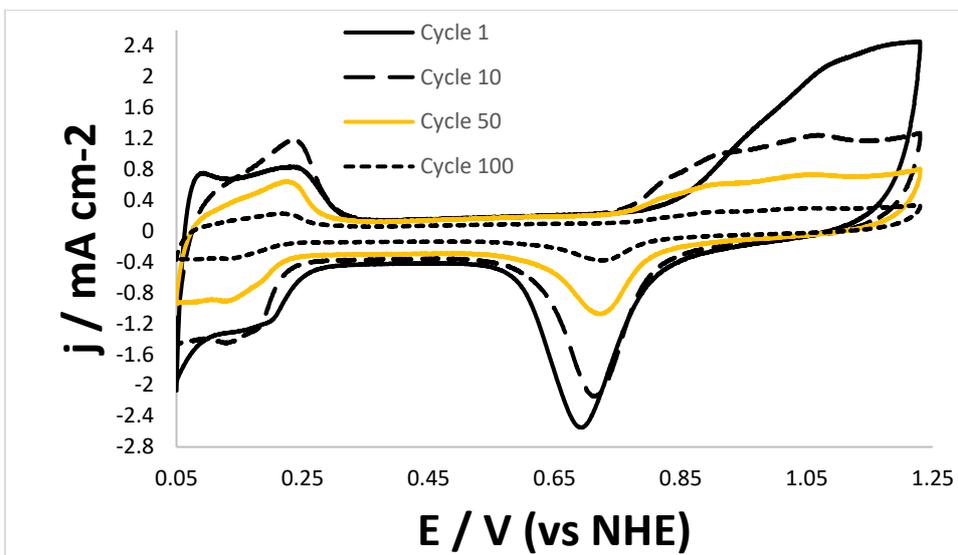
Figure 21: First, tenth, fiftieth and hundredth cyclic voltammograms obtained for prepared Pd/C catalyst during 100 cycles recorded at 100 mVs^{-1}.
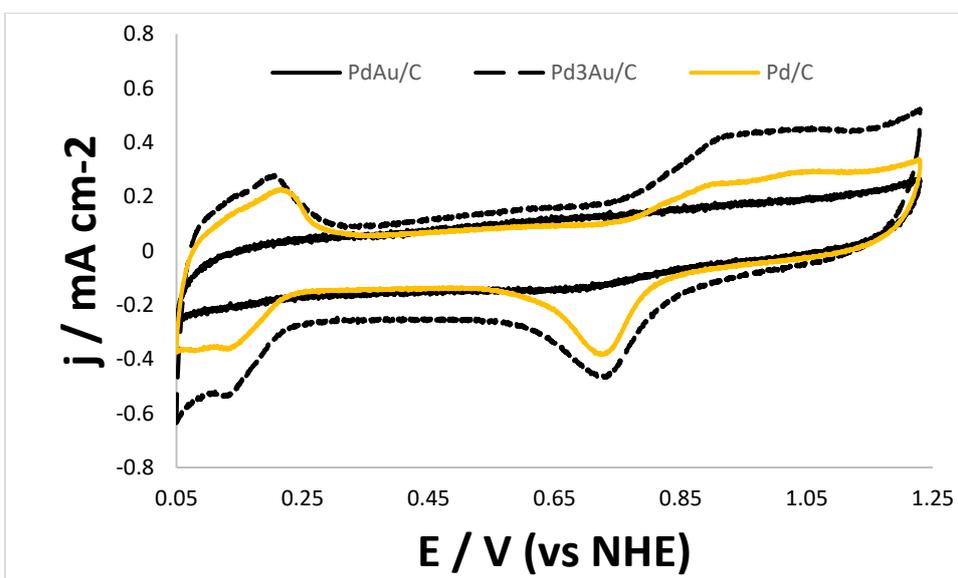
Figure 22: An overlay of the hundredth cyclic voltammogram obtained for PdAu/C, Pd$_3$Au/C and Pd/C catalysts recorded at 100 mVs^{-1}.

The hundredth cyclic voltammograms obtained for the three prepared catalysts; PdAu/C, Pd$_3$Au/C and Pd/C are shown in Figure 22 for ease of comparison. It was observed that Pd$_3$Au/C and Pd/C presented similar CV profiles; both characteristic of a palladium on carbon catalyst indicating that both catalysts maintained their palladium redox features during the potential cycling from 0.05 to 1.2 V. It was also observed that Pd$_3$Au/C had higher redox currents in the hydrogen adsorption and desorption area as well as in the oxide reduction area compared to Pd/C indicating a lower rate of redox current degradation during the potential cycling test and hence is a more stable catalyst than Pd/C. The higher cycling stability observed in Pd$_3$Au/C

compared to Pd/C was attributed to the presence of gold in the sample. A similar stabilization effect by the addition of small amounts of gold to palladium and platinum ORR catalysts has been observed in the literature [123, 151]. Sasaki *et al.* [126] reported an enhancement in ORR stability for a platinum monolayer deposited on palladium-gold nanoparticles catalyst compared to a platinum monolayer deposited on palladium nanoparticles, the authors suggested that gold may inhibit platinum dissolution and hence stabilise the catalyst.

In contrast to Pd_3Au/C and Pd/C, the CV recorded for PdAu/C at the hundredth cycle presented a different profile; a profile with no defined redox features which is similar to that of gold electrodes in acidic media at the potential range used in this study [150, 152]. The loss of the initially-present palladium features in PdAu/C was attributed to an enrichment of gold on surface [152]. Although both PdAu/C and Pd_3Au/C contain gold which could modify palladium's electrochemical behaviour, they exhibited different electrochemical behaviour under cycling where Pd_3Au/C maintained its palladium redox features and PdAu/C behaved more like a gold electrode. This difference in electrochemical behaviour was attributed to the higher ratio of gold to palladium in PdAu/C compared to Pd_3Au/C especially because palladium and gold were not alloyed in the samples, as deduced from the XRD data.
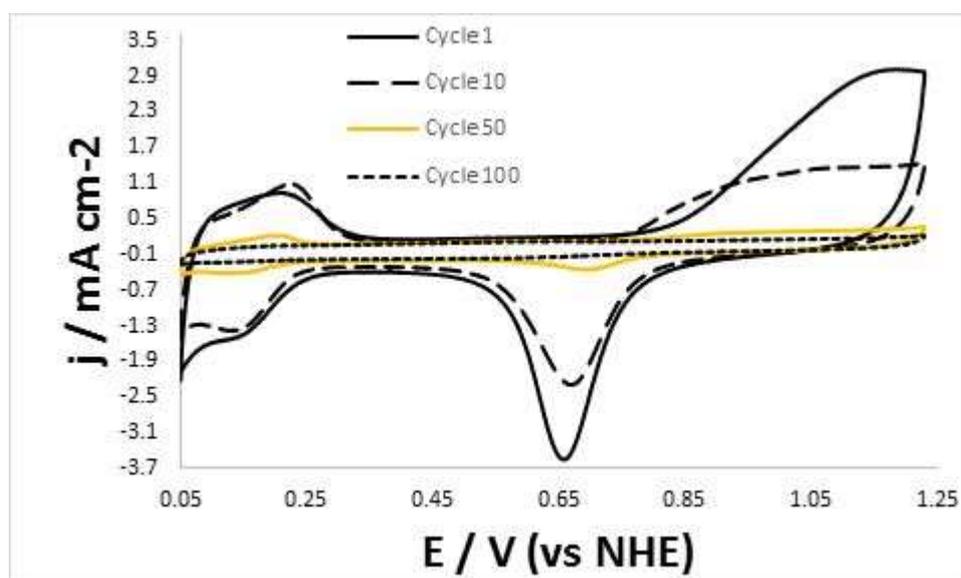
Figure 23: First, tenth, fiftieth and hundredth cyclic voltammograms obtained for commercial 20 % palladium on carbon catalyst during 100 cycles recorded at 100 mVs^{-1}.

For the two pure palladium-based catalysts (prepared Pd/C and commercial Pd/C), significant changes to the CVs and ECSA values were observed in the 100 scans as shown in Figures 21 and 23. A decrease in peak intensities was also observed in areas corresponding to hydrogen adsorption and desorption, surface-oxide formation and surface-oxide reduction for both catalysts. In addition to these changes, the peaks corresponding to the surface-oxide reduction

shifted to slightly higher potentials (ca. 50 mV) in the CVs obtained for the hundredth cycle for both catalysts. This is indicative of increasing particle size during the potential cycling. A similar potential increase in the position of the oxide-reduction peak has been reported for palladium [153] as well as platinum [154] and attributed to particle size increase in both cases.

Although, the ECSA loss appears to be greater for the commercial Pd/C (91 %) than the prepared Pd/C (78 %). This was thought to be as a result of the commercial catalyst having a smaller average particle size (3.6 nm) than the prepared Pd/C catalyst (5.4 nm). Mittermeier *et al.* [153] observed that ECSA loss during potential cycling was inversely proportional to particle sizes. In addition, they reported that no stable particle size was found after they tested series of Pd/C catalysts (3 to 9 nm); all the catalysts lost essentially all of their ECSA over the course of recording 2000 potential cycles between 0.5 to 1.0 V. Therefore, the authors concluded that palladium was not suitable for use as an ORR catalyst in acid.

Tang *et al.* [155] also observed a similar decrease in ECSA during a degradation study of Pd/C. They found the ECSA loss to be due to a reduction in number of ORR active sites resulting from an increase in palladium oxides on palladium surface through cycling at high potentials (1.2V). Therefore, the surface area loss observed in this study was attributed to increase in size of palladium nanoparticles and electrochemical oxidation of palladium [73, 74, 153].
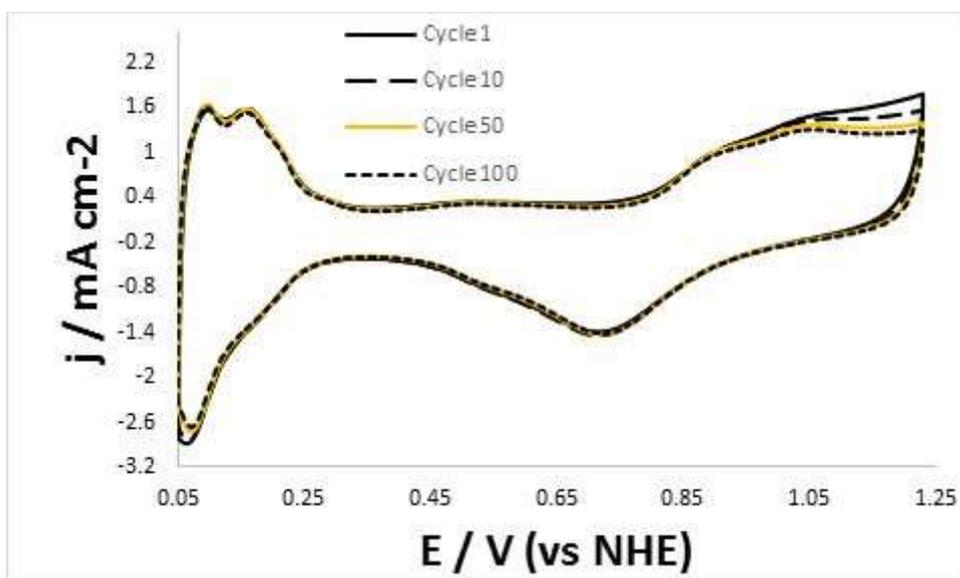
Figure 24: First, tenth, fiftieth and hundredth cyclic voltammograms obtained for commercial 20 % platinum on carbon catalyst during 100 cycles recorded at 100 mVs^{-1}.

In contrast to the platinum catalyst, the four palladium-based catalysts showed significant changes to the surface-oxides reduction peak during potential cycling. This shows that the palladium-based catalysts had a lower stability than platinum during the cycling tests. Platinum-

based catalysts have been reported to demonstrate higher stability than palladium-based catalysts in acidic media [115, 153, 156]. Each catalyst's stability was evaluated by measuring the loss of electrochemical surface area between the first and the last cycle; as a more stable catalyst would retain a higher percentage of its initial ECSA after cycling. The calculated percentages are shown in Table 8.

The commercial platinum catalyst was the most stable and retained 98 % of its initial ECSA. The palladium on carbon catalysts (commercial Pd/C and prepared Pd/C) were the most unstable; retaining only 9 % and 22 % of their initial ECSA values. Pd_3Au/C and PdAu/C retained 58 % and 12 % of their initial ECSA respectively. In comparison with Pd/C, Pd_3Au/C retained a high percentage of its initial surface area value; suggesting the addition of gold can improve the stability of palladium. The improved stability was thought to be due to gold segregating to the catalyst surface during potential cycling [150] and protecting palladium from the harsh oxidative conditions. This protection can be maintained during the potential cycling since gold does not begin to oxidise in H_2SO_4 until ca. 1.32 V; which is outside the potential window (1.2 V upper limit) used in this study [73, 157]. Gold has been reported to impart additional stability to catalysts; Chen *et al.* [158] reported improved stability of a palladium-gold catalyst compared to a similarly synthesised purely palladium based catalyst. Kang [159] also observed improved stability of a PtAuNi/C catalyst. They attributed the enhancement to gold's high corrosion-resistance and its ability to form a passivating layer that reduces the oxidation and dissolution of other less stable species in the catalyst; improving the overall durability of catalyst.

Table 8: ECSA values, average particle sizes and ECSA retained after cycling in nitrogen for PdAu/C, Pd_3Au/C, Pd/C, PdCOM and PtCOM catalysts.

Catalyst	Average Particle Size (nm)	ECSA (m^2g^{-1})	ECSA retained after 100 cycles (%)
PdAu/C	7.5	2.5	12
Pd_3Au/C	6.8	6.2	58
Pd/C	5.4	15.5	22
PdCOM	3.6	25.8	9
PtCOM	2.4	57.2	98

3.11 Chronoamperometry Studies of the of Palladium-Gold Catalysts

The stability of PdAu/C, Pd$_3$Au/C and Pd/C were evaluated using chronoamperometry. Chronoamperometry can be used for monitoring the decay of ORR current at a specific potential over time. The holding potential was each catalyst's half-wave potential since they exhibited very different activities. Current was monitored over two hours at a rotation rate of 900 rpm while maintaining a gentle oxygen flow into the electrolyte. The catalyst stability was evaluated from the ratio of its final current (at 2 hours) to initial current (taken at 10 seconds). The obtained current-time plots for the catalysts are shown in Figure 25 along with those obtained for the commercial palladium and platinum. The plot shows a normalized current, where 100 % is the initial current at 10 seconds for each catalyst.
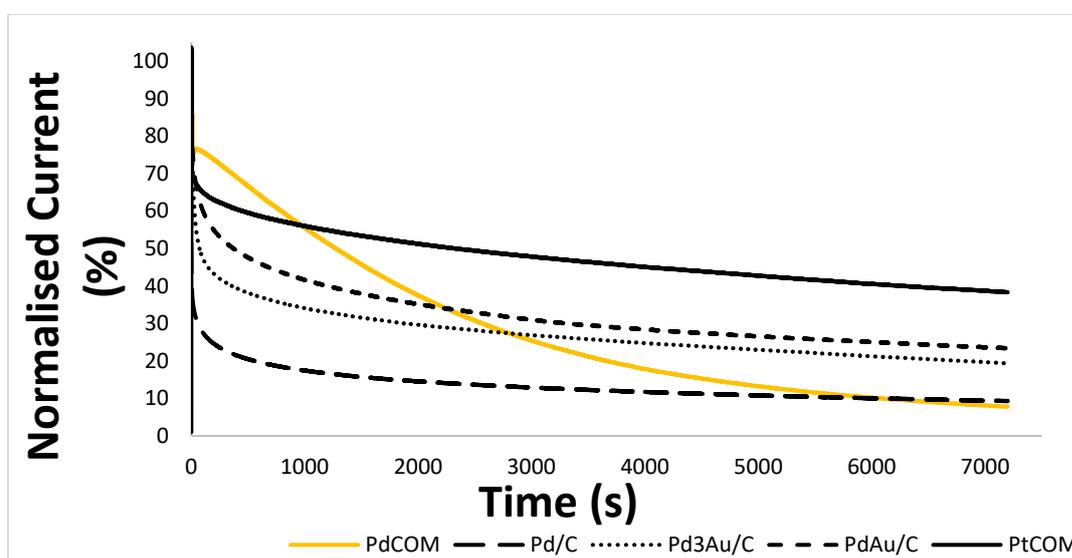
Figure 25: Chronoamperometric response curves obtained for PdAu/C, Pd$_3$Au/C, Pd/C, PdCOM and PtCOM catalysts based on normalising each catalyst's initial current to 100 %.

From Figure 25, a decay of current was observed for all catalysts. Percentages of ORR current retained were 38 %, 31 %, 16 %, 13 % and 63 % for PdAu/C, Pd$_3$Au/C, Pd/C, PdCOM and PtCOM catalysts respectively. The commercial platinum, followed by PdAu/C exhibited the highest stability. It was observed that PdAu/C showed a higher stability under chronoamperometry than the potential cycling test. This was thought to be due to the ECSA being used a measure of stability in the potential cycling test; PdAu/C's loss of ECSA was attributed to an enrichment of gold on the surface. The other results were in good agreement with the trend observed in the potential cycling test monitoring the ECSA loss during the cycling.

3.12 Conclusions

Palladium and palladium-gold catalysts were successfully synthesised via a polyol method. The average particle sizes were 7.5 nm, 6.8 nm and 5.4 nm for PdAu/C, Pd$_3$Au/C and Pd/C catalysts respectively. XRD analysis revealed the presence of two individual palladium and gold phases with no alloying between the metals. Electrochemical characterisation revealed a palladium-rich surface on all catalysts initially. Initial cyclic voltammograms of the palladium-gold catalysts revealed a similar redox behaviour to palladium; hydrogen adsorption and desorption peaks at low potentials (ca. 0.05 V to 0.3 V), double layer region (ca. 0.4 V to 0.7 V) and surface-oxide formation peaks (ca. 0.8 V to 1.2 V). The electrochemical surface areas obtained were 15.5, 6.2 and 2.5 m^{2}g^{-1} for the Pd/C, Pd$_3$Au/C and PdAu/C catalysts respectively.

Linear sweep voltammograms showed onset potentials of 0.86, 0.87, 0.87 V for PdAu/C, Pd$_3$Au/C and Pd/C. It was observed that polarisation curves for Pd$_3$Au/C, prepared Pd/C and commercial Pd/C showed marked variations to the expected curves over the course of recording the set of 5 consecutive voltammograms as a result of rapidly decreasing electrochemical surface area. Therefore, kinetic current and hence specific and mass activities could not be calculated for these catalysts. Pd/C, Pd$_3$Au/C and PdAu/C exhibited single Tafel slopes around 60 mV decade^{-1} associated with ORR taking place at high oxide coverage of the palladium surface. The ORR activity was found to decrease with increasing amounts of gold in catalysts. The exchange current densities calculated for Pd$_3$Au/C and PdAu/C were in the order of 10^{-14}, about 2 times lower in magnitude than values obtained for Pd/C catalysts (10^{-12}). The palladium-gold catalysts produced about 5 times the amount of peroxides during ORR when compared with the pure palladium catalysts.

Potential cycling from 0.05 to 1.2 V was used to evaluate the catalysts stability over 100 cycles. PdAu/C lost most of its palladium electrochemical features by the fiftieth cycle and showed no oxidative or reductive currents by the hundredth cycle. This was associated with an enrichment of gold on its surface. Severe ECSA losses of 78, 91, 88 and 42 % were observed for prepared Pd/C, commercial Pd/C, PdAu/C, and Pd$_3$Au/C respectively. These ECSA loses were attributed to oxidation of the palladium surface due to repeated potential cycling to a relatively high potential of 1.2 V.

 The higher stability of Pd$_3$Au/C suggested the addition of gold can improve palladium's stability. The improved stability was attributed to gold segregating to the catalyst surface during potential cycling and protecting the palladium from the harsh oxidative conditions. The most stable catalyst was the commercial Pt/C catalyst with only a 2 % loss of ECSA observed.

Evaluation of stability by chronoamperometry showed percentages of ORR current retained 38 %, 31 %, 16 %, 13 % and 63 % for PdAu/C, Pd$_3$Au/C, Pd/C, commercial Pd/C and commercial Pt/C catalysts respectively. PdAu/C presented the highest stability; a result that was different to the initially-observed trend when ECSA was used for the evaluation. This was because PdAu/C's loss of ECSA was also associated with an enrichment of gold on the surface rather than just palladium oxidation.

From these experiments, the addition of gold to palladium was observed to be beneficial to improving palladium's stability in acid media. This enhancement of stability was attributed to a surface segregation of gold and its ability to protect palladium from oxidation. However, a reduction in activity was also observed especially with increasing ratio of gold in the catalysts. Therefore, further work is needed into maintaining palladium's activity in the presence of gold.

Chapter 4. Palladium-Iridium Particles as Oxygen Reduction Catalysts

4.1 Introduction

Although iridium is more commonly used as anode catalysts for the oxygen evolution reaction [160, 161], it has been found to be useful in oxygen reduction reactions as well [162]. This is due to iridium being cheaper than platinum and possessing excellent electrochemical stability in acid [163]. Iridium is a platinum group metal sharing some similar properties with platinum; atomic sizes, face-centred cubic crystal structures and high dissolution potentials [164] (Ir/Ir^{3+} 1.16 V and Pt/Pt^{2+} 1.18 V). Iridium has also been reported to undergo oxygen reduction via the highly preferred 4-electron reduction pathway [165].

In contrast to platinum, Ir/C has been reported to have low ORR activity [166]. The authors reported a kinetic current density of 0.1 $mAcm^{-2}$ and 13.9 $mAcm^{-2}$ at 0.8 V for Ir/C and Pt/C respectively in H_2SO_4. They also reported that modification of the Ir/C catalyst with cobalt resulted in improved activity and doubling of the kinetic current density was observed. Li *et al.* [167] also reported an enhancement in iridium's ORR activity by its modification with vanadium. The authors observed a maximum power density of 517.2 mW cm^{-2} for Ir-V/C catalyst; about 1.5 times higher than that obtained for a pure Ir/C catalyst. Although there was an improvement in Ir-V/C, its power density was only 77 % of that recorded for Pt/C under the same conditions. This ORR improvement in Ir-V/C was attributed to reduced Ir-Ir distances in the catalyst and the presence of other elements (vanadium in this case) being able to modify iridium's surface and electronic properties.

Therefore, iridium is not typically used as the main metal for ORR catalysis. It is often used as co-catalyst alongside other metal such as platinum and palladium. Platinum-iridium alloys [162, 164, 168] have been reported to show enhanced ORR activity compared to platinum. The improvement in activities were attributed to the presence of iridium in the catalysts weakening the adsorption strength of OH, reducing OH-coverage and thus improving ORR activity of platinum.

Iridium nanoparticles decorated on platinum-palladium core- shell nanoparticles have been found to improve the activity and stability during ORR in a fuel cell when compared to Pt/C [169]. The authors reported a 24 % increase in maximum power density (792.2 mW cm^{-2} at 70 °C). During potential cycling of 40,000 cycles, the iridium decorated Pt/C catalyst lost only 32 % of its ECSA while the Pt/C had lost 50 %.

In contrast to the usually reported nanoparticles, Yang *et al.* synthesised nanowire alloys (1.5-2 nm) of palladium and iridium[170]. They attributed changes in shapes of CV obtained (a flattening of the Pd-O reduction peak) to a protection of palladium with iridium through alloying. An enhancement in stability of PdIr/C compared to commercial Pt/C catalyst was reported. The PdIr/C lost 33 % mass activity while the commercial Pt/C lost 65 % under the same degradation conditions at 0.9 V. Another report of palladium-iridium nanocrystals was made by the same authors [171]. A similar observation of improved catalytic stability was observed in a fuel cell with a Pd_2Ir/C nanocrystal losing only 6 % ECSA and 12 % mass activity compared to 42 % and 58 % loss for the commercial Pt/C after 10,000 cycles. This improved durability was attributed to iridium's existence in the sub-surface layer altering palladium's surface electronic structure, lowering the activation energies of O/OH hydrogenation and thus protecting palladium from dissolution losses.

These studies have shown the beneficial effects of modifying ORR metal catalysts with iridium. Therefore, iridium was chosen to alloy with palladium with a view of enhancing palladium's stability during oxygen reduction. From its Pourbaix diagram [172], it can be observed that iridium is stable under the test conditions for fuel cells; low pH and high potentials. A ternary catalyst with palladium, iridium and gold was also studied as gold was found to enhance palladium's stability in the previous chapter (Chapter 3).

4.2 Synthesis of Palladium-Iridium Catalysts

To prepare the PdIr/C catalyst, appropriate amounts of $(NH_4)_2PdCl_4$ and $IrCl_3.3H_2O$ were dissolved in 10 mL sodium citrate solution. A ternary palladium-iridium-gold catalyst (PdIrAu/C) was also prepared using appropriate amounts of $(NH_4)_2PdCl_4$, $IrCl_3.3H_2O$ and $HAuCl_4.3H_2O$ dissolved in 10 mL sodium citrate solution. The exact amounts used for each catalyst are shown in Chapter 2.

This mixture was added dropwise to a heated flask containing a nitrogen-saturated sonicated suspension of 200 mg Vulcan in 75 mL ethylene glycol at 140 °C. The reaction was maintained at this temperature for 3 hours. The solution was allowed to cool down naturally and each carbon-supported catalyst was separated from the reaction solution by centrifuging. Catalyst was extensively washed with deionised water and ethanol. Catalyst was dried at 80 °C in the oven overnight and ground with a mortar.

Palladium catalyst (Pd/C) prepared and discussed in Chapter 3 will be used for comparison purposes.

4.3 X-ray Diffraction (XRD) Analysis of Palladium-Iridium Catalysts

The X-ray diffraction patterns of the PdIr/C, PdIrAu/C and Pd/C catalysts are shown in Figure 26. The broad peak at 25° was assigned to carbon for all catalysts [173]. The diffraction peaks at 2θ values of ca. 40.1°, 46.5°, 68.2° and 81.9° were attributed to the (111), (200), (220), and (311) crystal planes of palladium respectively [113] for the three catalysts. Although no peaks relating to iridium or iridium oxide were observed, slight shifts towards higher 2θ angles were noted for the PdIr/C and PdIrAu/C catalysts. This suggests a lattice interaction between palladium and iridium. This is in good agreement with observation of higher Bragg angles reported by Bao *et al* [173] and Kim *et al.* [174]. The higher Bragg angles reported for the PdIr/C catalysts were attributed to a lattice contraction caused by incorporation of iridium with a lower d-spacing (0.2217 nm) into palladium (0.2246 nm). The diffraction pattern obtained for the ternary PdIrAu/C catalyst was similar to that of the palladium-iridium catalysts. No additional peaks relating to gold phases were observed. This could be due to the low ratios of gold (3 %) to palladium and iridium used in the ternary catalyst.

The average crystallite sizes of the catalysts were estimated from the full-width at half maximum of the (220) peak using the Scherrer equation. The calculated sizes were 5.6 nm and 4.8 nm for PdIr/C and PdIrAu/C catalysts respectively. These sizes are similar in value to 4.3 nm calculated for the Pd/C catalyst.
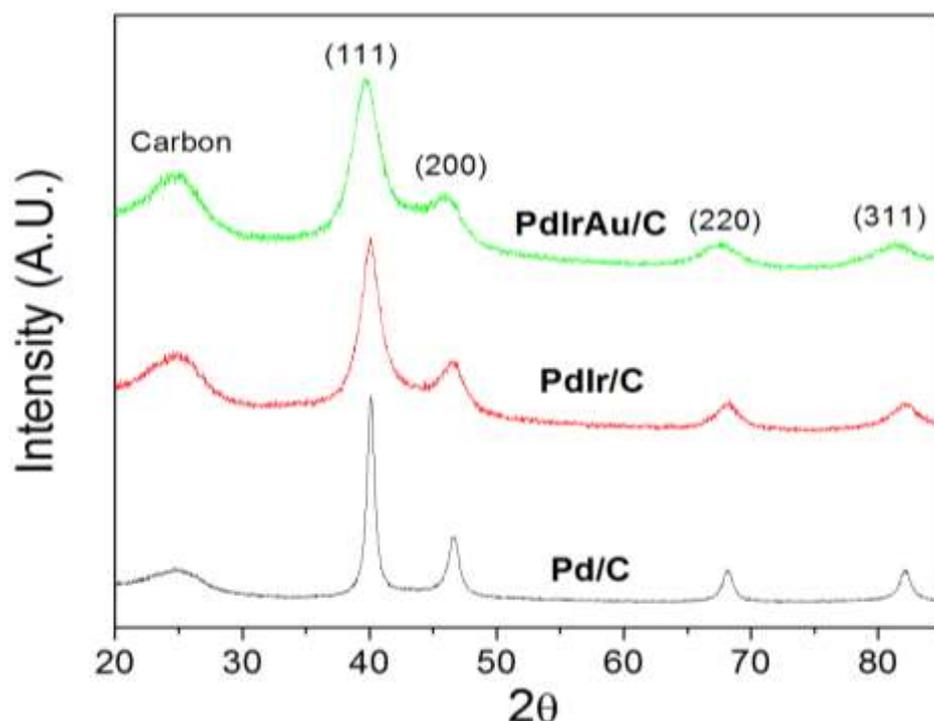
Figure 26: X-ray diffraction patterns obtained for PdIr/C, PdIrAu/C and Pd/C catalysts.

4.4 TEM and EDX Characterisation of Palladium-Iridium Catalysts

The obtained TEM images for PdIr/C and PdIrAu/C catalysts showed that spherical metal particles were dispersed on the carbon support without much agglomeration. The images obtained for PdIr/C and PdIrAu/C are shown in Figures 27 and 28. The particle size distribution was obtained by measuring the sizes of more than 100 randomly selected particles from the TEM images.
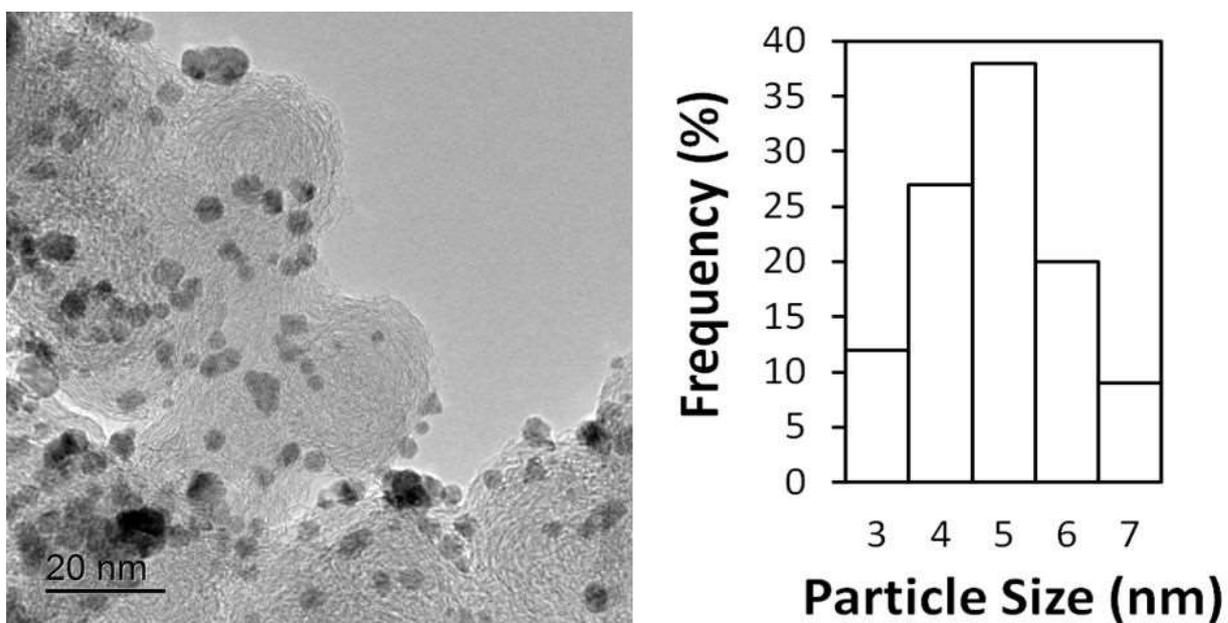
Figure 27: TEM image obtained for PdIr/C and its corresponding particle size distribution.
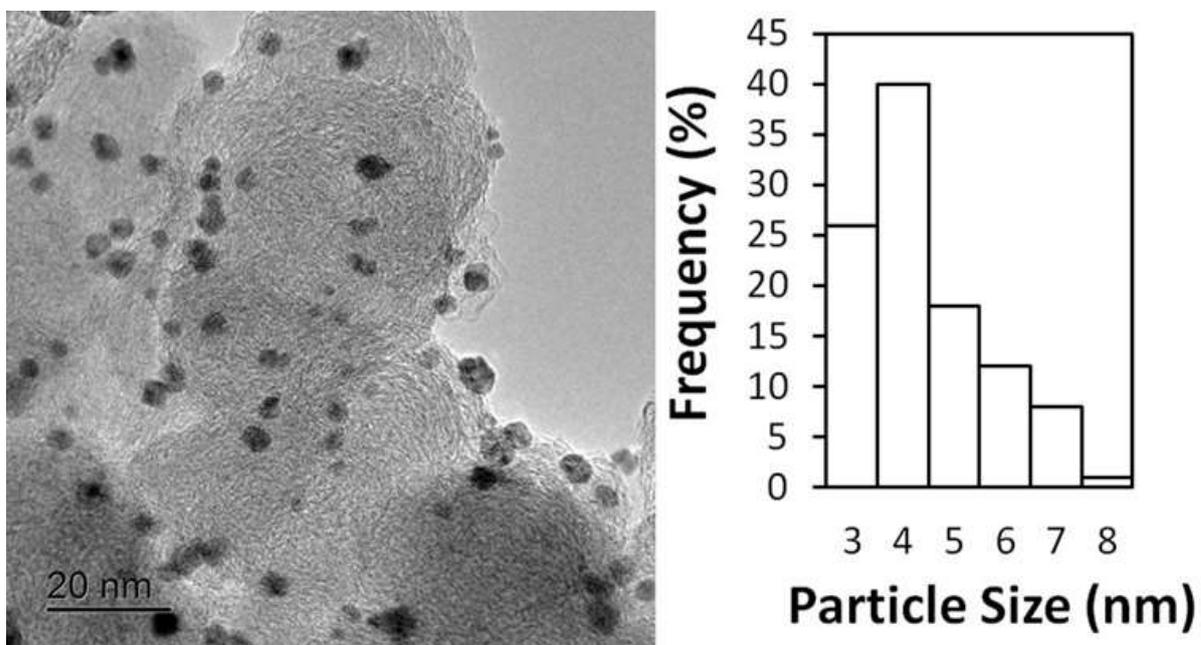
Figure 28: TEM image obtained for PdIrAu/C and its corresponding particle size distribution.

From the TEM images in Figures 27 and 28, it can be observed that PdIr/C and PdIrAu/C had narrow particle size distributions. The average particle size was calculated for both catalysts by measuring and taking the average of more than 100 particles. 5.2 nm and 4.8 nm were obtained as average particle size for PdIr/C and PdIrAu/C respectively. The measured average particle sizes were in good agreement with those calculated from the XRD peaks using the Scherrer equation.

High resolution images of single nanoparticles on PdIr/C, PdIrAu/C and Pd/C catalysts were also obtained. Fast Fourier transform was used to measure the lattice space. In Pd/C catalyst, the interplanar spacing between the lattice planes was 0.2224 nm. This corresponded to the (111) plane of face-centred cubic palladium. A slightly larger spacing of 0.2227 nm was measured in the PdIr/C catalyst. This is in good agreement with data from XRD analysis suggesting the interaction between palladium and iridium led to changes in lattice spacing. Similar measurement of lattice parameter of a palladium-iridium alloy was reported by Bao *et al*[173].
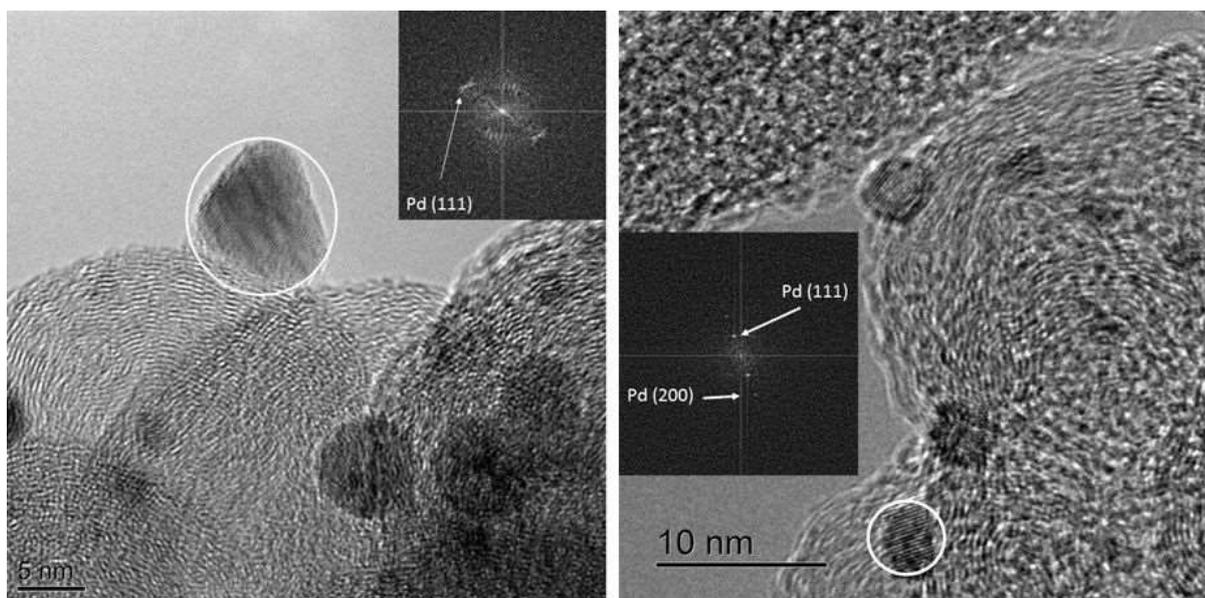
Figure 29: High resolution image obtained for Pd/C and PdIr/C showing lattice planes for palladium.

As shown in Figure 30 below, 2 distinct lattice spaces were observed in the HRTEM image for the PdIrAu/C; (0.2226 nm corresponding to a slightly larger Pd (111) as observed and discussed for the PdIr/C catalyst) and 0.2361 nm for Au (111). These values were obtained on two individual particles suggesting a stronger interaction between palladium and iridium and minimal interaction with gold.
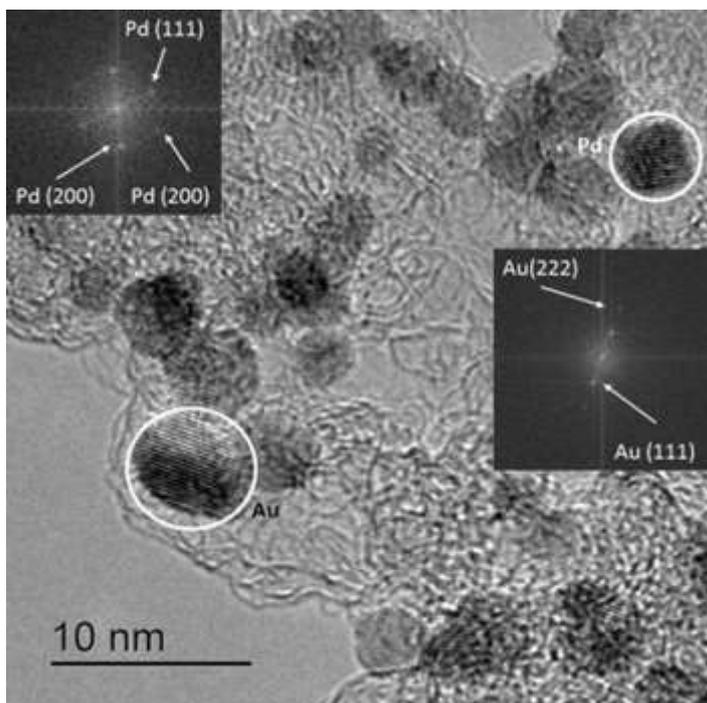
Figure 30: HRTEM image obtained for PdIrAu/C showing lattice planes of palladium and gold obtained on different particles.

The average weight percentages of metals in PdIr/C and PdIrAu/C from EDX measurements are presented in Table 9 below. The value for Pd/C is shown along for comparison. The values obtained were close to the expected values (20 % total metal weight on carbon); indicating a complete precursor reduction and deposition of metal particles on the support.

Table 9: EDX metal weight average, average particle sizes estimated from XRD and TEM Analysis for PdIr/C, PdIrAu/C and Pd/C catalysts.

Catalyst	XRD Estimated Crystallite Size (nm)	TEM Average Particle Size (nm)	EDX Metal Average		
			Pd (% wt.)	Ir (% wt.)	Au (% wt.)
PdIr/C	5.6	5.2	10.8	9.6	-
PdIrAu/C	4.6	4.8	11.6	8.5	3.4
Pd/C	4.3	5.4	21.4	-	-

4.5 X-ray Photoelectron Spectroscopy (XPS) Analysis of Palladium-Iridium Catalysts

XPS was used to analyse the oxidation state and surface composition of PdIr/C and PdIrAu/C. The Pd $3d$ spectra (Figure 31) of the PdIr/C showed 2 peaks that were resolved using 3 doublets. The binding energies of the Pd $3d_{5/2}$ peaks at 335.6 eV, 336.2 eV and 337.6 eV corresponded to metallic Pd^0, palladium with oxygen adsorbed (PdO_{ads}) and palladium II oxide respectively (PdO) [175, 176]. The compositional analysis of the palladium peaks show that the Pd^0, PdO_{ads} and PdO were in a relative ratio of 89.2%, 2.3% and 8.5% respectively. This indicates that the catalyst surface consisted mostly of metallic palladium.

In comparison to metallic $3d_{5/2}$ peak of the Pd/C, an increase in binding energy from 335.3 eV to 335.6 eV was observed for the PdIr/C catalyst. This 0.3 eV increase in palladium binding energy upon iridium addition suggests a possible interaction between both metals. Asanova *et al.* [175] reported a similar observation and attributed the increase in palladium binding energy to a charge transfer from palladium to iridium.
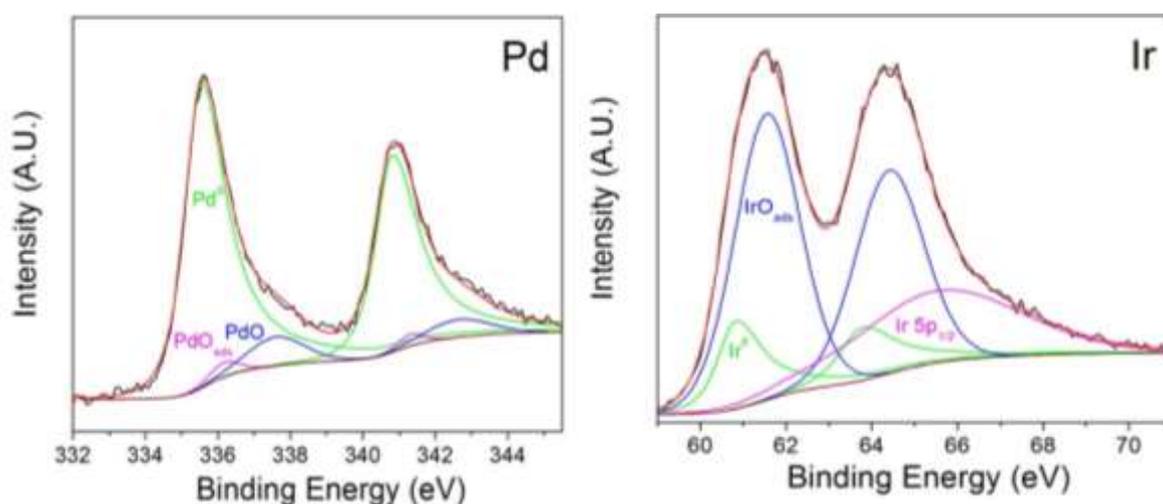
Figure 31: Pd 3d and Ir 4f XPS Spectra obtained for PdIr/C.

The Ir $4f$ spectrum (Figure 31) was resolved into two doublets and a singlet peak. The peak positions of the Ir $4f_{7/2}$ at 60.7 eV and 61.5 eV were assigned to metallic iridium [175] and iridium with oxygen adsorbed (IrO_{ads}) [177] respectively. The singlet peak at 65.5 eV was attributed to the Ir $5p_{1/2}$ peak as discussed by Kahk [178]. The corresponding Ir $5p_{3/2}$ peak was seen in the survey spectrum at a binding energy of approximately 49 eV as expected. A 0.2 eV decrease in binding energy of metallic Ir $4f_{7/2}$ was observed (60.9 eV to 60.7 eV). This negative shift corroborates the initially observed positive shift in the Pd $3d$ spectrum and confirms an alloying interaction between palladium and iridium in the PdIr/C catalyst as suggested by the XRD analysis.

The Pd 3*d* and Ir 4*f* XPS spectra obtained for the PdIrAu/C catalyst were similar in composition and binding energies to PdIr/C. This indicates that the surfaces of the ternary catalyst are similar to that of bimetallic PdIr/C and the addition of gold to the ternary catalyst did not cause a modification in palladium-iridium's surface behaviour.

4.6 Cyclic Voltammetry (CV) Characterisation of Palladium-Iridium Catalysts

The cyclic voltammograms obtained for Pd/C, PdIr/C and PdIrAu/C catalysts at a scan rate of 20 mVs-1 from 0.05 to 1.2V in nitrogen is shown in Figure 32.
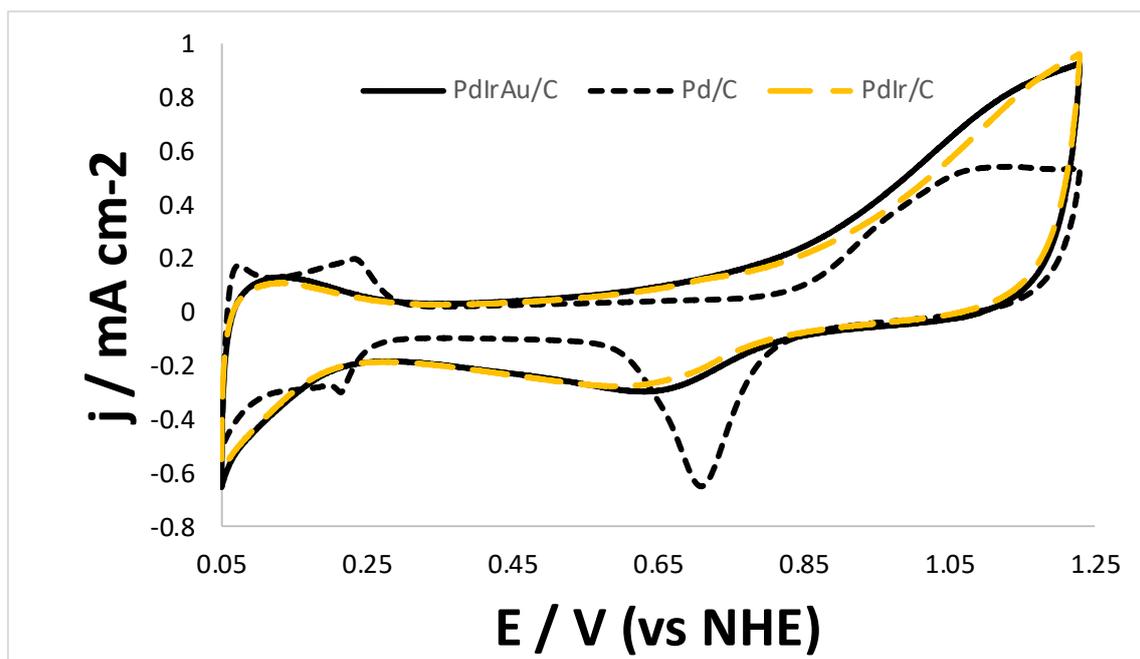
Figure 32: Cyclic voltammograms of Pd/C, PdIr/C and PdIrAu/C catalysts in N_2-saturated 0.5 M H_2SO_4 at a scan rate of 20 mVs^{-1}.

From Figure 32, it can be observed that PdIr/C and PdIrAu/C had similar CV profiles which were quite different to the typical shape seen for the Pd/C catalyst; indicating significant changes to the palladium CV upon the addition of iridium. Similar observations for the CV changes in palladium-iridium alloys have been reported in literature [169, 179]. The surface oxide formation on the iridium-containing catalysts started at a much lower potential (0.55 V) than on Pd/C (0.75 V). On the reverse scan, oxide reduction peak for PdIr/C and PdIrAu/C catalysts were observed to have shifted to a lower potential (0.61 V from 0.7 V). This was thought to be a result of iridium's low oxygen reduction activity, with typical values of 0.44 V reported for oxide reduction peak of iridium on carbon electrodes [166, 180].

From the CVs (Figure 32), it can be observed that the oxide reduction peaks for PdIr/C and PdIrAu/C are very broad and not well resolved. In contrast to palladium and platinum electrodes,

iridium has been reported to show no distinct oxide reduction feature in acid electrolytes [166]. This has been discussed to be due to the nature of iridium's adsorption of oxygen species in aqueous solution being different to platinum and palladium electrodes [180].

The electrochemical surface area was calculated for the catalysts by integrating the charge under the palladium-oxide reduction peak and comparing this with a charge density of 420 μCcm^{-2} reported for the reduction of a monolayer of PdO on palladium [133]. The ECSA values obtained were 7.6, 8.2 and 15.5 m^2g^{-1} for the PdIr/C, PdIrAu/C and Pd/C catalysts respectively. It was observed that ECSA value for PdIrAu/C was larger than PdIr/C; this could be a result of its smaller average particle size (4.8 nm for PdIrAu/C and 5.2 nm for PdIr/C).

4.7 Oxygen Reduction Activity Studies of Palladium-Iridium Catalysts

Activity of PdIr/C and PdIrAu/C were evaluated from data obtained from linear sweep voltammograms recorded from a potential 30 mV higher than onset potential to 0.2 V a t a scan rate of 5 mVs^{-1} in oxygen-saturated 0.5 M H_2SO_4.
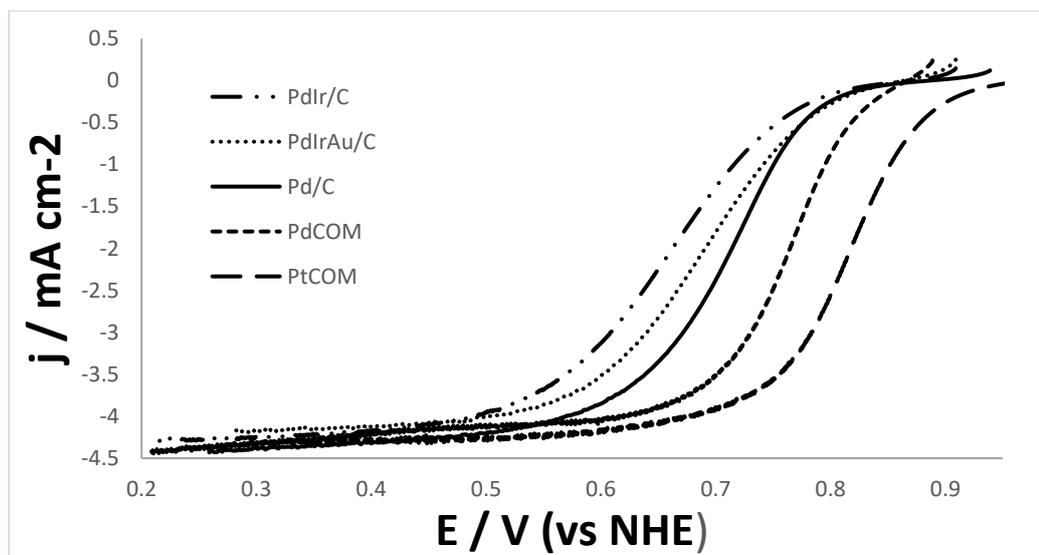
Figure 33: Linear sweep voltammograms for PdIr/C, PdIrAu/C compared with Pd/C, commercial Pd/C and commercial Pt/C at 900 rpm and a scan rate of 5 mVs^{-1}.

Figure 33 compares linear voltammograms recorded for the prepared PdIr/C, PdIrAu/C catalysts alongside prepared Pd/C, commercial 20 % Pd and 20 % Pt (PdCOM and PtCOM) at a rotation of 900 rpm. All catalysts displayed the three regions typically associated with an ORR polarisation curve. It can be seen that the commercial Pt/C had the highest activity followed by commercial Pd/C and the prepared Pd/C. PdIrAu/C had a higher activity than PdIr/C; suggesting that the addition of gold to the PdIr/C improved its activity. The increased activity of PdIrAu/C was thought to be as a result of its smaller average particle size.

Both PdIr/C and PdIrAu/C had activities lower than Pd/C; suggesting the addition of iridium caused a reduction in palladium's ORR activity. This is not surprising as iridium and gold have been reported to have low ORR activity in acid [118, 166]. Further electrochemical studies were carried out on these catalysts as the aim of this study was to investigate the stability of palladium-based catalysts. Onset potentials were 0.87, 0.87, 0.87 and 0.89 V for PdIr/C, PdIrAu/C, Pd/C and PdCOM catalysts respectively. The commercial platinum catalyst had an onset of 0.97 V which was about 100 mV more positive than that of any of the palladium-based catalysts.

4.8 Koutecky-Levich Analysis on Palladium-Iridium Catalysts

The data from the linear sweep voltammograms recorded for PdIr/C, PdIrAu/C and PtCOM at rotation rates of 400, 625, 900, 1225 and 1600 rpm were used for a Koutecky-Levich plot. The plots for PdIr/C and PdIrAu/C could only be compared with the commercial platinum catalyst as Koutecky-Levich plots could not be obtained for the prepared Pd/C and the commercial palladium catalyst due their instability as discussed in Chapter 3. Koutecky-Levich plot is a plot of the inverse overall current against the inverse of rotation rate. An extrapolation of rotation rate to infinity from the Koutecky-Levich plot gives the value of kinetic current. Kinetic current, i_k is the current without any effects from mass-transport. Figure 34 shows the plot obtained for the PdIr/C, PdIrAu/C and commercial Pt/C at a potential of 0.67 V. This potential was selected because all three catalysts were under a mixed kinetic and diffusion control regime at this potential.
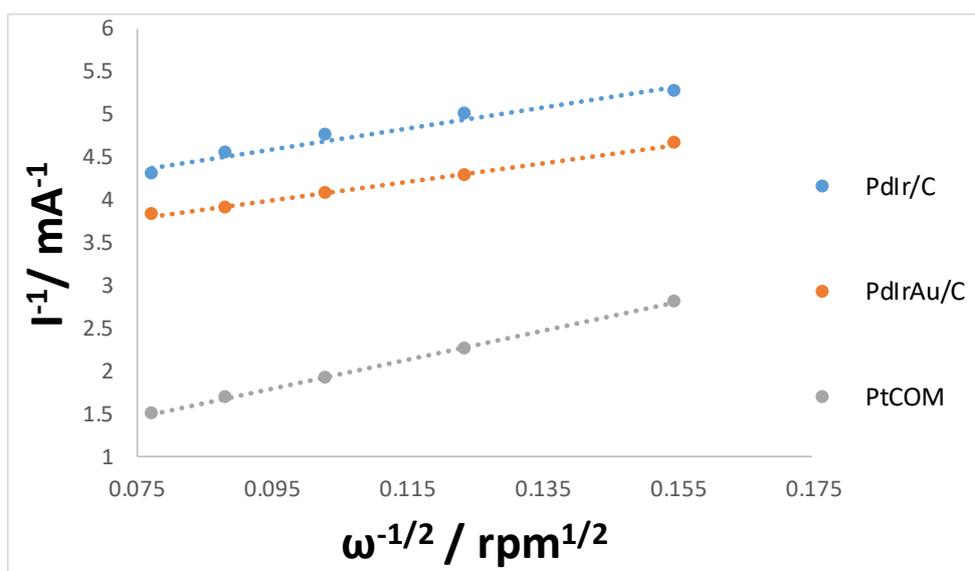
Figure 34: Koutecky-Levich plots obtained for PdIr/C, PdIrAu/C and the commercial Pt/C catalyst at 0.67 V.

Specific and mass activities were calculated from the kinetic current values obtained from each catalyst as shown in Table 10. The specific and mass activities were obtained for each catalyst by normalizing the kinetic current with its electrochemical surface area and its noble metal loading respectively.

Table 10: Kinetic parameters obtained for PdIr/C, PdIrAu/C and PtCOM catalysts.

Catalyst	Kinetic current at 0.67 V (mA)	Specific Activity at 0.67V (mAcm^{-2})	Mass Activity at 0.67 V (Ag$_{metal}^{-1}$)
PdIr/C	0.47	0.23	86.48
PdIrAu/C	0.55	0.29	111.75
PtCOM	5.92	2.41	1177.45

From the values obtained from the Koutecky-Levich plots in Table 10, it can be seen that the PdIrAu/C exhibited about one and half times the specific activity of the PdIr/C. This suggests that the addition of gold to PdIr/C improved its ORR activity. The observed enhancement could be resulting from PdIrAu/C's smaller average particle size; however, this improved activity of PdIrAu/C was about only a tenth of that of the commercial Pt/C. These values could not be compared with literature values as activities are usually reported at 0.9 V or 0.85 V for platinum catalysts.

4.9 Tafel Analysis on Palladium-Iridium Catalysts

Tafel analysis was used to evaluate the ORR activity of the PdIr/C and PdIrAu/C catalysts via the Tafel slope and the exchange current density. The obtained values were compared with those calculated for prepared Pd/C, commercial Pd/C and Pt/C. Figure 35 shows the Tafel plot obtained for the PdIr/C catalyst. The Tafel slopes and exchange current density values calculated for each catalyst are shown in Table 11.
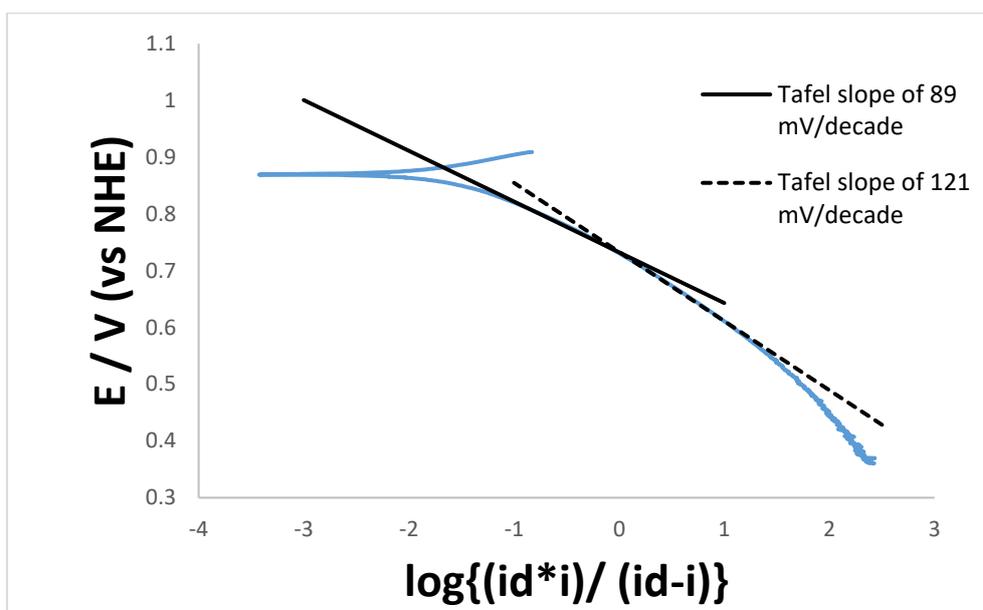
Figure 35: Tafel plot obtained for the PdIr/C catalyst showing its two Tafel slopes of 89 and 121 mVdecade^{-1} at the low and high current density regions respectively.

Table 11: Tafel Slopes and exchange current density values obtained for PdIr/C, PdIrAu/C Pd/C, commercial Pd/C and commercial Pt/C catalysts.

Catalyst	Tafel slope (mVdecade^{-1})	Exchange Current Density (Acm^{-2})
PdIr/C	89	2.8x10^{-13}
	122	5.1x10^{-11}
PdIrAu/C	92	5.6x10^{-13}
	120	9.3x10^{-11}
Pd/C	71	5.6x10^{-12}
PdCOM	59	9.5x10^{-12}
PtCOM	72	5.5x10^{-10}
	119	4.2x10^{-8}

In contrast to the palladium catalysts (Pd/C and PdCOM), PdIr/C and PdIrAu/C exhibited two Tafel slopes of 89 and 92 mVdecade^{-1} in the low current density region (0.82 to 0.73 V) as well

as 122 and 120 mVdecade^{-1} in the high current density region (from 0.72 V to lower potentials). The change in Tafel behaviour observed for PdIr/C and PdIrAu/C suggests that iridium caused a change in surface coverage of palladium by adsorbed oxygen intermediates. This modification in electronic behaviour of palladium is supported by the changes observed in oxide-formation and oxide-reduction regions of the CV for the palladium-iridium based catalysts. Therefore, the two Tafel slopes observed for PdIr/C and PdIrAu/C were attributed to an iridium modification of palladium surface. These Tafel values obtained are close to those reported in literature at 80 and 121 mVdecade^{-1} [165, 181] for iridium.

Although iridium's ORR has been reported [165] to proceed via a mechanism similar to platinum where platinum's Tafel slopes of 60 and 120 mVdecade^{-1} are characteristic for ORR at high surface oxygen coverage and low surface oxygen coverage respectively [12, 138], this difference in Tafel values at the low current density region (89 and 72 mVdecade^{-1} for PdIr/C and Pt/C respectively) suggests a difference in the rate determining step during ORR between platinum and iridium.

PdIr/C and PdIrAu/C showed exchange current densities lower than values obtained for Pd/C; indicating their lower ORR activity. The ternary catalyst showed higher exchange current densities than the PdIr/C. This improvement was attributed to the presence of gold in the catalysts. The obtained values are close to a value of (10^{-10} Acm^{-2}) published for ORR on an iridium catalyst at the high current density region with a Tafel slope of 112 mVdecade^{-1} [165].

4.10 Quantification of Hydrogen Peroxide Generated for Palladium-Iridium Catalysts

The ring currents obtained for PdIr/C and PdIrAu/C along with those obtained for Pd/C, commercial palladium and platinum catalysts at a rotation rate of 900 rpm are shown in Figure 36 below. All catalysts had a low ring currents with the lowest value obtained from the commercial Pt/C.

The percentage of peroxide produced during the ORR was quantified at 0.4 V. The percentage peroxide produced were 2.1 %, 2.6 %, 3.5 % 7.1 and 7.9 % for the commercial platinum, PdIr/C, PdIrAu/C, commercial Pd/C and prepared Pd/C catalysts respectively. The similar peroxide yields for commercial Pt/C and PdIr/C are consistent with literature reports of about 2 % reported for platinum and iridium catalysts [147, 182].
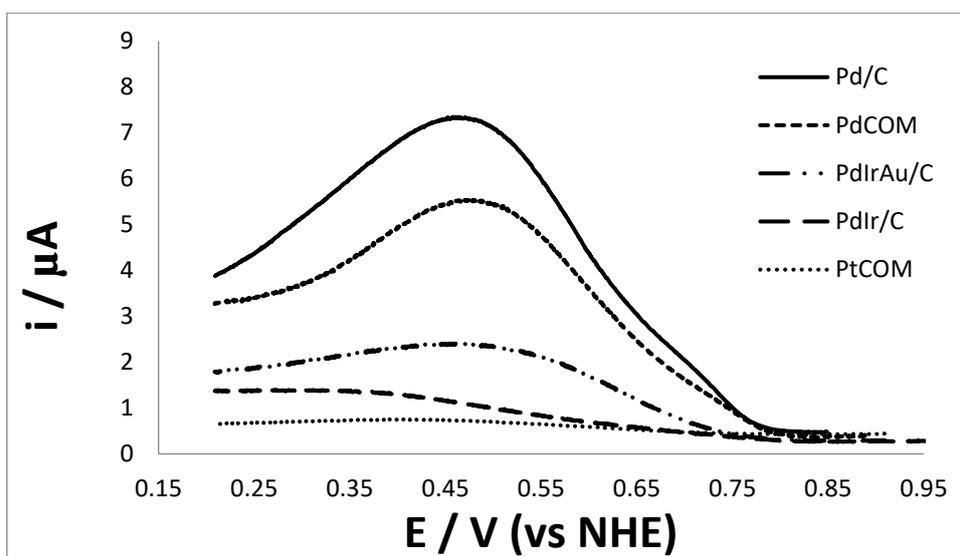
Figure 36: Ring currents obtained for PdIr/C, PdIrAu/C, Pd/C, commercial Pd/C and commercial Pt/C catalysts at 900 rpm and a scan rate of 5 mVs^{-1}.

The peroxide yield of PdIr/C and PdIrAu/C are similar, although the slightly higher yield on PdIrAu/C can be due to the presence of gold. In comparison to the prepared Pd/C and commercial Pd/C, PdIr/C and PdIrAu/C both had lower amounts of peroxide intermediates detected. This suggests that the interaction between palladium and iridium can improve palladium's selectively for the direct 4-electron reduction of oxygen.

4.11 Cyclic Voltammetry (CV) Stability Studies of Palladium-Iridium Catalysts

Cyclic voltammetry was used to study the stability of PdIr/C and PdIrAu/C catalysts in acid. This was done by recording 100 cyclic voltammograms for each catalyst at a scan rate of 100 mVs^{-1} from 0.05 to 1.2 V in nitrogen-saturated 0.5M H_2SO_4. The effect of cycling on the ECSA was monitored to provide information on catalyst stability. Figures 37 and 38 show the first, tenth, fiftieth and hundredth cyclic voltammograms obtained for PdIr/C and PdIrAu/C.

63
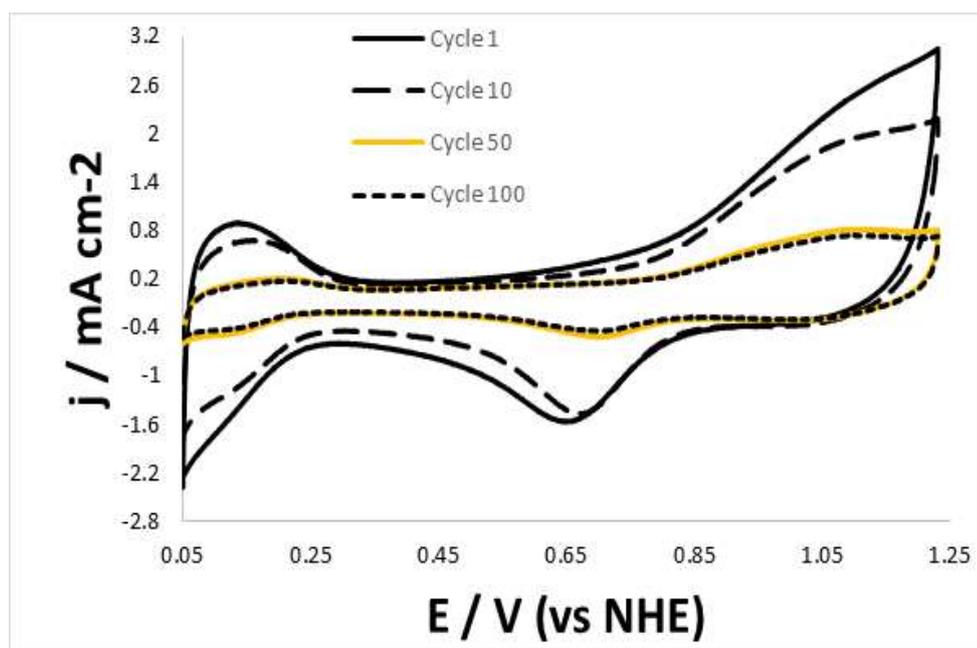
Figure 37: First, tenth, fiftieth and hundredth cyclic voltammograms obtained for PdIr/C catalyst during 100 cycles recorded at 100 mVs^{-1}.
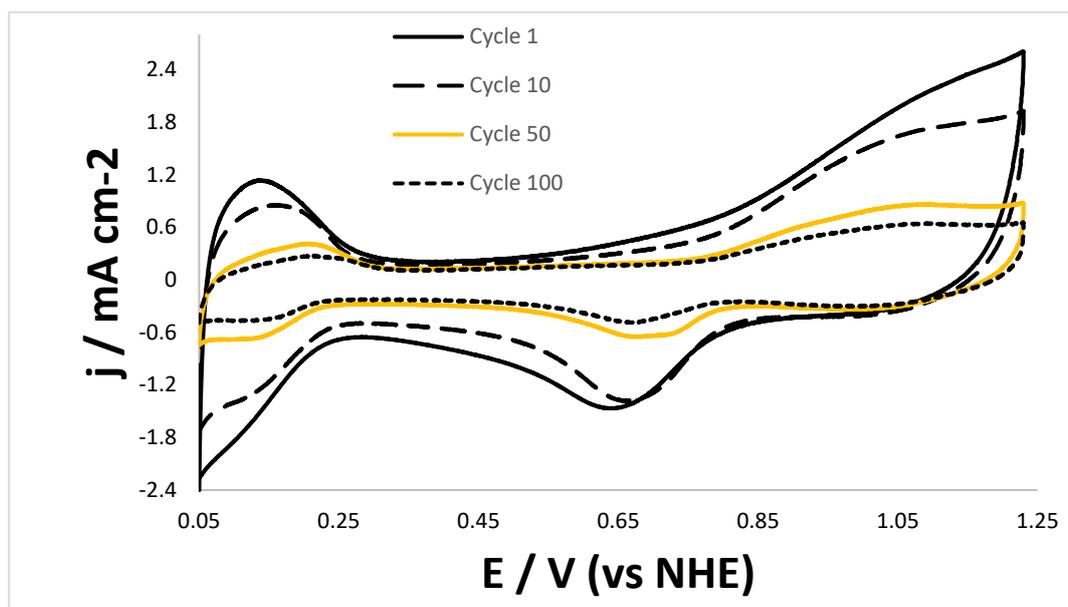
Figure 38: First, tenth, fiftieth and hundredth cyclic voltammograms obtained for PdIrAu/C catalyst during 100 cycles recorded at 100 mVs^{-1}.

From Figures 37 and 38, a dramatic change was observed in the overall shapes of the CVs recorded for the two catalysts over 100 cycles. Significant decreases were seen in the hydrogen adsorption and desorption area as well as in the oxide reduction areas over the 100 cycles recorded. The surface-oxide reduction peaks were observed to be shifted to higher potentials. These observations are similar with those observed and discussed for Pd/C and PdCOM in

Chapter 3. Therefore, the loss of ECSA for PdIr/C and PdIrAu/C was attributed to palladium oxidation and particle size increase. Table 12 shows the percentage of ECSA retained by each catalyst after the potential cycling along with for those values obtained for prepared Pd/C, commercial Pd/C, (PdCOM) and commercial Pt/C (PtCOM).

Table 12: ECSA values, average particle sizes and ECSA retained after cycling in nitrogen for PdIr/C, PdIrAu/C, Pd/C and commercial Pd/C and Pt/C catalysts.

Catalyst	Average Particle Size (nm)	ECSA (m^2g^{-1})	ECSA retained after 100 cycles (%)
PdIr/C	5.2	7.6	31
PdIrAu/C	4.5	8.2	38
Pd/C	5.4	15.5	22
PdCOM	3.6	25.8	9
PtCOM	3.1	57.2	98

In comparison to the Pd/C and PdCOM, it was observed that PdIr/C and PdIrAu/C retained higher percentages (31 % and 38 %) of their initial ECSA values respectively. This suggests the interaction of palladium with iridium in PdIr/C and PdIrAu/C improved palladium's stability under potential cycling conditions.

XPS analysis was done for PdIr/C, PdIrAu/C and PdCOM after degradation so as to investigate the electronic effect of potential cycling on the catalysts' surfaces. This was done by collecting the used catalysts' particles from the working electrode after the potential cycling test. The images shown in Figures 39, 40 and 41 are of the Pd 3*d* regions obtained for the catalysts (commercial Pd/C, PdIr/C and PdIrAu/C) before and after the catalysts' degradation. From the images, it can be observed that significant changes occurred on all the palladium surfaces during potential cycling; all 3 catalysts showed a decrease in the relative ratio of the metallic Pd^0 and an increase in the relative ratios of the oxidised species (PdO_{ads} and PdO) after the potential cycling.
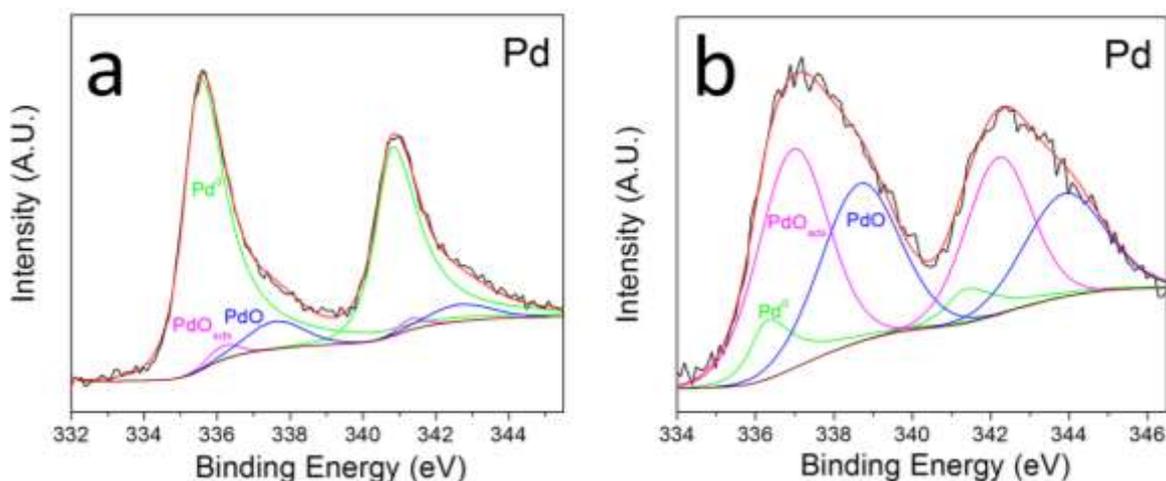
Figure 39: Pd 3d XPS Spectra obtained for commercial Pd/C before (labelled a) and after potential cycling (labelled b).

The fitted data of *Pd 3d* XPS spectra for the commercial Pd/C showed a significant reduction in the relative ratio metallic Pd^0 composition before and after the potential cycling study.
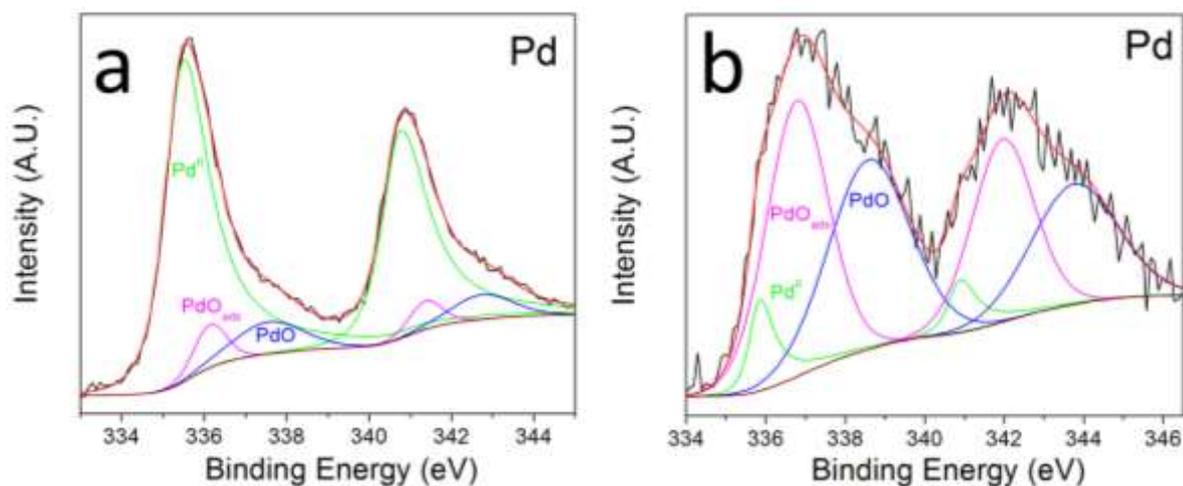
Figure 40: Pd 3d XPS Spectra obtained for PdIr/C before (labelled a) and after potential cycling (labelled b).

A similar decrease in intensity of the metallic Pd^0 peak was also observed for the PdIr/C. In comparison with PdCOM, the loss of the metallic Pd^0 composition was not as pronounced. This suggests that PdIr/C was more resistant to surface oxidation during the potential cycling.
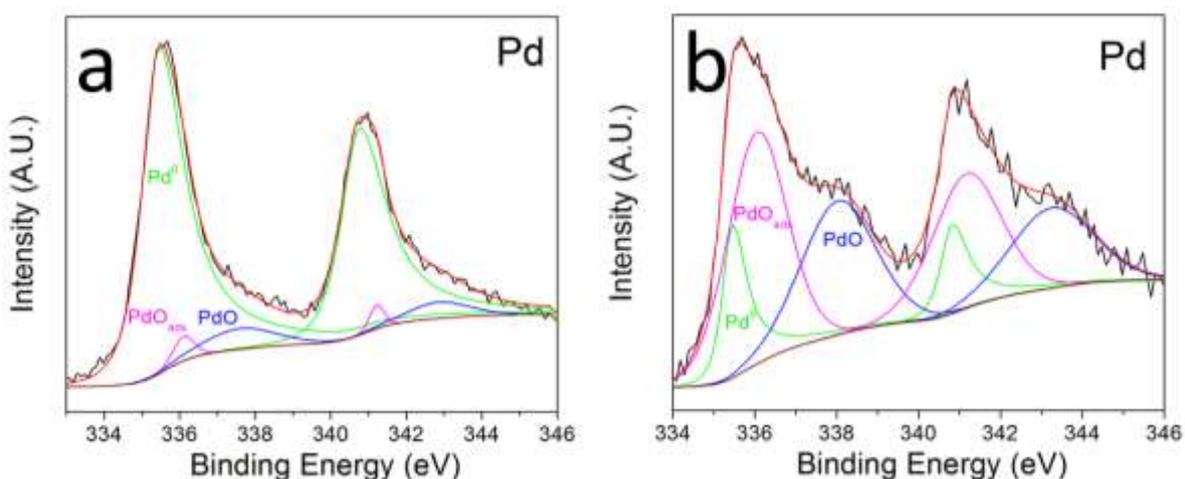
Figure 41: Pd 3d XPS Spectra obtained for PdIrAu/C before (labelled a) and after potential cycling (labelled b).

The increase in the surface oxidation detected by XPS could be a reason for their loss of activity during degradation as it has been reported that the zero-valent palladium and not the oxidised palladium is active for ORR [127]. This observation is in good agreement with the works of Arico *et al.* [183] who during an XPS study observed enhanced ORR activity as a result of increasing the relative ratio of metallic platinum in a catalyst. According to Solomun [74], the repetitive formation and reduction of palladium's surface oxide eventually leads to the suppression of palladium's electrodissolution and palladium becoming oxidised. Juodkazis *et al.* [75] also reported a similar observation of palladium's electrochemical oxidation rather than it's dissolution as being the main electrochemical process during palladium's anodic polarisation up to 1.3 V in 0.5 M H_2SO_4. They reported only about 5 % of the total amount of ionized palladium dissolved in the electrolyte. Therefore, the instability (loss of ECSA) observed for PdIr/C, PdIrAu/C and PdCOM in this potential cycling study was attributed to an electrochemical oxidation of palladium due to repeated potential cycling to high potentials.

Table 13 shows the percentage of metallic Pd^0 component retained by the catalysts after the potential cycling. A more stable catalyst would be more resistant to surface oxidation and hence be able to maintain a higher percentage of its initial metallic component. PdCOM was the most unstable catalyst as it retained only 12 % from the initial 92 % metallic Pd^0 component. PdIr/C and PdIrAu/C retained 20 % and 28 % respectively. This suggests that the electronic interaction between palladium and iridium as revealed by XRD and XPS analyses was able to modify palladium's properties and increase its resistance to oxidation. A similar electronic modification of palladium by iridium has been reported by Meku [184] for a stable Pd$_3$IrFe/C alloy; the authors concluded that this alloying interaction between palladium and iridium led to the

weakening of the adsorption of oxygenated intermediates on palladium surface. This can explain the higher stability observed for PdIr/C compared to commercial PdCOM as PdIr/C's palladium surface was more corrosion-resistant and retained higher percentage of its initial metallic component after the potential cycling.
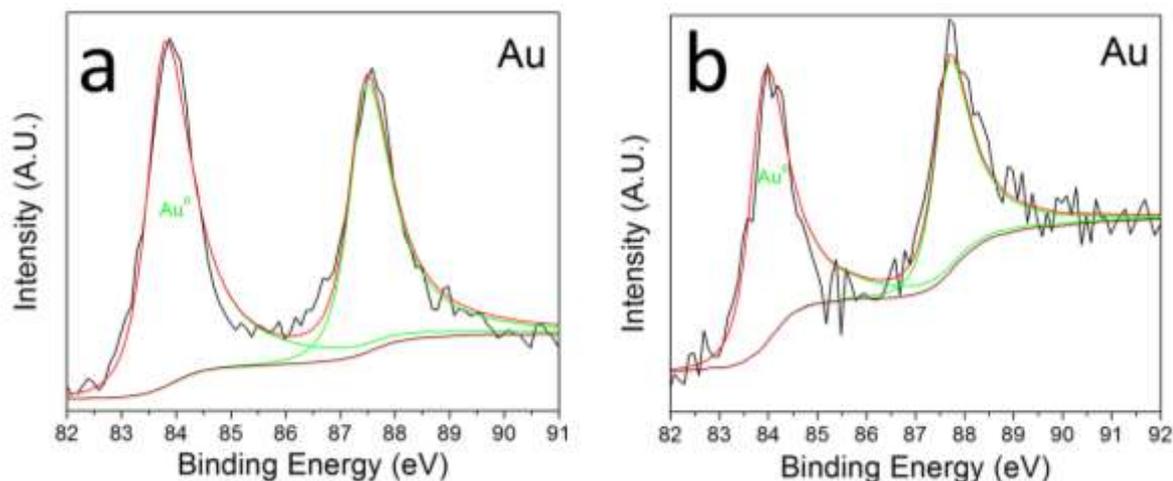
Figure 42: Au 4f XPS Spectra obtained for PdIrAu/C before (labelled a) and after potential cycling (labelled b).

Figure 42 shows the fitted data for the *Au 4f* spectra of PdIrAu/C before and after the potential cycling. It was observed that there were no discernible changes to the gold spectra before and after the experiment. This observation demonstrates the stability of gold and its resistance to oxidation under the potential cycling conditions used. XPS data could not obtained for the iridium *4f* spectra due to low intensity signals. Iridium's low intensity was thought to be due to Iridium's segregation to subsurface layers, as iridium has a higher surface segregation energy than palladium [185]. A similar enrichment of palladium on the surface has been reported for a Pd$_3$FeIr/C catalyst and the authors attributed this to a sub-surface segregation of iridium [184].

4.12 Chronoamperometry Studies of Palladium-Iridium Catalysts

The stability of PdIr/C and PdIrAu/C were evaluated using chronoamperometry. The holding potential was each catalyst's half-wave potential. Current was monitored over two hours at a rotation rate of 900 rpm. The obtained current-time plots are shown along with results obtained from Pd/C, commercial palladium and platinum catalysts in Figure 43. The plots show a normalized current, where 100% is the initial current at 10 seconds for each catalyst.
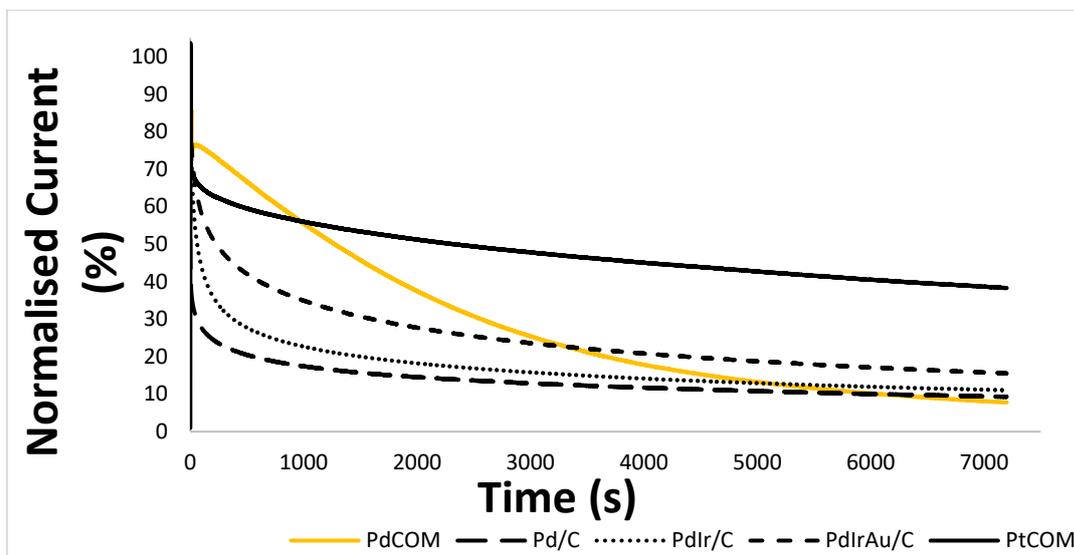
Figure 43: Chronoamperometric response curves obtained PdIr/C, PdIrAu/C, Pd/C, commercial Pd/C and Pt/C catalysts normalised to each catalyst's initial current.

From Figure 43, a steady decay of current was observed for all catalysts. Percentages of ORR current retained were 18 %, 25 %, 16 %, 13 % and 63 % for PdIr/C, PdIrAu/C, Pd/C, PdCOM and PtCOM catalysts respectively. The commercial platinum, followed by the PdIrAu/C exhibited the highest stability. This is in good agreement with the trend observed in the potential cycling test monitoring the ECSA loss during the cycling.

4.13 ORR Degradation Studies on Palladium-Iridium Catalysts

A degradation test was done to evaluate catalysts' stabilities and quantify the loss of activity during ORR for PdIr/C, PdCOM and PtCOM. The degradation was done through potential cycling between 0.87 V to 0.4 V. These potentials were selected for use in order to exclude electrochemical processes involving hydrogen or palladium oxidation since palladium has been reported to undergo oxidation at potentials around 0.96 V [73, 156]. In addition, the initial stability tests of potential cycling between 0.05 and 1.2 V (Section 4.11) suggested palladium oxidation as a potential cause of catalyst degradation.

At the start of the experiment, 3 cyclic voltammograms were recorded in a nitrogen-saturated 0.5 M H_2SO_4 from 0.05 to 1.2 V at a scan rate of 20 mVs^{-1} to determine the ECSA of the catalyst. After the CVs were recorded, the catalysts were subjected to 1000 runs of potential cycling between 0.87 and 0.4 V at a scan rate of 0.2 Vs^{-1} in an oxygen-saturated 0.5 M H_2SO_4 with no electrode rotation and the maintenance of oxygen flow to the electrolyte. After the thousandth cycle, 3 CVs were recorded in nitrogen under similar conditions to those at the start of the experiment. The results were evaluated by comparing ECSA values obtained before and after

the potential cycling. Figure 44 shows the initial and final CVs obtained for PdIr/C along with those from the commercial palladium and platinum catalysts (Figures 45 and 46).
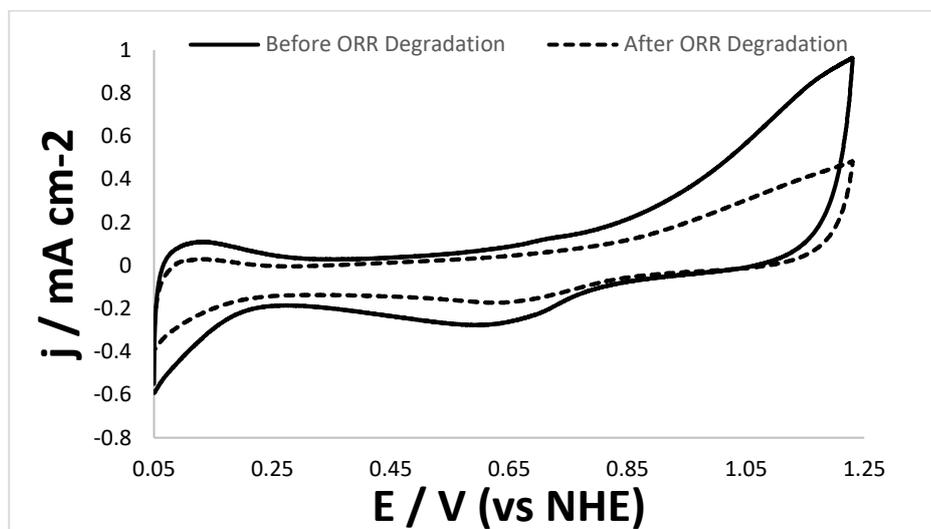
Figure 44: Cyclic voltammograms obtained for the PdIr/C catalyst before and after ORR degradation recorded at 20 mVs^{-1} in N$_2$-saturated H$_2$SO$_4$.

For PdIr/C, the CV recorded after the potential cycling shows a decreased of the peaks related to hydrogen adsorption and desorption as well as surface oxide formation and surface oxide-reduction. This observation is indicative of a reduction in the electrochemical surface area. In literature, loss of ECSA has been attributed to an increase in particle size resulting from agglomeration [62, 153, 186]. The ECSA of PdIr/C after degradation was found to be 52 % of its initial value. This is a milder degradation in comparison to the stability test of potential cycling from 0.05 to 1.2 V where the same catalyst could retain only 31 %.
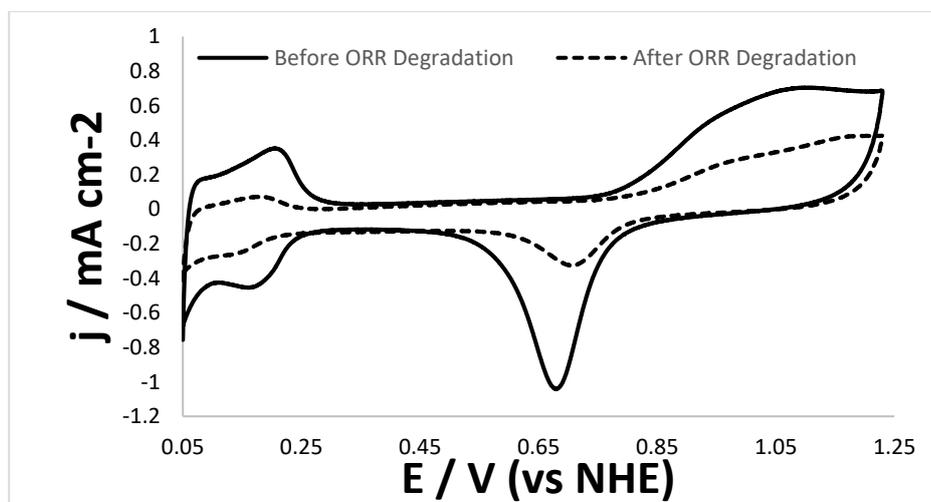
Figure 45: Cyclic voltammograms obtained for the commercial Pd/C catalyst before and after ORR degradation recorded at 20 mVs^{-1} in N$_2$-saturated H$_2$SO$_4$.

In comparison to PdIr/C, the commercial palladium catalyst showed a similar decrease in the hydrogen adsorption and desorption as well as palladium-oxide formation and reduction peaks. In addition to this, a shift to a higher potential value for the oxide-reduction peak; usually associated with particle size increase was observed. The ECSA obtained from the CV after degradation was 18 % of its initial value; indicating an increase in particle size for palladium during cycling.
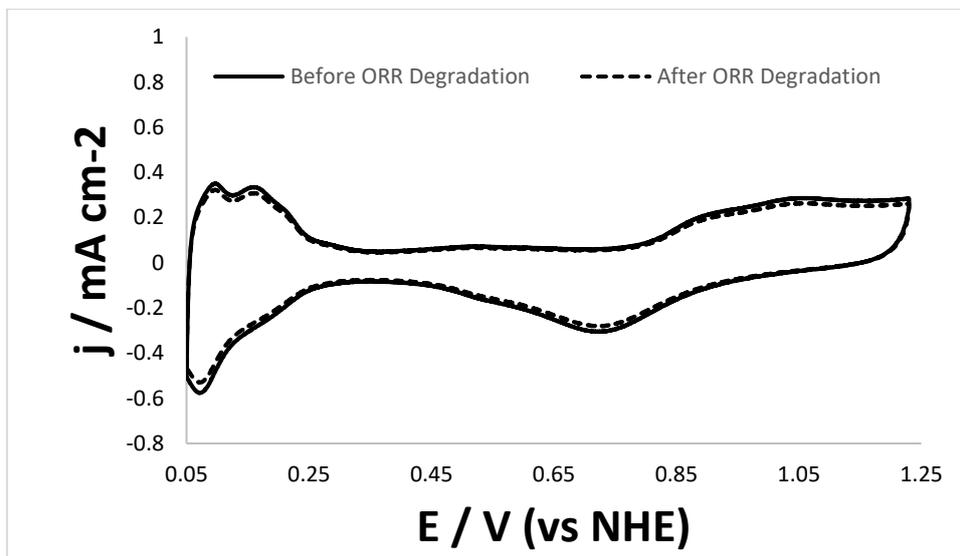
Figure 46: Cyclic voltammograms obtained for the commercial Pt/C catalyst before and after ORR degradation recorded at 20 mVs^{-1} in N$_2$-saturated H$_2$SO$_4$.

In contrast to PdIr/C and PdCOM, the commercial platinum catalyst retained 99 % of its initial ECSA after the ORR degradation test. Therefore, it was concluded that no significant changes to platinum's particle size occurred during the potential cycling.

TEM analysis was done for PdIr/C, PdCOM and PtCOM after the ORR degradation so as to investigate the effect of repeated ORR cycles on the morphology of the catalysts. This was done by collecting the catalysts' particles from the working electrode after the electrochemical ORR degradation experiment was completed. The representative micrographs shown below in Figures 47 and 48 compares the initial morphology of the catalysts as prepared and received with their final morphology after the ORR degradation test. It was observed that all three catalysts initially had good dispersion of nanoparticles on the carbon support without much agglomeration.

Table 13: Percentages of ECSA retained after nitrogen potential cycling, metallic Pd^0 retained, chronoamperometric current retained and ECSA retained after ORR degradation in oxygen obtained for PdIr/C, PdIrAu/C, Pd/C, commercial Pd/C and Pt/C catalysts.

Catalyst	% of ECSA retained after potential cycling (0.05 to 1.2 V in N_2)	% XPS' Pd^0 retained after potential cycling	% of current retained from chronoamperometry	% of ECSA retained after degradation (0.87 to 0.4 V in O_2)
PdIr/C	31	20	18	56
PdIrAu/C	38	28	25	-
Pd/C	22	-	16	-
PdCOM	9	12	13	18
PtCOM	98	-	63	99
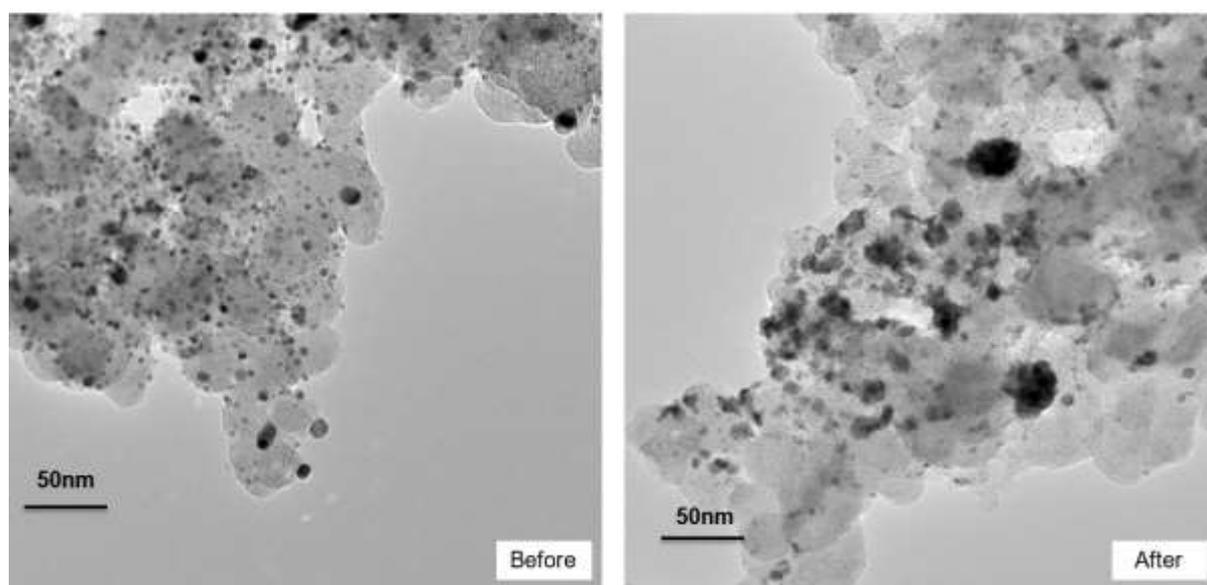
Figure 47: TEM image obtained for PdIr/C before and after the ORR degradation in oxygen.

The TEM image obtained for PdIr/C after the ORR degradation revealed an overall lower particle density on the carbon support. It was also observed that after the test, there were fewer individual nanoparticles as well as a higher number of larger-sized and agglomerated particles

on the support. This was thought to be due to particles near one another coalescing and increasing in size during ORR degradation.
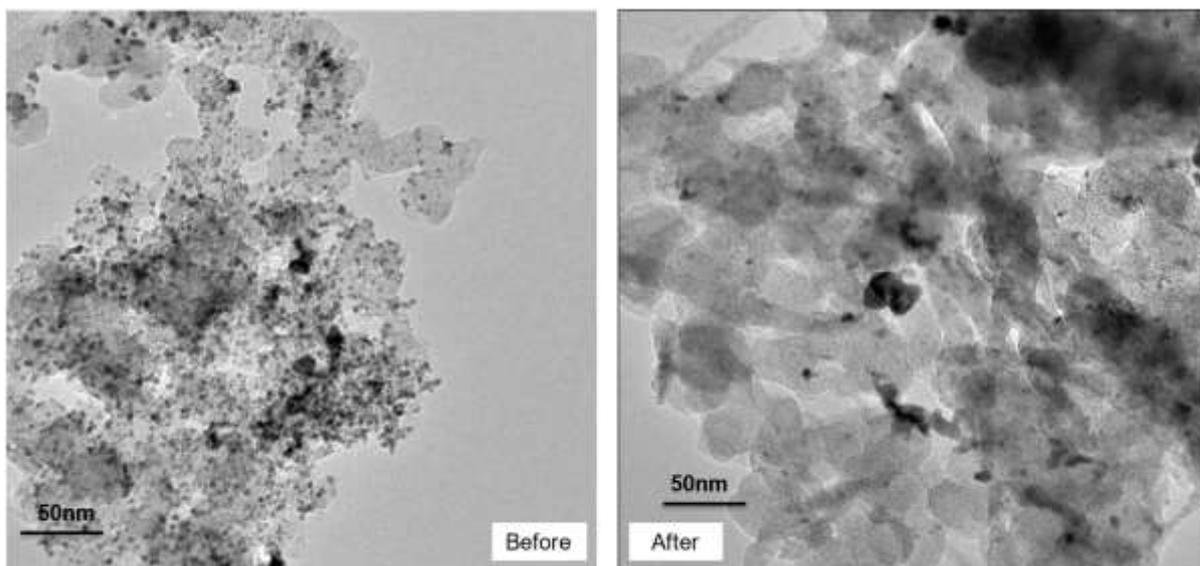
Figure 48: TEM image obtained for commercial Pd/C before and after the ORR degradation in oxygen.

For the commercial Pd/C, fewer individual nanoparticles as well as larger agglomerates and areas with depleted number of particles were observed. Detachment of particles from the support can result from a weaker interaction between the particles and support. A comparison between the micrographs obtained for PdIr/C and commercial Pd/C suggests a more extensive change in morphology to the commercial palladium catalyst. This corroborates the observed ECSA retention of 18 % and 56 % for PdCOM and PdIr/C respectively. The higher stability of PdIr/C is indicative of a stronger interaction between the palladium-iridium particles with the carbon support compared to the interaction between palladium particles and the carbon support. The interaction of palladium and iridium has been reported to improve dispersion on carbon as a result of Pd-Ir bonds lowering the surface energy of the metal particles and hence preventing their aggregation [184].

In contrast to the commercial Pt/C, PdIr/C and commercial Pd/C showed significant changes in the catalysts' morphology after the degradation experiment. This indicates the platinum catalyst was more resistant to surface modification than the palladium-based ones. There was no measurable change in morphology and particle sizes in the platinum catalyst after the 1000 cycles. This is unsurprising as measurable platinum degradation is usually observed when cycling at potentials higher than the 0.87 V upper limit used for this study [187, 188].
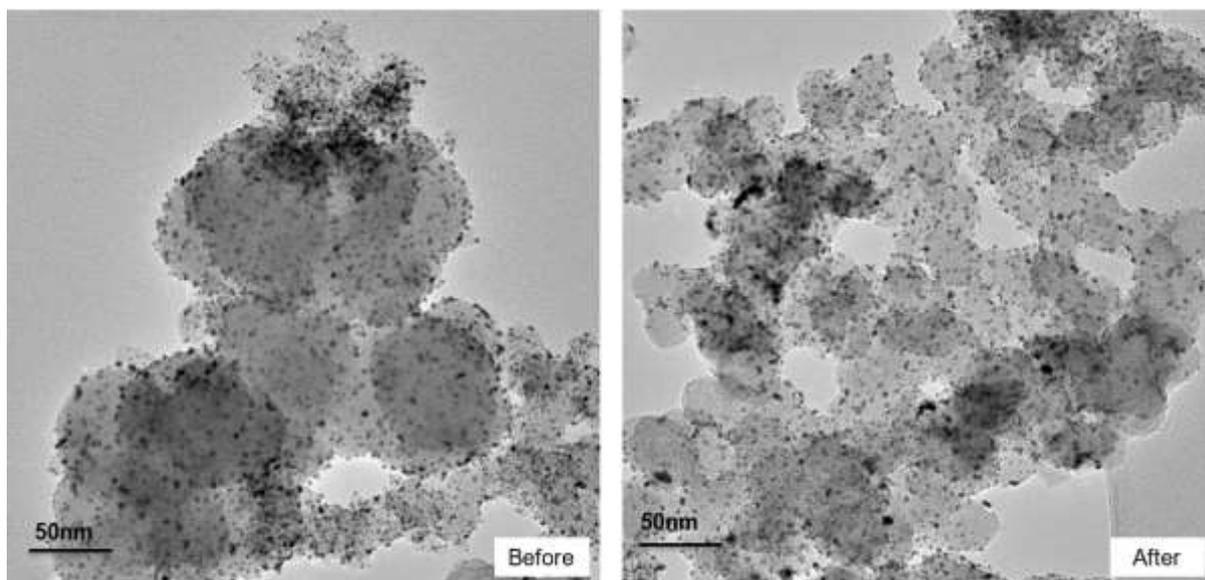
Figure 49: TEM image obtained for commercial Pt/C before and after the ORR degradation in oxygen.

From the micrographs, the loss of ECSA and activity for commercial Pd/C and PdIr/C was qualitatively attributed to particle detachment and subsequent agglomeration. However, this analysis is limited as it is only representative and does not take into account other degradation mechanisms operating on the catalysts. A more thorough technique such as identical location transmission electron microscopy would be able to monitor identical areas on a micrograph before and after the experiment so as to elucidate the exact degradation mechanism of the catalysts [188].

4.14 Conclusions

Carbon-supported palladium-iridium and palladium-iridium-gold catalysts were successfully synthesised by a polyol method in ethylene glycol. The average particle sizes were 5.2 and 4.8 nm for PdIr/C and PdIrAu/C catalysts respectively. XRD and XPS analyses revealed an alloying interaction between palladium and iridium. Electrochemical characterisation showed similar CV profiles for PdIr/C and PdIrAu/C. These CVs revealed significant changes to the palladium CV upon alloying with iridium. The surface oxide formation on the iridium-containing catalysts started at a much lower potential (0.55 V) than on Pd/C (0.75 V). On the reverse scan, oxide reduction peak for PdIr/C and PdIrAu/C catalysts shifted to a lower potential (0.61 V from 0.7 V). The electrochemical surface areas obtained were 7.6, 8.2 and 15.5 m^2g^{-1} for the PdIr/C, PdIrAu/C and Pd/C catalysts respectively.

Linear sweep voltammograms showed onset potentials of 0.87, 0.87, 0.87 and 0.89 V for PdIr/C, PdIrAu/C, prepared Pd/C and commercial Pd/C catalysts respectively. Koutecky-

Levich analysis was used to calculate kinetic current and hence specific and mass activities of the catalysts. Specific activities obtained at 0.67 V were 0.23, 0.29 and 2.41 mAcm^{-2} for PdIr/C, PdIrAu/C and commercial Pt/C respectively. In comparison to PdIr/C, the enhanced activity of PdIrAu/C was attributed to its smaller average particle sizes. Tafel analyses showed that PdIr/C and PdIrAu/C exhibited slope values around 90 and 120 mVdecade^{-1} in the low and high current density regions respectively. This Tafel behaviour was different to that observed on the Pd/C catalysts; suggesting iridium alloying modified palladium's electronic behaviour and its adsorption interaction with oxygen intermediates. Exchange current densities calculated were in the order of order of 10^{-13}; about one order in magnitude lower than values obtained for Pd/C catalysts (10^{-12}) at the lower Tafel slope. The peroxide yield for the palladium-iridium catalysts were similar to platinum's and about half the amount for detected for Pd/C catalysts.

Potential cycling from 0.05 to 1.2 V over 100 cycles revealed significant ECSA loss of 69 and 61 % for PdIr/C and PdIrAu/C respectively. These results demonstrate the relatively higher stability of the palladium-iridium catalysts in comparison to prepared and commercial Pd/C that lost 78 and 91 % of their initial ECSA values respectively when subjected to the same potential cycling tests. XPS analysis done on catalysts after the potential cycling test revealed increased relative amounts of oxidised surface palladium species. PdIr/C and PdIrAu/C were observed to have retained higher percentages of metallic Pd^0 (20 and 28 % respectively) than the commercial Pd/C catalyst (12 %). This suggested that the electronic interaction between palladium and iridium was able to modify palladium's properties and increase its resistance to surface oxidation.

Similar trends in stability data of the catalysts were obtained when catalysts were subjected to chronoamperometry. PdIr/C and commercial Pd/C were found to have retained a higher percentage of their initial ECSA (56 and 18 % respectively) after the milder ORR degradation test of 1000 runs of potential cycling between 0.87 and 0.4 V. This indicates that catalysts' exposure to high anodic potentials was a more significant factor in ECSA loss than the number of cycles recorded. TEM analysis done after the mild ORR degradation revealed agglomeration and particle size increase as the cause of ECSA loss. In comparison to the commercial Pd/C, the extent of agglomeration and particle size increase was lower for PdIr/C; corroborating the lower loss of ECSA observed for it.

From these results, the alloying of iridium with palladium was found to beneficial to improving palladium's stability in acid media due to a modification in palladium's interaction with

oxygenated species. However, a reduction in activity was also observed; indicating further research is needed into increasing the activity of the palladium-iridium alloys.

Chapter 5. TiO$_2$-C and WO$_3$-C Supported Palladium-Iridium Particles as Oxygen Reduction Catalysts

5.1 Introduction

Although carbon blacks are the most commonly used support material for oxygen reduction catalysts, they suffer from electrochemical corrosion at potentials above 0.9 V [189]. Corrosion of the support results in detachment and agglomeration of the detached metal nanoparticles; leading to a loss of electrochemical surface area and an overall degradation in activity. Therefore, transition metal oxides especially titanium oxides and tungsten oxides with their abundant availability, low prices, high stability and corrosion-resistance have been explored as possible alternatives to carbon black supports [190-194].

Titanium and tungsten in TiO$_2$ and WO$_3$ are present in their highest oxidation states of +4 and +6 respectively and so do not readily lose additional electrons to become further oxidised. In comparison to a carbon-based support, TiO$_2$ and WO$_3$ supports have been reported to have stronger interactions with the metal particles [194, 195]. This is interaction is called strong metal-metal oxide interaction (SMSI) in the literature. SMSI has been associated with prevention of metal particle agglomeration as well as modification of the metal's electronic properties resulting in enhancement of activity and stability [196, 197].

Huang *et al.* reported similar activity and enhanced stability for a platinum catalyst supported on carbon-doped TiO$_2$, in comparison to platinum supported on carbon [198] in acidic media. They also reported a similar observation for a platinum-palladium supported on carbon-doped TiO$_2$ catalyst [199]. The authors attributed the enhanced stabilities to the presence of TiO$_2$ in the support minimizing carbon corrosion and loss of electrochemical surface area in the catalysts.

In contrast to a prepared sample of Pt/C, dealloyed platinum-copper supported on TiO$_2$ have been reported to have a significant increase in ORR activity as well exceptional stability. The authors observed a current density of 4.0 and 2.0 mAcm^{-2} on dealloyed PtCu/TiO$_2$ and Pt/C at 0.9 V respectively. They also observed an absence of noticeable particle size increase with potential cycling. Strong electronic interactions between the dealloyed platinum-copper and the TiO$_2$ support was discussed as the reason for the enhancement in activity and stability [89].

XPS studies of platinum electrochemically deposited on TiO$_2$ revealed that the support had a strong interaction with the electronic structure of the platinum and this modification influenced the observed ORR activity [200]. Estudillo-Wong *et al.* [192] reported palladium supported on

TiO$_2$/C hybrid materials as displaying enhanced activities for methanol oxidation in comparison to conventional Pd/C This enhancement was attributed to a strong metal-metal oxide interaction between palladium and TiO$_2$. This interaction was deduced from a decrease in lattice parameter from the XRD analysis.

Fu *et al.* [201] reported enhanced ORR activity for platinum and palladium deposited on hybrid TiO$_2$ nanotubes on titanium support, compared to similar nanoparticles supported on carbon. The authors attributed the activity enhancement to strong interactions between the metal nanoparticles and the TiO$_2$ leading to a favourable change in adsorption energy of intermediate oxygen species during the oxygen reduction reaction. It is of interest to note that the ORR enhancement was greater for the Pd/TiO$_2$/Ti than the Pt/TiO$_2$/Ti; suggesting that the strong metal-metal oxide interaction between palladium and TiO$_2$ is more favourable for ORR than that of platinum and TiO$_2$. Although the authors observed an activity enhancement for the platinum and palladium supported on TiO$_2$/Ti compared similarly-prepared particles supported on carbon; their activities were much lower than those of the commercial Pd/C and Pt/C. Stabilities of these catalysts were not discussed.

Similarly, tungsten is a metal with some potential uses fuel cells. Tungsten-based materials have been reported and tested as catalysts as well as supports in fuel cell studies. For instance; Goddard *et al.* calculated and found that Pd$_3$W could be a good catalyst for ORR as it had a desirable d-band centre[202]. Bard *et al.* [203] reported that a palladium-tungsten catalyst (30% W) showed a ten-fold increase in activity in order of 10^{-3} Acm^{-2} compared to a palladium catalyst (10^{-4} A cm^{-2}) at 0.85 V. This catalyst also exhibited good stability when held at a voltage of 0.55 V for 3 days in 0.5 M H$_2$SO$_4$.

Palladium supported on a tungsten-based bimetallic carbide (Co$_3$W$_3$C) was reported to demonstrate good activity was well as stability in acidic environment [204]. Although a lower onset than platinum was obtained for this catalyst, its half-wave potential was 20 mV and 90 mV higher than Pt/C's and Pd/C's respectively. The improved activity was attributed to a synergetic effect of the support donating electron density to palladium. The stability of the catalyst was investigated by cycling between 0.6 and 1.2 V in oxygen for 1000 cycles. The catalyst retained 93 % of its activity while Pt/C retained 82 %. The stability of the catalyst was attributed to the support's improved stability over carbon.

Yan *et al.* [197] observed an improvement in ORR mass activity (174.6 mAmg^{-1}) of platinum supported on carbon-tungsten oxide composite compared to Pt/C (98.6 mAmg^{-1}) at 0.9 V in acid. The carbon-tungsten oxide-supported catalyst also had higher stability; these

improvements were attributed to a strong interaction between platinum and WO_3 modifying the electronic properties of platinum.

Palladium supported on WO_3-C hybrid materials has been reported to have high ORR activity comparable to commercial Pt/C [194] in acid. A shift relative in the Pd $3d$ binding energy was observed in the XPS of the Pd $3d$ of the Pd/WO_3-C compared to Pd/C; leading to the conclusion of a 'strong metal-metal oxide' interaction between the palladium and the WO_3-C support. The authors attributed the improved activity to small particles, uniform dispersion as well as a strong interaction between palladium and WO_3 leading to formation of tungsten bronze; enhancing ORR. The catalysts' stabilities were not evaluated.

The literature suggests the addition of titanium and tungsten-based materials could be beneficial to improving catalysts' ORR activities and stabilities. The most stable oxides (TiO_2 and WO_3) were chosen for use in this study as supports. Although they are both semi-conductors [205, 206] with lower conductivity than carbon blacks, the addition of Vulcan increases overall conductivity of the supports.

5.2 Preparation of the Titanium and Tungsten Oxide-Carbon Composites.

Titanium t-butoxide was added to 750 mg of Vulcan powder. 10 ml of hydrogen peroxide was added slowly, and the mixture was kept at room temperature until it dried.

Phosphotungstic acid solution was added to 750 mg of Vulcan powder. This mixture was stirred for 48 hours at room temperature. The suspension was centrifuged to remove excess phosphotungstic acid. The obtained powder was dried in the oven overnight.

Both samples were heat-treated at 600°C under nitrogen to obtain the titanium oxide-carbon and tungsten oxide-carbon composites. The obtained composites were then used as catalyst support for palladium-iridium nanoparticles.

5.2.1 Synthesis of Palladium-Iridium Nanoparticles on Titanium and Tungsten Oxide-Carbon Composites

To prepare each catalyst, appropriate amounts of $(NH_4)_2PdCl_4$ and $IrCl_3.3H_2O$ were dissolved in 10 mL sodium citrate solution to obtain a 1:1 palladium: iridium composition. This mixture was added dropwise to a heated flask containing a nitrogen-saturated sonicated suspension of 200 mg composite support (TiO_2-C or WO_3-C) in 75 mL ethylene glycol at 140 °C. The reaction was maintained at this temperature for 3 hours. The solution was allowed to cool down naturally and each catalyst was separated from the reaction solution by centrifuging. Catalyst was

extensively washed with deionised water and ethanol. Catalyst was dried at 80 °C in the oven overnight and ground with a mortar. Catalysts were denoted PdIr/TiO$_2$-C and PdIr/WO$_3$-C based on the support used.

Palladium-iridium catalyst (PdIr/C) prepared and discussed in previous chapter (Chapter 4) will be used for comparison purposes.

5.3 X-ray Diffraction (XRD) Analysis of Palladium-Iridium Catalysts Supported on TiO$_2$-C and WO$_3$-C

The X-ray diffraction patterns of the palladium-iridium nanoparticles supported on TiO$_2$-C, WO$_3$-C and Vulcan are shown in Figure 50. The broad peak at 25° was assigned to carbon for all catalysts. In the case of the PdIr/TiO$_2$-C, a TiO$_2$ reflection overlaps with it making it appear sharper.

All three catalysts showed diffraction peaks at 2θ values of ca. 40.1°, 46.5°, 68.2° and 81.9° corresponding to the (111), (200), (220), and (311) crystal planes of palladium respectively. Although no peaks relating to iridium or iridium oxide were observed, slight shift towards higher 2θ angles was noted for all catalysts as discussed for PdIr/C in Chapter 4. In comparison to PdIr/C, the Pd diffraction peaks on PdIr/TiO$_2$-C and PdIr/WO$_3$-C were at higher Bragg angles. This observation suggests an interaction between palladium and the oxides. A similar observation has been reported and attributed to an electronic interaction between palladium and TiO$_2$ [195, 207] and between palladium and WO$_3$ [194, 208].

For PdIr/TiO$_2$-C, additional peaks were seen at 25.3°, 27.4° 54.5°and 70.1°. These peaks corresponded to the anatase form of TiO$_2$. Also, the Scherrer equation could not be used for estimation of crystallite size due to peak overlap between TiO$_2$ and Pd at 68°.

For PdIr/WO$_3$-C, additional peaks were seen at 23.6°, 33.5°, 48.1°, 54.2°, 59.9° and 75.4° corresponding to the (200), (220), (400), (024), (422) and (442) crystal planes of H$_{0.53}$WO$_3$; hydrogen tungsten oxide [209]. The average crystallite size was estimated from the full-width at half maximum of the (220) peak using the Scherrer equation. The calculated size was 3.8 nm.
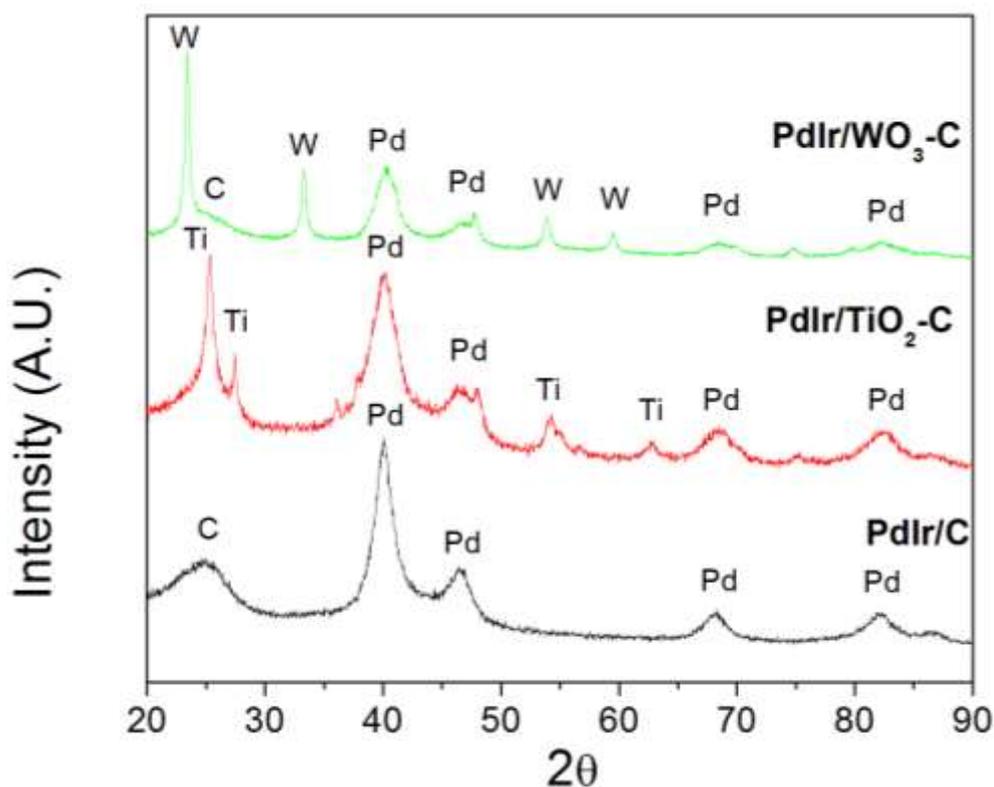
Figure 50: X-ray diffraction patterns obtained for PdIr/TiO₂-C, PdIr/WO₃-C and PdIr/C catalysts. Reflections labelled 'c, 'Ti' and 'W' correspond to carbon, titanium oxide and tungsten oxide respectively.

5.4 TEM and EDX Characterisation of Palladium-Iridium Catalysts Supported on TiO₂-C and WO₃-C

The obtained images for PdIr/TiO₂-C and PdIr/WO₃-C are shown in Figures 51, 52 and 53. For PdIr/TiO₂-C spherical metal particles were uniformly distributed on the support without much agglomeration.

A high-resolution image of single nanoparticles on PdIr/TiO₂-C is shown below in Figure 52. The image shows a palladium particle closely associated with a TiO₂ particle; further supporting the XRD data suggesting interaction between the metal particles and the TiO₂. Fast Fourier transform was used to measure the lattice space. The larger particle had a lattice spacing of 0.35 nm corresponding to anatase TiO₂ [210] and the smaller particle was identified as palladium.
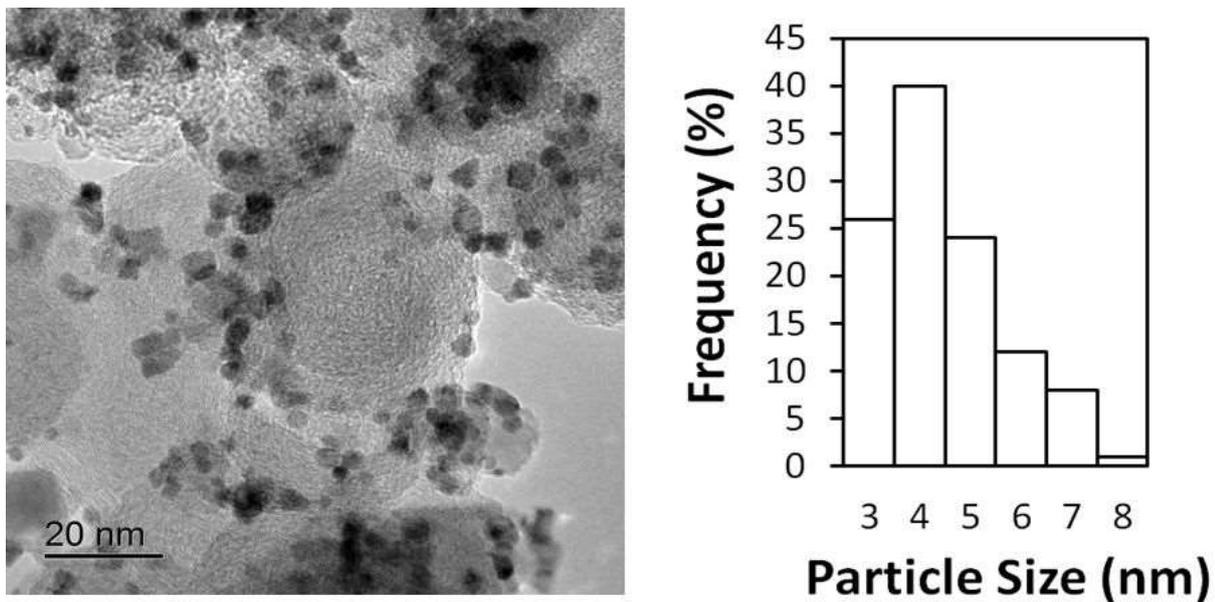
Figure 51: TEM image for PdIr/TiO₂-C and its corresponding particle size distribution.
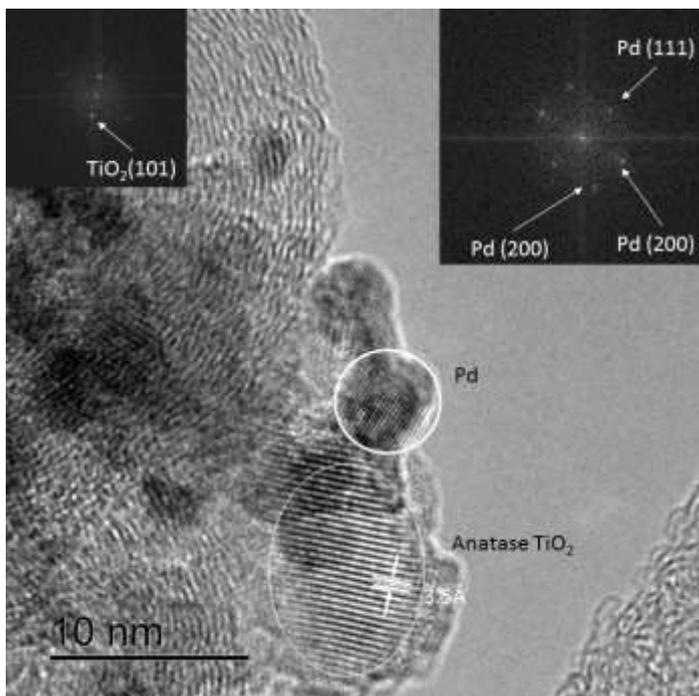
Figure 52: High resolution image obtained for PdIr/TiO₂-C showing lattice planes and the close interaction between palladium and TiO₂.

The obtained images for PdIr/WO₃-C showed many small spherical metal particles were poorly-dispersed on the support; with some areas having high and others having a much lower particle density. Also, a rod-like shape identified by *in-situ* EDX analysis as tungsten oxide was present. Two regions were generally identified on the catalyst; agglomeration of particles close to the rod-like WO₃ and agglomeration of particles on the carbon support. Due to this agglomeration,

the particle size distribution could not be obtained for PdIr/WO$_3$-C. However, some individual particles sizes were measured from particles found outside of the agglomerate.
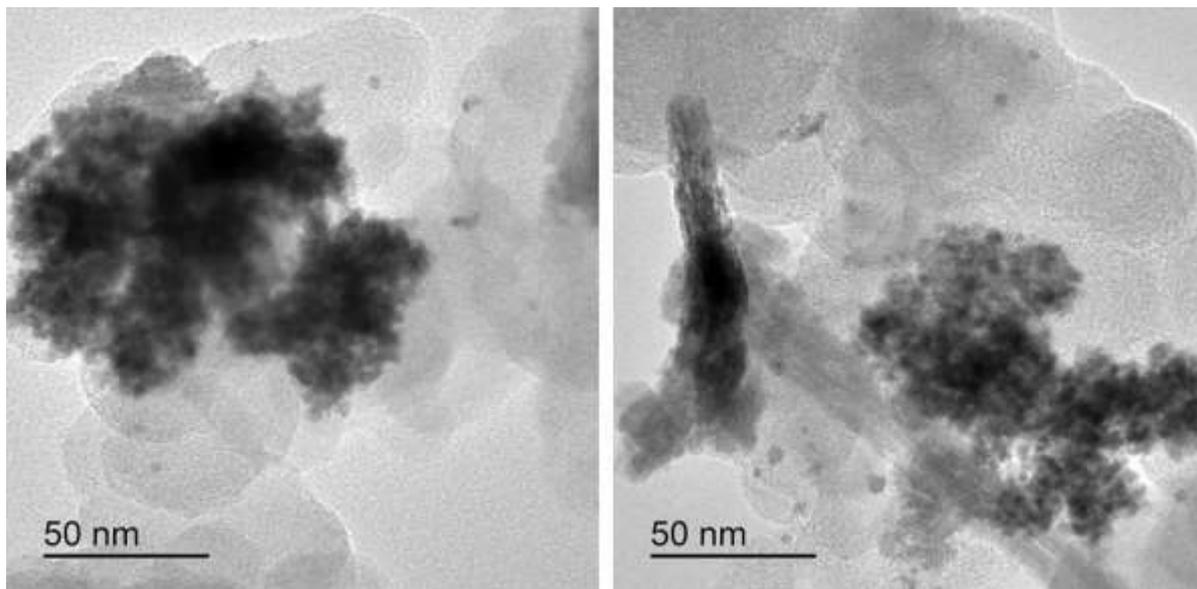
Figure 53: TEM image obtained for PdIr/WO$_3$-C showing agglomeration.

The agglomeration was thought to be due to the use of phosphotungstic acid used in the synthesis of WO$_3$-C support. To synthesise the support, Vulcan was treated with phosphotungstic acid. This acid modified the Vulcan surface and resulted in a more hydrophilic support. The hydrophilic nature of the support could result in the metal nanoparticles being deposited and anchored onto local regions with higher concentration of WO$_3$. Kumar *et al.* [148] observed agglomeration of palladium nanoparticles supported on Vulcan that had been pre-treated with HNO$_3$ in comparison with those supported on untreated Vulcan. They reported that the oxidative HNO$_3$ pre-treatment of Vulcan led to a breakdown of the neighbouring micropore walls and merged them into larger dimensions that favoured the formation of patches of agglomerated palladium. The authors attributed the agglomeration to a lower surface area and micropore volume on the acid-functionalized support. Therefore, the low particle dispersion and agglomeration observed in TEM images for PdIr/WO$_3$-C was attributed to phosphotungstic acid's oxidation of the Vulcan.

It was observed that PdIr/TiO$_2$-C and PdIr/WO$_3$-C had smaller particle sizes than PdIr/C. This was attributed to a stronger interaction between the carbon-oxide support and metal particles than metal particles and carbon. The EDX measurement as shown in Table 14 indicated a slightly higher than the expected average weight percentages of palladium and iridium for PdIr/WO$_3$-C. This was thought to be due to the catalyst's low dispersion of particles on the support resulting in widely varying particle weight averages measured.

Table 14: EDX metal weight averages, average particle sizes estimated from TEM Analysis for PdIr/TiO₂-C, PdIr/WO₃-C and PdIr/C catalysts.

Catalyst	XRD Estimated Crystallite Size (nm)	TEM Particle Size (nm)	EDX Metal Average	
			Pd (% wt.)	Ir (% wt.)
PdIr/TiO$_2$-C	-	4.2	10.7	10.9
PdIr/WO$_3$-C	3.8	4.5	12.3	11.8
PdIr/C	5.6	5.2	10.8	9.6

5.5 X-ray Photoelectron Spectroscopy (XPS) Analysis of Palladium-Iridium Catalysts Supported on TiO₂-C and WO₃-C

XPS was used to analyse the oxidation states and surface composition of the carbon supported metals. For PdIr/TiO$_2$-C, the Pd 3d XPS spectrum was characterized by three pairs of Pd 3d peaks corresponding to metallic Pd^0, palladium with oxygen adsorbed (PdO$_{ads}$) and palladium II oxide respectively (PdO); similar to peaks observed for PdIr/C.

In contrast to PdIr/TiO$_2$-C and PdIr/C, the Pd 3d XPS spectrum for PdIr/WO$_3$-C was characterized by two pairs of Pd 3d peaks corresponding to metallic Pd^0 and palladium II oxide respectively (PdO). This suggests that the presence of WO$_3$ in the catalyst modified the adsorption of oxygen on palladium in a manner different to TiO$_2$.

In addition, a downward shift was noticed in the binding energy of the metallic Pd^0 from 335.6 eV to 335. 4 eV for PdIr/TiO$_2$-C and PdIr/WO$_3$-C when compared with PdIr/C; suggesting an interaction between the metal oxides and palladium. Similar shifts in binding energies have been reported and attributed to strong metal-metal oxide interaction (SMSI) in literature [196, 211]. This XPS data indicating the presence of metal-metal oxide interaction is consistent results from the TEM and XRD analyses.
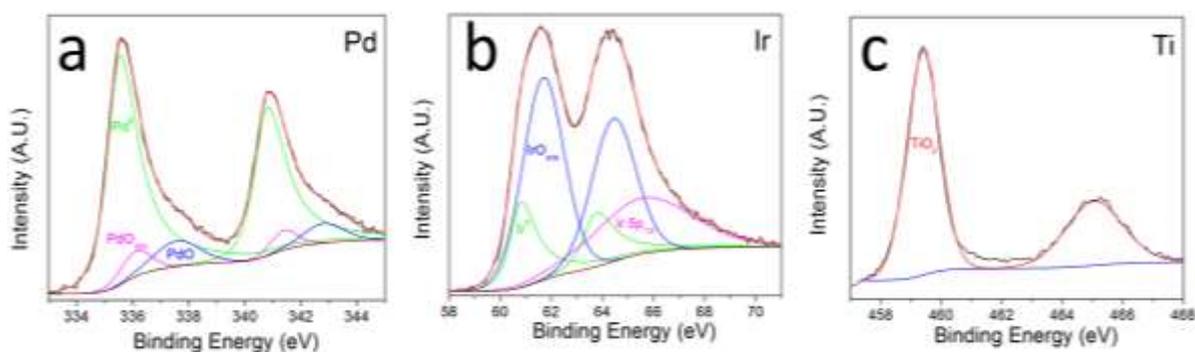
Figure 54: Pd 3d, (labelled a) Ir 4f (labelled b) and Ti 2p (labelled c) XPS Spectra obtained for the PdIr/TiO₂-C catalyst.

The *Ti 2p* XPS spectrum showed the presence of a single component identified as TiO$_2$ [212].
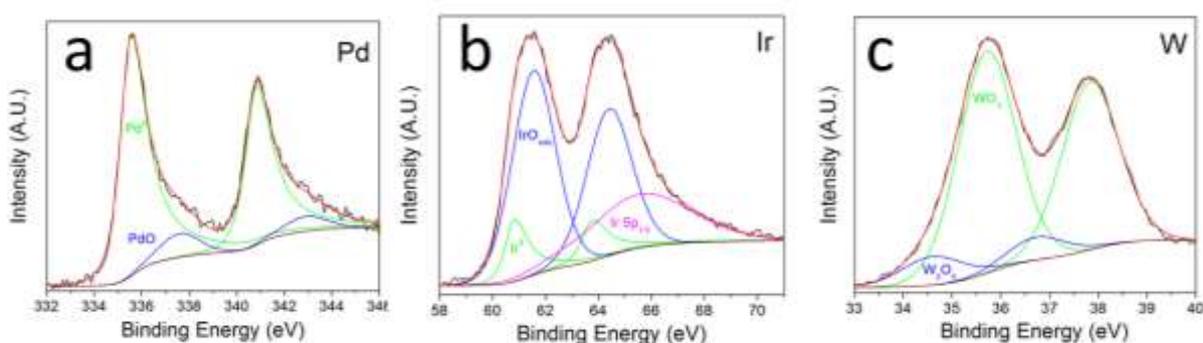
Figure 55: Pd 3d (labelled a), Ir 4f (labelled b) and W 4f (labelled c) XPS Spectra obtained for the PdIr/WO₃-C catalyst.

The *W 4f* spectrum showed the presence of 2 components identified as WO$_3$ and W$_2$O$_5$ [213] with a relatively higher proportion of WO$_3$ to W$_2$O$_5$.

5.6 Cyclic Voltammetry (CV) Characterisation of Palladium-Iridium Catalysts Supported on TiO₂-C and WO₃-C

Cyclic voltammograms recorded for PdIr/TiO$_2$-C, PdIr/WO$_3$-C and PdIr/C at a scan rate of 20 mVs^{-1} in nitrogen between 0.05 and 1.21 V are shown in Figure 56 below. The CVs obtained for PdIr/TiO$_2$-C and PdIr/WO$_3$-C were similar in shape to that of PdIr/C indicating that the three catalysts undergo similar redox processes; the electrochemical features seen were from palladium-iridium nanoparticles. The absence of redox features from TiO$_2$ and WO$_3$ in PdIr/TiO$_2$-C and PdIr/WO$_3$-C was because the main electrochemical processes for TiO$_2$ [214] and WO$_3$ [215] do not occur at the potential range used in this experiment (0.05 to 1.2 V).
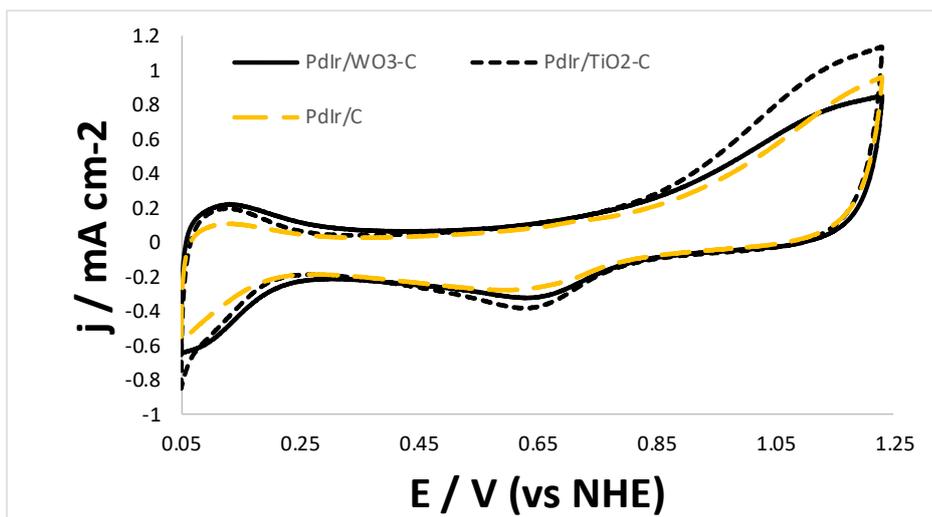
Figure 56: Cyclic voltammograms for PdIr/TiO₂-C, PdIr/WO₃-C and PdIr/C catalysts in N₂ saturated 0.5 M H₂SO₄ at scan rate 20 mVs⁻¹.

Electrochemical surface area (ECSA) was calculated for the three catalysts by quantification of charge under the palladium-oxide reduction peak. The ECSA values obtained were 7.6, 10.8 and 6.1 m^2g^{-1} for the PdIr/C, PdIr/TiO₂-C and PdIr/WO₃-C catalysts respectively.

5.7 Oxygen Reduction Activity Studies of Palladium-Iridium Catalysts Supported on TiO₂-C and WO₃-C

Activity of PdIr/TiO₂-C and PdIr/WO₃-C were evaluated from data obtained from linear sweep voltammograms recorded from a potential 30 mV higher than onset potential to 0.2 V at a scan rate of 5 mVs⁻¹ in oxygen-saturated 0.5 M H₂SO₄.
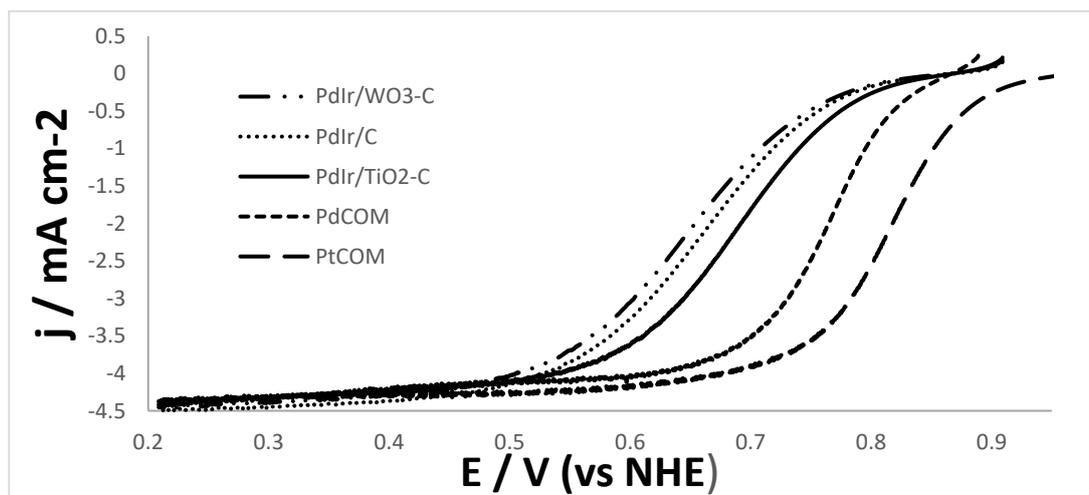
Figure 57: Linear sweep voltammograms obtained for PdIr/TiO₂-C, PdIr/WO₃-C and PdIr/C compared with commercial Pd/C and Pt/C at 900 rpm and a scan rate of 5 mVs⁻¹.

Figure 57 compares linear voltammograms recorded for the prepared PdIr/TiO$_2$-C and PdIr/WO$_3$-C catalysts with PdIr/C, commercial 20 % Pd and 20 % Pt (PdCOM and PtCOM) recorded under similar conditions at a rotation rate of 900 rpm. It can be seen that the commercial Pt/C and Pd/C catalysts had the highest activity. In comparison to PdIr/C, PdIr/TiO$_2$-C exhibited higher activity while PdIr/WO$_3$-C had a lower activity. The higher activity of PdIr/TiO$_2$-C was attributed to its smaller particle sizes as well as a favourable interaction between the TiO$_2$ and the metal particles. Choi *et al.* [216] reported an enhancement in ORR activity when they modified a Pd/C catalyst with TiO$_2$. The lower activity observed with PdIr/WO$_3$-C was attributed to the low dispersion of the metal particles on the WO$_3$-C support as seen in the TEM micrographs.

5.8 Koutecky-Levich Analysis on Palladium-Iridium Catalysts Supported on TiO$_2$-C and WO$_3$-C

Linear sweep voltammograms recorded for PdIr/C, PdIr/TiO$_2$-C and PdIr/WO$_3$-C at rotation rates of 400, 625, 900, 1225 and 1600 rpm were used for a Koutecky-Levich plot in order to evaluate and compare catalyst activities. Figure 58 shows the plot obtained for the three catalysts at a potential of 0.67 V.
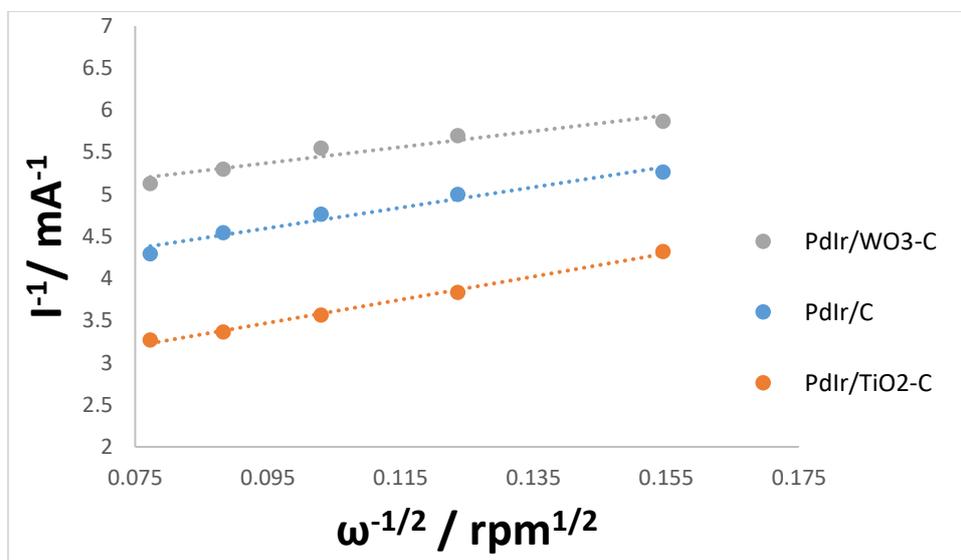
Figure 58: Koutecky-Levich plots obtained for PdIr/C, PdIr/TiO$_2$-C and PdIr/WO$_3$-C catalysts.

Table 15: Kinetic parameters obtained for PdIr/TiO₂-C, PdIr/WO₃-C and PdIr/C catalysts.

Catalyst	Kinetic current at 0.67 V (mA)	Specific Activity at 0.67 V (mAcm⁻²)	Mass Activity at 0.67 V (Ag_metal⁻¹)
PdIr/C	0.47	0.23	86.48
PdIr/TiO₂-C	0.99	0.52	180.51
PdIr/WO₃-C	0.36	0.19	65.21

From the values obtained from the Koutecky-Levich plots in table, PdIr/TiO₂-C had the highest activity. It had a specific activity nearly twice the magnitude of the value obtained for PdIr/C at 0.67 V. This suggests that the use of titanium oxide-carbon composite support for palladium-iridium nanoparticles can improve its ORR activity. PdIr/WO₃-C had a specific activity about one and half times lower than the specific activity of the PdIr/C at 0.67 V. This was thought to be due to particle agglomeration and its lower ECSA.

5.9 Tafel Analysis on Palladium-Iridium Catalysts Supported on TiO₂-C and WO₃-C

Tafel analysis was used in evaluating the activity of the catalysts to quantify the rate of increase in overpotential with current density. Data points for the Tafel plots (Figure 59) were taken from the recorded LSVs for the catalysts at 400 rpm at scan rate 5 mVs⁻¹. A mass transport effect correction was applied to the current density. The Tafel slope and exchange current density values calculated for each catalyst are shown in Table 16.
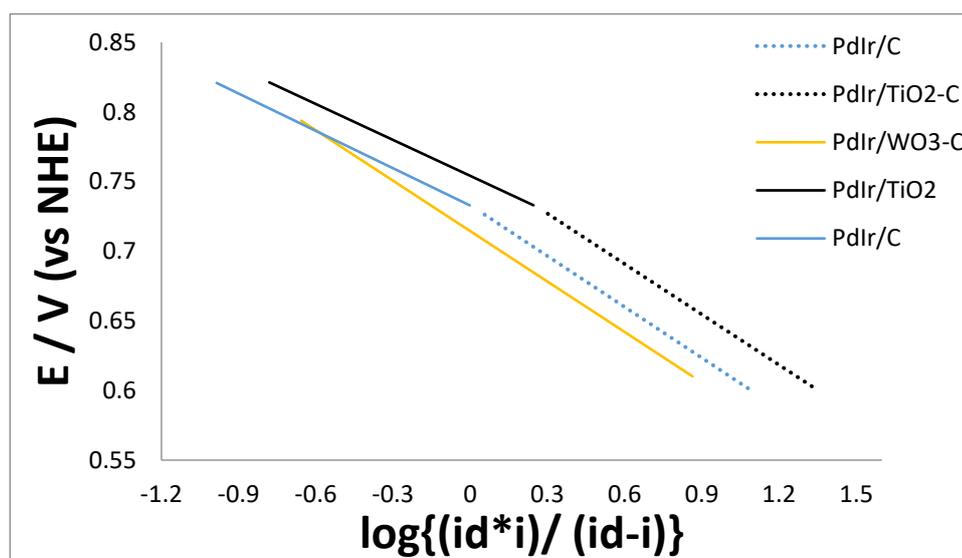
Figure 59: Tafel slopes for PdIr/TiO₂-C (2 slopes in black), PdIr/WO₃-C (single slope in yellow) and PdIr/C (2 slopes in blue).

Table 16: Tafel Slopes and exchange current density obtained for PdIr/TiO$_2$-C, PdIr/WO$_3$-C and PdIr/C catalysts.

Catalyst	Tafel Slope (mVdecade^{-1})	Exchange Current Density (Acm^{-2})
PdIr/C	89	2.8x10^{-13}
	122	5.1x10^{-11}
PdIr/TiO$_2$-C	86	9.2x10^{-13}
	120	0.9x10^{-10}
PdIr/WO$_3$-C	121	2.4x10^{-11}

In contrast to PdIr/C and PdIr/TiO$_2$-C with similar Tafel behaviour and slopes (indicating a similarity in both catalysts' ORR mechanism), PdIr/WO$_3$-C exhibited a single Tafel slope of 121 mVdecade^{-1}. This observation was unexpected as palladium usually has a Tafel slope around 60 mVdecade^{-1} associated with ORR taking place on palladium with a high surface oxide coverage [139]. Since Tafel slope is determined by surface oxidation as a function of potential, the absence of this Tafel slope around 60 mVdecade^{-1} suggests that WO$_3$ can inhibit the adsorption of oxygenated species on palladium during ORR. This Tafel behaviour of PdIr/WO$_3$-C is in good agreement with a single Tafel slope of 122 mVdecade^{-1} reported for a Pt/WO$_3$ catalyst [213].

5.10 Quantification of Hydrogen Peroxide Generated for Palladium-Iridium Catalysts Supported on TiO$_2$-C and WO$_3$-C

The ring currents obtained for PdIr/TiO$_2$-C and PdIr/WO$_3$-C are shown below in Figure 60 along with those obtained from PdIr/C, commercial palladium and commercial platinum catalysts at a rotation rate of 900 rpm. The percentage of peroxide produced during the ORR was quantified at 0.4 V. The percentage peroxide produced were 2.1 %, 2.6 %, 3.2 %, 5.3 % and 7.1 % for the commercial platinum, PdIr/C, PdIr/TiO$_2$-/C, PdIr/WO$_3$-C and commercial palladium catalysts respectively. In comparison to PdIr/C, peroxide yields were slightly higher for PdIr/TiO$_2$-C and PdIr/WO$_3$-C. This is consistent with observations of an increased peroxide yield on catalysts with oxide-based supports [217, 218].
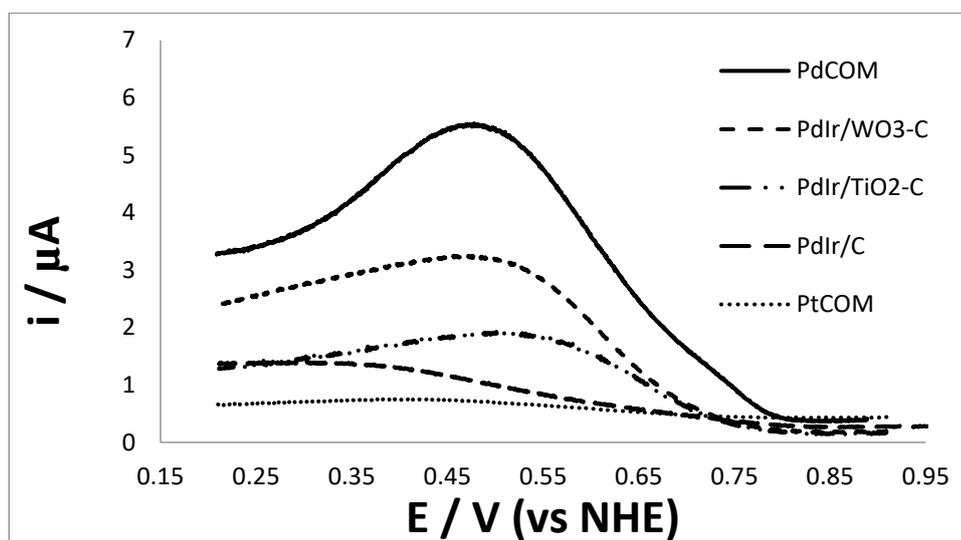
Figure 60: Ring currents obtained for PdIr/TiO₂-C, PdIr/WO₃-C, PdIr/C, commercial Pd/C and Pt/C catalysts at 900 rpm.

5.11 Cyclic Voltammetry (CV) Stability Studies of Palladium-Iridium Catalysts Supported on TiO₂-C and WO₃-C

Cyclic voltammetry was used to study the stability of PdIr/TiO$_2$-C and PdIr/WO$_3$-C catalysts in acid. This was done by recording 100 cyclic voltammograms for each catalyst at a scan rate of 100 mVs^{-1} from 0.05 to 1.2 V in nitrogen-saturated 0.5M H$_2$SO$_4$. The effect of potential cycling on the ECSA was monitored to provide information on catalyst stability. Figures 61 and 62 show the first, tenth, fiftieth and hundredth cyclic voltammograms obtained for both catalysts.
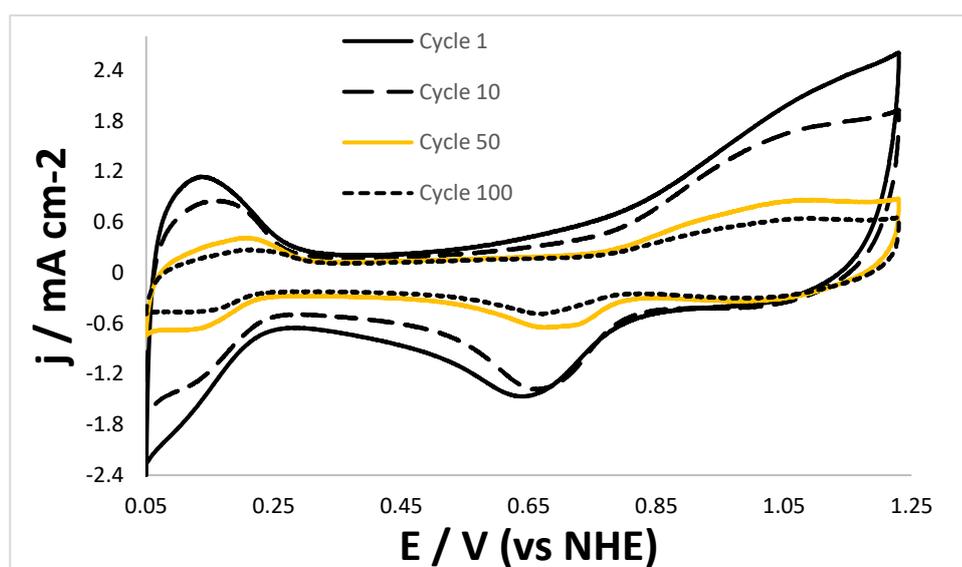
Figure 61: First, tenth, fiftieth and hundredth cyclic voltammograms for PdIr/WO₃-C catalyst during 100 cycles recorded at 100 mVs⁻¹.
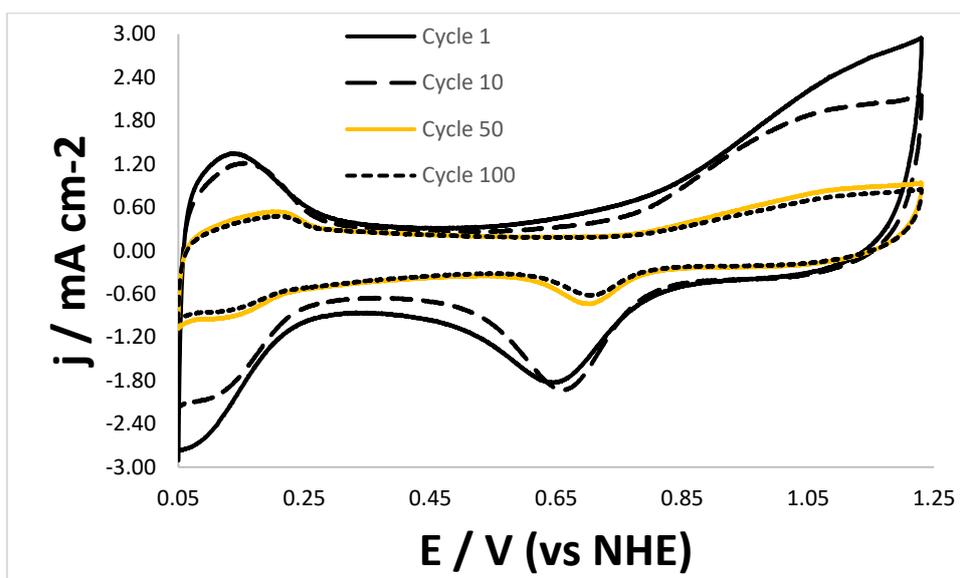
Figure 62: First, tenth, fiftieth and hundredth cyclic voltammograms obtained for PdIr/TiO$_2$-C catalyst during 100 cycles recorded at 100 mVs^{-1}.

From Figures 61 and 62, significant changes to the overall shape of the CVs were observed for both catalysts. These changes were similar to those observed and attributed to ECSA loss resulting from palladium oxidation and particle size increase in PdIr/C (as discussed in Chapter 4). In comparison to PdIr/C (31%), PdIr/TiO$_2$-C and PdIr/WO$_3$-C retained higher percentages of their initial ECSA values; 56 % and 42 % respectively; suggesting the presence of tungsten oxide and titanium oxide in the support was beneficial to improving catalyst stability under potential cycling conditions.

XPS analysis was done for PdIr/TiO$_2$-C and PdIr/WO$_3$-C catalysts after degradation by collecting the used catalysts' particles from the working electrode. The results were compared with those obtained from the PdIr/C catalyst. The images shown in Figures 63 and 64 are of the Pd $3d$ regions obtained for the fresh catalysts and after the catalysts' degradation for PdIr/TiO$_2$-C and PdIr/WO$_3$-C respectively.
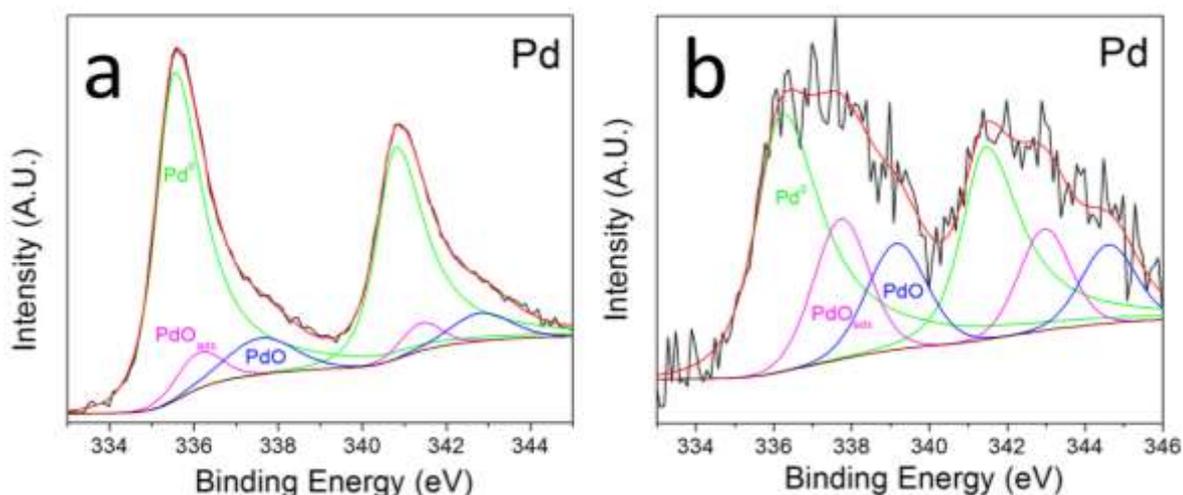
Figure 63: Pd 3d XPS Spectra obtained for PdIr/TiO$_2$-C before (labelled a) and after potential cycling (labelled b).
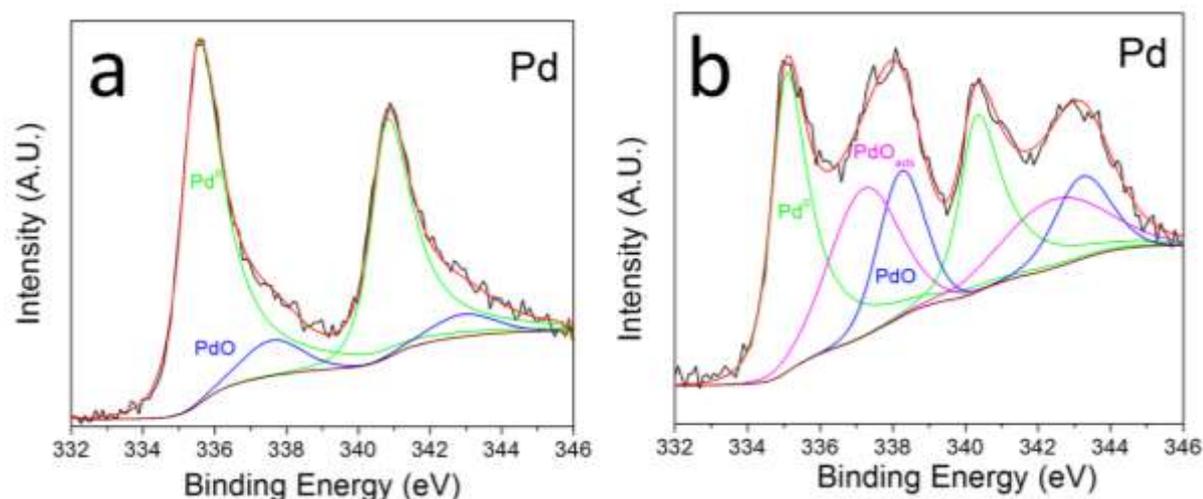
Figure 64: Pd 3d XPS Spectra obtained for PdIr/WO$_3$-C before (labelled a) and after potential cycling (labelled b).

From the TEM images, it can be observed that some changes occurred on the palladium surfaces of PdIr/TiO$_2$-C and PdIr/WO$_3$-C during the potential cycling; the catalysts showed a decrease in the relative ratio of the metallic Pd^0 and an increase in the relative ratios of the oxidised species (PdO$_{ads}$ and PdO). As discussed in previous chapter for PdIr/C, their loss of electrochemical surface area during potential cycling were attributed to an increase in the palladium surface oxidation as revealed by XPS analysis. In comparison to PdIr/C that retained 20 % from its initial ratio of metallic Pd^0, PdIr/TiO$_2$-C and PdIr/WO$_3$-C retained higher percentages of 61 % and 45 % respectively. Their improved stabilities were attributed to a strong metal-metal oxide interaction and its ability to modify palladium's electronic properties and hence making it more resistant to electrochemical oxidation. This is in agreement with

discussions from Shim [219] and Lewera [196] who observed a weakening of the adsorption strength of oxygenated species on a platinum surface as a result of modifying their platinum catalyst with WO_3. A similar observation has been made for a palladium surface by Zhang [194].

Although both oxide-modified catalysts (PdIr/TiO$_2$-C and PdIr/WO$_3$-C) showed enhanced stability relative to Vulcan-supported PdIr/C, the TiO$_2$-containing catalyst (PdIr/TiO$_2$-C) showed a better stability than the WO$_3$ containing PdIr/WO$_3$-C. This difference in stabilities could be a result of TiO$_2$ being more electrochemically stable than WO$_3$. TiO$_2$ is not redox-active in this study's potential range of interest (0.05 to 1.2 V) and it has been suggested that WO$_3$ can undergo the formation of acid-soluble hydrogen tungsten bronze species between 0.08 and 0.22 V [220]. This can lead to a gradual loss of the initially-observed stabilising effect of SMSI on palladium [213] in PdIr/WO$_3$-C. Therefore, an overall higher enhancement in stability during potential cycling was observed for the PdIr/TiO$_2$-C catalyst.
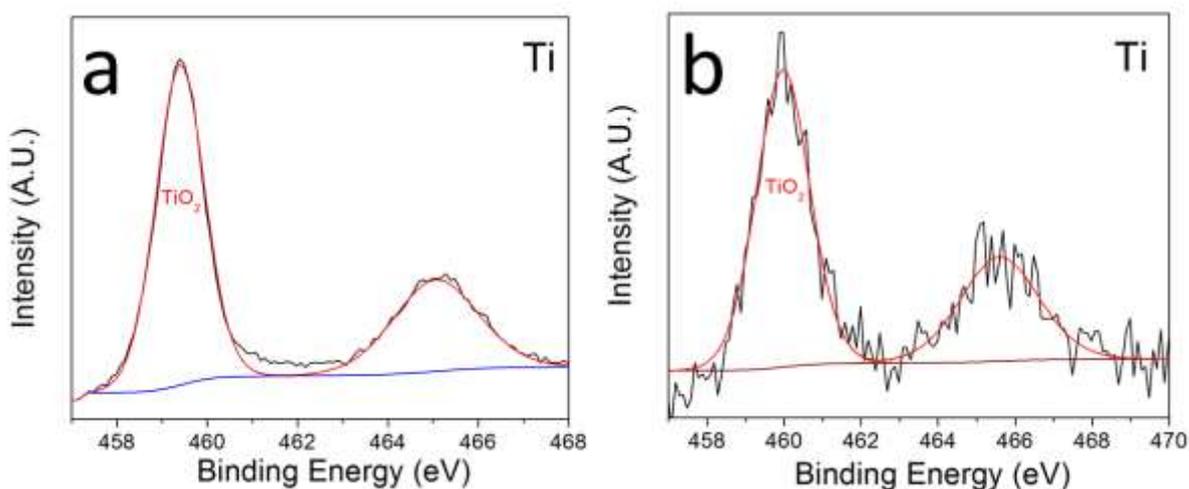
Figure 65: Ti 2p XPS Spectra obtained for PdIr/TiO2-C before (labelled a) and after potential cycling (labelled b).

Figure 65 compares the *Ti 2p* XPS spectra obtained for PdIr/TiO$_2$-C before and after the potential cycling. This showed that no changes to the component or binding energy of TiO$_2$ was observed; it indicates that TiO$_2$ remained stable and demonstrated excellent stability during the potential cycling experiment.
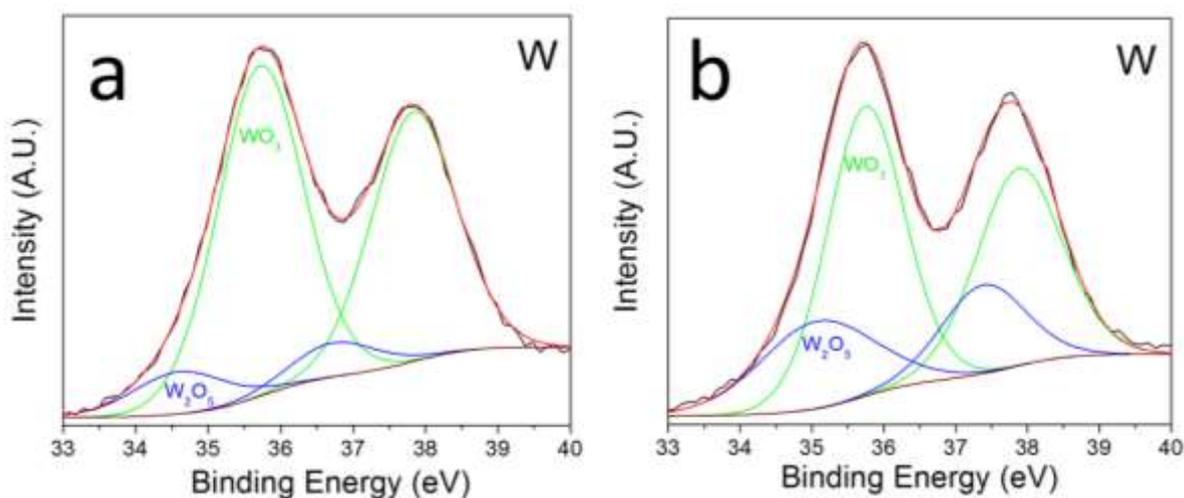
Figure 66: W 4f XPS Spectra obtained for PdIr/WO₃-C before (labelled a) and after potential cycling (labelled b).

Figure 66 compares the *W 4f* XPS spectra obtained for PdIr/WO₃-C before and after the potential cycling. These spectra showed that there was an increase in the relative ratios of W_2O_5 (W^{5+}) to WO_3 (W^{6+}) during the potential cycling. This suggests that potential cycling was associated with a reduction process in WO_3, thereby reducing its stability and the overall stability that was gained via the strong metal-metal oxide interaction between palladium-iridium particles and WO_3. A similar observation was reported by Liu *et al.* for a Pt/WO₃ catalyst after a potential cycling degradation test [213].

5.12 Chronoamperometry Studies of Palladium-Iridium Catalysts Supported on TiO₂-C and WO₃-C

The stability of PdIr/WO₃-C and PdIr/TiO₂-C were evaluated using chronoamperometry. The holding potential each catalyst's half-wave potential. Current was monitored over two hours at a rotation rate of 900 rpm. The obtained current-time plots are shown along with results obtained from PdIr/C, commercial palladium and platinum catalysts in Figure 67. The plots show a normalized current, where 100% is the initial current at 10 seconds for each catalyst.

From Figure 67 below, a steady decay of current was observed for all catalysts. Percentages of ORR current retained were 29 %, 38 %, 18 %, 13 % and 63 % for PdIr/WO₃-C, PdIr/TiO₂-C, PdIr/C, PdCOM and PtCOM catalysts respectively. The commercial platinum, followed by PdIr/TiO₂-C exhibited the highest stability. This is in good agreement with the trend observed in the potential cycling test monitoring the ECSA loss during the cycling.
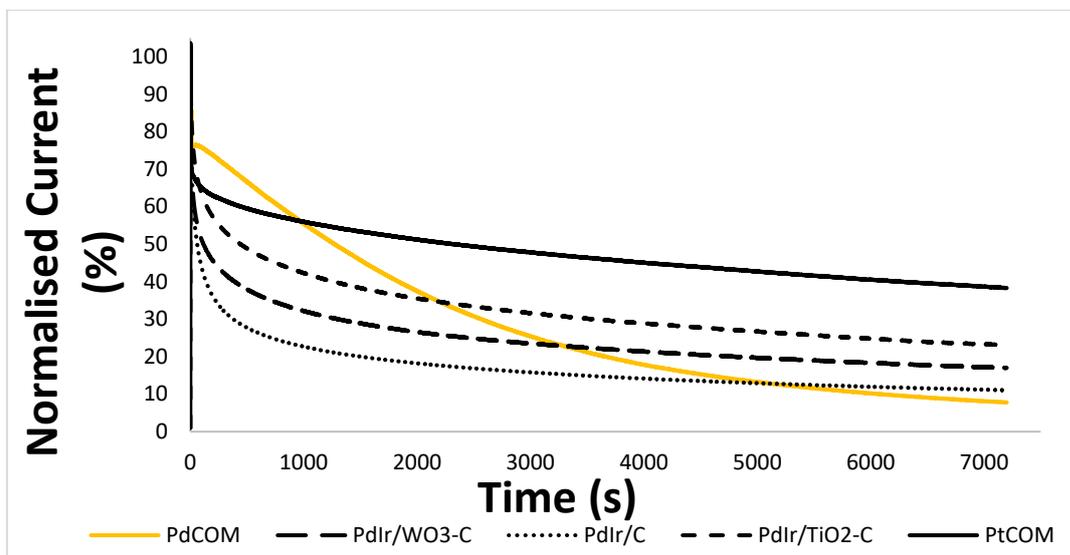
Figure 67: Chronoamperometric response curves obtained for PdIr/TiO$_2$-C, PdIr/WO$_3$-C, PdIr/C, commercial Pd/C and Pt/C normalised to each catalyst's initial current.

5.13 ORR Degradation Studies on Palladium-Iridium Catalysts Supported on TiO$_2$-C and WO$_3$-C

A degradation test was done to evaluate catalysts' stabilities and quantify the loss of activity during ORR for PdIr/WO$_3$-C and PdIr/TiO$_2$-C. The degradation was done through potential cycling between 0.87 V to 0.4 V. These potentials were selected for use to limit the effect of electrochemical processes involving palladium oxidation. At the start of the experiment, 3 cyclic voltammograms were recorded in a nitrogen-saturated 0.5 M H$_2$SO$_4$ from 0.05 to 1.2 V at a scan rate of 20 mVs^{-1} to determine the ECSA of the catalyst. After the CVs were recorded, the catalysts were subjected to 1000 cycles of potential cycling between 0.87 and 0.4 V at a scan rate of 0.2 Vs^{-1} in an oxygen-saturated 0.5 M H$_2$SO$_4$ with no electrode rotation and the maintenance of oxygen flow to the electrolyte. After the thousandth cycle, 3 CVs were recorded in nitrogen under similar conditions to those at the start of the experiment. The results were evaluated by comparing ECSA values obtained before and after the potential cycling. The results were also compared with those obtained for PdIr/C. Figures 68 and 69 shows the initial and final CVs obtained for PdIr/WO$_3$-C and PdIr/TiO$_2$-C catalysts.
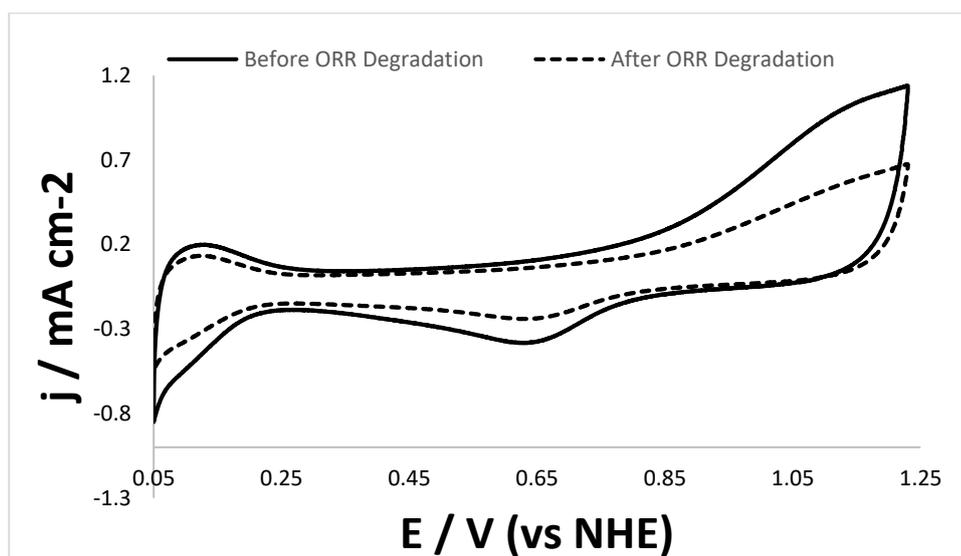
Figure 68: Cyclic voltammograms obtained for the PdIr/WO$_3$-C catalyst before and after ORR degradation recorded at 20 mVs^{-1} in N$_2$-saturated H$_2$SO$_4$.
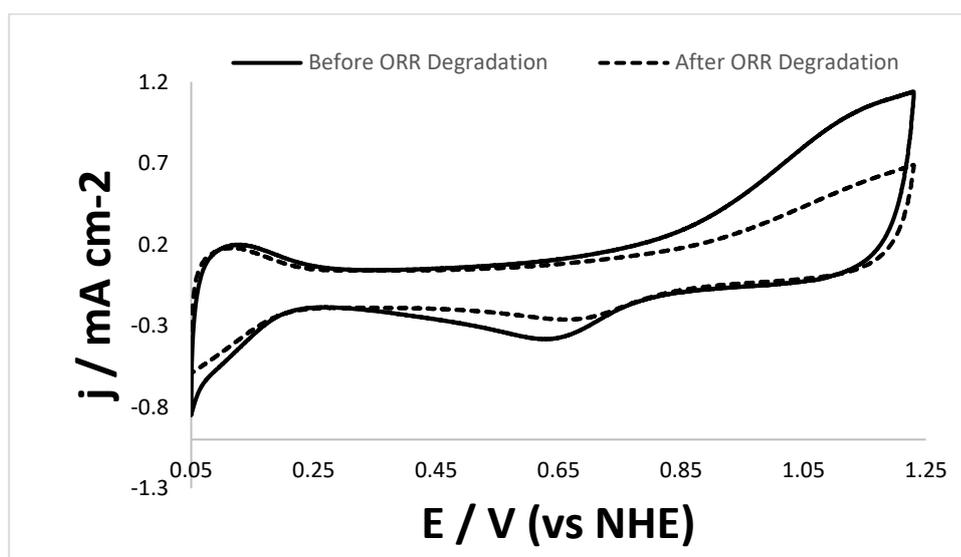
Figure 69: Cyclic voltammograms obtained for the PdIr/TiO$_2$-C catalyst before and after ORR degradation recorded at 20 mVs^{-1} in N$_2$-saturated H$_2$SO$_4$.

The CVs recorded for both catalysts after the potential cycling showed a decrease in intensity of the peaks related to hydrogen adsorption and desorption as well as surface oxide formation and surface oxide-reduction. In addition to this, a shift to a higher potential value for the oxide-reduction peak; usually associated with particle size increase was observed. This observation is indicative of a reduction in the electrochemical surface area resulting from particle agglomeration. The observations are similar to those obtained for PdIr/C. The ECSA of

PdIr/WO₃-C and PdIr/TiO₂-C after degradation were found to be 68 % and 79 % of their initial values. These catalysts display higher stability than PdIr/C that retained 52 % of its initial ECSA.

Table 17: Percentages of ECSA retained after nitrogen potential cycling, metallic Pd⁰ retained, chronoamperometric current retained and ECSA retained after ORR degradation in oxygen obtained for PdIr/C, PdIr/TiO₂-C, PdIr/WO₃-C, commercial Pd/C and Pt/C catalysts.

Catalyst	% of ECSA retained after potential cycling (0.05 to 1.2 V in N_2)	% XPS' Pd^0 retained after potential cycling	% of current retained from chronoamperometry	% of ECSA retained after degradation (0.87 to 0.4 V in O_2)
PdIr/TiO₂-C	56	61	38	79
PdIr/WO₃-C	42	45	29	68
PdIr/C	31	20	18	56

TEM analysis was done for PdIr/TiO₂-C after the degradation by collecting the used catalyst particles from the working electrode after the ORR degradation experiment was completed. The results obtained were compared with PdIr/C so as further investigate the effect of the presence of TiO₂ in the catalyst. The representative micrographs shown in Figures 70 and 71 compares the initial morphology of PdIr/C and PdIr/TiO₂-C as prepared with their final morphology after the ORR degradation test.
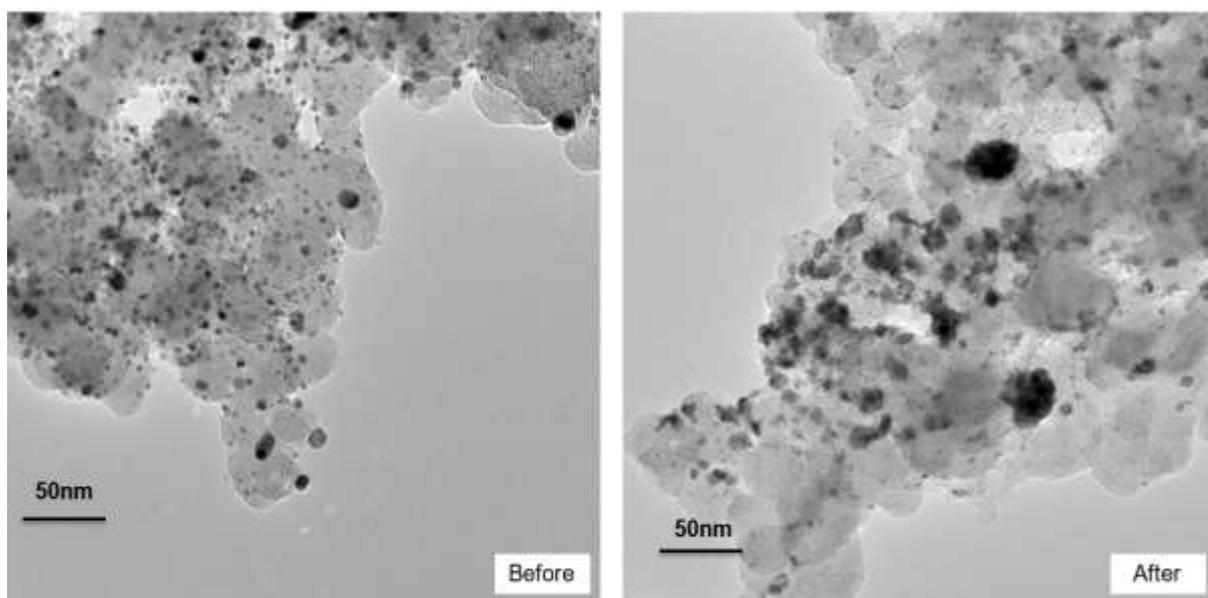
Figure 70: TEM image obtained for PdIr/C before and after the ORR degradation in oxygen.

As discussed in the previous chapter, the TEM image obtained for PdIr/C after the ORR degradation revealed an overall lower particle density as well as larger particles on the carbon support.
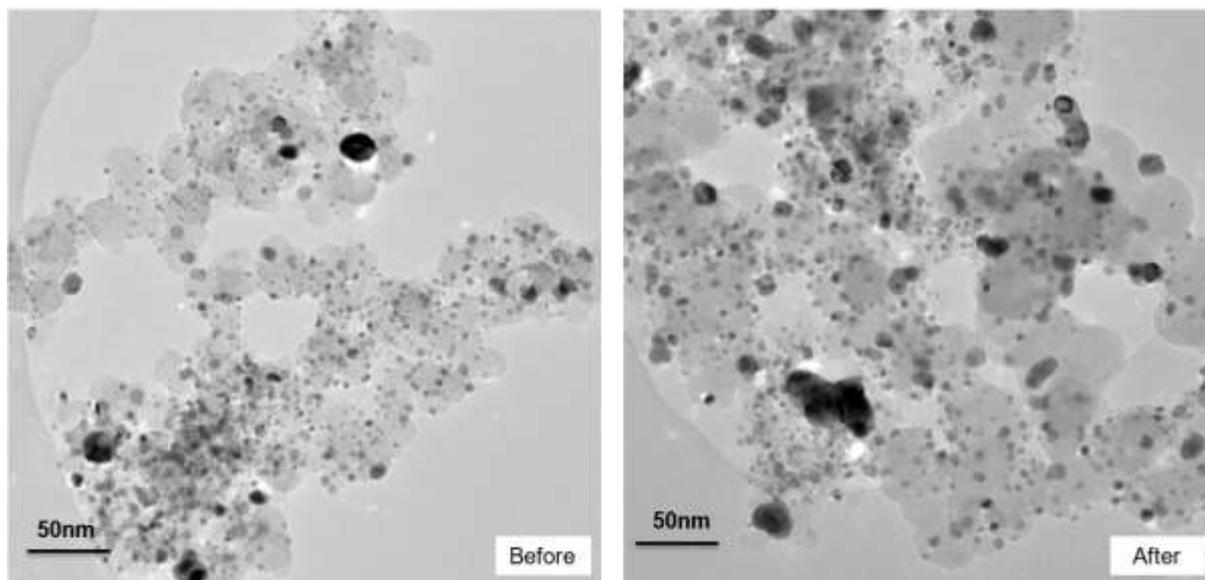
Figure 71: TEM image obtained for PdIr/TiO$_2$-C before and after the ORR degradation in oxygen.

For PdIr/TiO$_2$-C, only a small increase in particle size was observed. Overall, the catalyst was able to maintain a fairly similar particle density and dispersion on the support. A comparison between the micrographs obtained for PdIr/C and PdIr/TiO$_2$-C suggests a more extensive change in morphology to PdIr/C after ORR degradation. This corroborates the observed ECSA loss of 21 % and 48 % for PdIr/TiO$_2$-C and PdIr/C respectively during the ORR degradation test. The higher stability of PdIr/TiO$_2$-C is indicative of a stronger interaction between the palladium-iridium particles supported on the TiO$_2$-Vulcan support than palladium-iridium supported purely on carbon. Strong metal-metal oxide interaction has been reported to be the reason for the reduced agglomeration of particles [196, 201]. Shih and Chang observed that the strong metal-metal oxide interaction between metal particles and TiO$_2$ can anchor the particles more strongly and hence inhibit particle migration and agglomeration [221].

5.14 Conclusions

Palladium-iridium catalysts supported on metal oxide-carbon composites; TiO$_2$-C and WO$_3$-C were successfully synthesised by a polyol method in ethylene glycol. The average particle sizes were 4.2 and 4.5 nm for PdIr/TiO$_2$-C and PdIr/WO$_3$-C catalysts respectively. XRD and XPS analyses revealed an alloying interaction between palladium and iridium as well as interaction between the metal oxides in the support and the palladium. TEM images showed that PdIr/TiO$_2$-

C had a good dispersion of metal nanoparticles on the support while PdIr/WO$_3$-C's particles were poorly-dispersed on the support; with some areas having higher and others having a much lower particle density.

Electrochemical characterisation showed similar CV profiles for PdIr/TiO$_2$-C and PdIr/WO$_3$-C; these CVs were comparable to a CV of PdIr/C. The ECSA values obtained were 7.6, 10.8 and 6.1 m^{2}g^{-1} for the PdIr/C, PdIr/TiO$_2$-C and PdIr/WO$_3$-C catalysts respectively. Koutecky-Levich analysis was used to calculate kinetic current and hence specific and mass activities of the catalysts. Specific activities obtained at 0.67 V were 0.23, 0.52 and 0.19 mAcm^{-2} for PdIr/C, PdIr/TiO$_2$-C and PdIr/WO$_3$-C catalysts respectively. In comparison to PdIr/C, the enhanced activity for PdIr/TiO$_2$-C was attributed to its smaller particle sizes as well as a favourable interaction between the TiO$_2$ and the metal particles. The reduced activity for PdIr/WO$_3$-C was attributed to the low dispersion of the metal particles on the WO$_3$-C support. Tafel analyses showed that PdIr/C and PdIr/TiO$_2$-C exhibited 2 slopes with values around 90 and 120 mVdecade^{-1} in the low and high current density regions respectively, while PdIr/WO$_3$-C only had a single Tafel slope around 120 mVdecade^{-1}. Since Tafel slope is determined by surface oxidation as a function of potential, the absence of the lower Tafel slope suggests that WO$_3$ can inhibit the adsorption of oxygenated species on Pd during ORR. The peroxide yield for PdIr/TiO$_2$-C and PdIr/WO$_3$-C were slightly higher than PdIr/C.

Potential cycling from 0.05 to 1.2 V over 100 cycles revealed significant ECSA loss of 44 and 58 % for PdIr/TiO$_2$-C and PdIr/WO$_3$-C, in comparison to 69 % loss observed for PdIr/C. These results demonstrate that the metal oxide-based catalysts had relatively higher stability in comparison to PdIr/C. XPS analysis done on catalysts after the potential cycling revealed increased relative amounts of oxidised surface palladium species in all three catalysts. PdIr/TiO$_2$-C and PdIr/WO$_3$-C were observed to have retained higher percentages of metallic Pd^0 (61 and 45 % respectively) than PdIr/C catalyst (20 %). This suggested that the strong metal-metal oxide interaction between metal nanoparticles and TiO$_2$ as well as WO$_3$ resulted in a modification of palladium's electronic properties and increased its resistance to electrochemical surface oxidation. PdIr/TiO$_2$-C was found to possess a higher stability than PdIr/WO$_3$-C. This was attributed to a slow reduction of WO$_3$ to W$_2$O$_5$ leading to a gradual loss of the initially-observed stabilising effect of SMSI on palladium.

Similar trends in stability data of the catalysts were obtained when catalysts were subjected to chronoamperometry and a milder ORR degradation test between 0.87 and 0.4 V. TEM analysis done after the mild ORR degradation revealed agglomeration and particle size increase as the

cause of ECSA loss. In comparison to PdIr/C, the extent of agglomeration and particle size increase was lower for PdIr/TiO$_2$-C; corroborating the lower loss in ECSA observed for it.

From these results, the use of metal oxide-carbon composite supports was observed to be beneficial to improving palladium's stability in acid media due to a modification in palladium's interaction with oxygenated species. In comparison, the use of TiO$_2$-C resulted in enhanced ORR activity while a decreased ORR activity was observed with WO$_3$-C due to agglomeration and poor particle dispersion on the support. This indicates that further research is needed into producing PdIr/ WO$_3$-C catalysts with better morphology and higher particle size distribution.

Chapter 6. Conclusions and Future Works

6.1 Conclusions

In a bid to improve ORR activity, palladium is usually alloyed with first-row transition metals [33, 59, 65, 71] which are easily corroded under acidic fuel cell conditions, leading to a loss of catalyst stability in PEM fuel cells.

This research provides a deeper insight into improving the stability of palladium-based catalysts for oxygen reduction in acidic PEM fuel cells by the modification of palladium with acid-stable metals such as gold and iridium. It also discusses the catalytic effect of the strong metal-support interaction between palladium-iridium nanoparticles and titanium oxide as well as tungsten oxide. In addition, it provides an understanding of the degradation mechanisms of palladium such as particle agglomeration and electrooxidation.

This study found that modifying palladium with gold or iridium improved its ORR stability in the acidic environment. Although this improved stability was associated with a reduction in ORR activity for both metals used, the effect was more pronounced for the gold-modified palladium catalysts. This was attributed to the lower ORR activity of gold compared to iridium. A further enhancement in stability was obtained for palladium-iridium nanoparticles supported on carbon-metal oxide hybrid supports (TiO_2-C and WO_3-C). It was observed that the TiO_2-C support was able to improve both ORR activity and stability while WO_3-C improved ORR stability only. This effect was attributed to differences in the catalysts' particle size and morphology; nanoparticles deposited on the TiO_2-C support were smaller and more uniformly distributed than those deposited on WO_3-C.

The prepared catalysts were characterised with techniques such as XRD, TEM and XPS to study catalysts' morphology, alloying as well as their surface species. The catalysts were synthesised using a polyol method with ethylene glycol as a mild reducing agent that yielded small nanoparticles of about 5 nm.

Pd_3Au/C and PdAu/C were prepared and their initial cyclic voltammograms revealed a similar redox behaviour to Pd/C but with lower electrochemical surface areas of 6.2 and 2.5 m^2g^{-1} respectively compared with Pd/C (15.6 m^2g^{-1}). The lower ECSA values obtained for the palladium-gold catalysts was attributed to the presence of gold in the catalysts as gold can hinder the reduction of surface-oxides on palladium. The polarisation curves of the palladium-gold catalysts showed lower onset potentials than the benchmark catalysts of prepared Pd/C, commercial Pd/C and commercial Pt/C. The lower ORR activity of palladium-gold catalysts was reflected in their exchange current densities which were in the order of 10^{-14}, about 2 times lower in order of magnitude than values obtained for Pd/C catalysts around 10^{-12}. The stability

tests indicated the catalyst with the higher gold to palladium ratio (PdAu/C) was more stable than the Pd$_3$Au/C and Pd/C catalysts as it retained 38 % of its initial chronoamperometric current over 2 hours while Pd$_3$Au/C and Pd/C retained 31 % and 16 % of theirs respectively. The improved ORR stability of the palladium-gold catalysts was attributed to the segregation of gold to the catalyst surface during potential cycling to protect palladium from the oxidation.

PdAu/C, Pd$_3$Au/C, prepared Pd/C and commercial Pd/C exhibited single Tafel slopes around 60 mV decade^{-1}. The similarity in Tafel behaviour of the palladium-gold catalysts with Pd/C catalysts indicated that the modification of palladium with gold did not change its ORR mechanism. In comparison to Pd/C, a 5-fold increase in amount of peroxide intermediates detected was observed during ORR on the palladium-gold catalysts. This increased peroxide yield could render palladium-gold catalysts unsuitable for use in PEMFCs where the four-electron reduction pathway is preferred.

The modification of palladium with iridium resulted in relatively low ORR activity of the PdIr/C and PdIrAu/C catalysts, with ECSA of 7.6 and 8.2 m^{2}g^{-1} and specific activities of 0.23 and 0.29 mAcm^{-2} respectively (at 0.67 V). However, PdIr/C and PdIrAu/C had higher ORR activities than the palladium-gold catalysts. In contrast to Pd/C, Tafel analyses showed that PdIr/C and PdIrAu/C exhibited two slopes around 90 and 120 mVdecade^{-1}. The exchange current densities for PdIr/C and PdIrAu/C were in the order of 10^{-13}; about one order of magnitude lower than values obtained for Pd/C catalysts (10^{-12}). The peroxide yield for the PdIr/C (2.6 %) and PdIrAu/C (3.5 %) were comparable to the 2.1 % yield obtained for the commercial Pt/C as expected, since ORR on iridium usually proceeds via the direct four-electron reduction pathway.

In comparison to prepared Pd/C (78 % ECSA loss) and commercial Pd/C (91 % ECSA loss), PdIr/C and PdIrAu/C also exhibited enhanced stability with 69 % and 62 % ECSA loss respectively during an oxidative potential cycling stability test. XPS analyses performed on the catalysts after this potential cycling test showed that PdIr/C and PdIrAu/C retained 20 % and 28 % ratio of metallic Pd^0 on their surfaces respectively while the commercial Pd/C retained only 12 %; indicating that PdIr/C and PdIrAu/C were more stable and became less oxidised during the potential cycling as they were able to retain a higher ratio of metallic Pd^0 on their surfaces after the stability test. During a 'milder' ORR degradation study involving potential cycling at lower and non-oxidising potentials (0.87 to 0.4V), PdIr/C lost only 44 % of its initial ECSA while the commercial Pd/C had lost 72 %. A comparison of the TEM images taken before and after the ORR degradation tests revealed that agglomeration and particle size growth

had occurred for both catalysts during the experiment. Although the effects were more pronounced for Pd/C than PdIr/C; indicating that iridium modification made palladium more resistant to agglomeration during ORR. This could make palladium-iridium catalysts potentially suitable for ORR catalysis in acidic PEM fuel cells.

The modification of Vulcan with TiO_2 as support material for palladium-iridium nanoparticles resulted in enhanced ORR activity of the PdIr/TiO_2-C catalyst while a similar modification with WO_3 resulted in reduced ORR activity for the PdIr/WO_3-C catalyst. PdIr/TiO_2-C and PdIr/WO_3-C had ECSA values of 10.8 and 6.1 m^2g^{-1} and specific activities of 0.52 and 0.19 $mAcm^{-2}$ respectively (at 0.67 V). Tafel analyses indicated a similar Tafel behaviour for PdIr/C and PdIr/TiO_2-C with 2 slopes around 90 and 120 $mVdecade^{-1}$ at the low and high current density regions respectively while PdIr/WO_3-C only had a single Tafel slope around 120 $mVdecade^{-1}$. In comparison to PdIr/TiO_2-C, this unexpected absence of the lower Tafel slope for PdIr/WO_3-C suggests that WO_3 could inhibit the adsorption of oxygenated species on palladium during ORR at the low current density region.

In comparison to PdIr/C (69 % ECSA loss), stability tests indicated that PdIr/TiO_2-C and PdIr/WO_3-C had enhanced ORR stability with ECSA loss of 44 and 58 % respectively. XPS analyses performed on the catalysts after the potential cycling revealed an increase in the relative ratio of oxidised palladium species in all three catalysts. PdIr/TiO_2-C and PdIr/WO_3-C retained higher ratios of metallic Pd^0 (61 and 45 % respectively) than PdIr/C catalyst (20 %) on their surfaces after the potential cycling test. This suggests that the interaction between palladium and TiO_2 as well as WO_3 resulted in a modification of palladium's electronic properties and increased its resistance to electrochemical surface oxidation. The higher stability of the PdIr/TiO_2-C compared to PdIr/WO_3-C was attributed to a slow reduction of WO_3 to W_2O_5 leading to a gradual loss of the initially-observed stabilising effect of WO_3 on palladium.

In conclusion, this study found that although gold and iridium modification of palladium resulted in reduced ORR activity, both modifications enhanced palladium's ORR stability in the acidic environment. It also found that the strong metal-metal oxide interaction between the hybrid support (TiO_2-C and WO_3-C) and palladium-iridium nanoparticles could improve ORR stability. An enhanced ORR activity was also observed for the palladium-iridium nanoparticles supported on TiO_2-C. Therefore, PdIr/TiO_2-C was found to be the best catalyst synthesised due to its relatively higher ORR activity and stability than PdIr/C.

Although this research found that alloying of palladium with iridium as well as using a hybrid support of Vulcan and TiO_2 resulted in enhanced ORR stability, the prepared catalysts' ORR

activity and stability were much lower than platinum's. Therefore, these catalysts will not be suitable for use in PEM fuel cells where high ORR activity and stability is essential.

6.2 Future Works

Although palladium and palladium-based catalysts are usually reported to have relatively good ORR activities [33, 37, 222], the palladium-based catalysts prepared and studied in this research had ORR activities much lower than expected. Therefore, further work is necessary to develop ways of maximising their activities without sacrificing stabilities. Although an alloy of palladium and iridium supported on a hybrid support of Vulcan and TiO_2 was found to the most stable catalyst prepared and studied in this work, its stability was inferior to that of the benchmark platinum catalyst. This indicates that further research is needed towards improving the stability of the palladium-based catalysts.

In this study, XRD analysis revealed the presence of palladium and gold in unalloyed phases. Therefore, the effect of heat treatment would be studied as this can induce alloying and more structural changes that can be beneficial to ORR activity and stability. Lee *et al.* reported formation of palladium-gold alloyed phases only when the as-synthesised catalysts were heat-treated [223].

In the literature, gold doping has been explored as a means of improving the durability of platinum-based catalysts. Gatalo *et al.* [224] reported enhanced stability as a result of doping their $PtCu_3/C$ catalyst with less than 1 % gold. They attributed this positive effect to a formation gold-platinum skin with improved corrosion resistance against copper dissolution. It would be beneficial to study this effect on palladium-based catalysts. Even though the effect of gold modification on palladium was studied in this research, the use of much lower amounts of gold (less than 1 %) for the doping effect is recommended for future studies. This study found an increased peroxide yield during ORR, therefore reducing the amounts of gold used for palladium modification via doping could reduce peroxide yield and make the catalysts more suitable for PEMFCs.

Although this study found iridium to improve the stability of palladium, iridium had a detrimental effect on ORR activity. Therefore, the effect of morphology on catalyst activity would be investigated, as ORR activity has been reported to be dependent on catalyst morphology. Xiao *et al.* reported palladium nanorods with ORR activity comparable to platinum; as a result of a ten-fold increase in ORR specific activity for their palladium nanorods compared to nanoparticles [225]. The use of palladium nanocubes led to a three-fold increase in ORR specific activity compared to spherical nanoparticles for Erikson et al [222]. Yang *et*

al. [170, 171] prepared a series of palladium-iridium nanowires and nanocrystals and reported improved activity as well as stability for these catalysts in acidic media. The authors attributed these enhancements to the high surface area morphology and the presence of iridium in the catalysts. It would be interesting to vary the synthetic conditions and develop palladium alloy nanostructures to further the research, as only nanoparticles were investigated in this study. Also, a compositional optimisation of palladium to iridium ratios needed for ORR stability enhancements without reduction in ORR activity would be studied.

In this study, a strong metal-metal oxide interaction was found to improve the stability of palladium-iridium catalysts supported on carbon-metal oxide hybrids. It would be interesting to extend the study to palladium-gold alloys as well as use other transition metal oxides such as niobium oxide. Also, the TiO_2 on Vulcan used in this study was found to be the anatase phase. Therefore, the study can be extended to other phases of TiO_2 especially rutile. Dhanasekaran [226] reported improved ORR activity and stability of platinum nanoparticles supported on rutile TiO_2 compared with platinum supported on anatase TiO_2. In this study, the palladium-iridium nanoparticles supported on WO_3-C were seen as agglomerates in TEM images. Therefore, a new method of synthesis would be investigated to prevent agglomeration; particularly the use of a non-oxidising WO_3 precursor such as sodium tungstate. For instance, Feng *et al.* [208] observed differences in activity and stability for a series of Pd/WO_3-C catalysts for formic acid oxidation based on the precursor and heat treatment used to generate the WO_3-C support.

Another method of protecting palladium from corrosion without comprising its activity would be the deposition of a platinum layer on palladium and palladium-based catalysts which has been reported to improve both activity and stability to being comparable to platinum [114, 227]. Strain and electronic effects have been reported as the source of improved activity. The platinum shell was reported to reduce the dissolution of the palladium core. This protective core-shell effect would be investigated and extended to other acid stable metals like gold and iridium.

References

1.   Andújar, J.M. and F. Segura, *Fuel cells: History and updating. A walk along two centuries.* Renewable and Sustainable Energy Reviews, 2009. **13**(9): p. 2309-2322.

2.   Kirubakaran, A., S. Jain, and R.K. Nema, *A review on fuel cell technologies and power electronic interface.* Renewable and Sustainable Energy Reviews, 2009. **13**(9): p. 2430-2440.

3.   Wang, Y., et al., *A review of polymer electrolyte membrane fuel cells: Technology, applications, and needs on fundamental research.* Applied Energy, 2011. **88**(4): p. 981-1007.

4.   Peighambardoust, S.J., S. Rowshanzamir, and M. Amjadi, *Review of the proton exchange membranes for fuel cell applications.* International Journal of Hydrogen Energy, 2010. **35**(17): p. 9349-9384.

5.   Supramaniam, S., *'2006' Fuel Cells: From Fundamentals to Applications*. New York: Springer.

6.   Scott, K. and A.K. Shukla, *Polymer electrolyte membrane fuel cells: Principles and advances.* Reviews in Environmental Science and Biotechnology, 2004. **3**(3): p. 273-280.

7.   Li, Q., et al., *Approaches and Recent Development of Polymer Electrolyte Membranes for Fuel Cells Operating above 100 °C.* Chemistry of Materials, 2003. **15**(26): p. 4896-4915.

8.   Li, Q., et al., *The CO Poisoning Effect in PEMFCs Operational at Temperatures up to 200[degree]C.* Journal of The Electrochemical Society, 2003. **150**(12): p. A1599-A1605.

9.   Gewirth, A.A. and M.S. Thorum, *Electroreduction of Dioxygen for Fuel-Cell Applications: Materials and Challenges.* Inorganic Chemistry, 2010. **49**(8): p. 3557-3566.

10.   Stacy, J., et al., *The recent progress and future of oxygen reduction reaction catalysis: A review.* Renewable and Sustainable Energy Reviews, 2017. **69**: p. 401-414.

11.   Sui, S., et al., *A comprehensive review of Pt electrocatalysts for the oxygen reduction reaction: Nanostructure, activity, mechanism and carbon support in PEM fuel cells.* Journal of Materials Chemistry A, 2017. **5**(5): p. 1808-1825.

12.   Song, C. and J. Zhang, *Electrocatalytic Oxygen Reduction Reaction*, in *PEM Fuel Cell Electrocatalysts and Catalyst Layers: Fundamentals and Applications*, J. Zhang, Editor. 2008, Springer. p. 89-116

13.   Wu, J. and H. Yang, *Platinum-Based Oxygen Reduction Electrocatalysts.* Accounts of Chemical Research, 2013. **46**(8): p. 1848-1857.

14.   Ramaswamy, N., N. Hakim, and S. Mukerjee, *Degradation mechanism study of perfluorinated proton exchange membrane under fuel cell operating conditions.* Electrochimica Acta, 2008. **53**(8): p. 3279-3295.

15.   Sawyer, D.T. and R.J. Day, *Kinetics for oxygen reduction at platinum, palladium and silver electrodes.* Electrochimica Acta, 1963. **8**(8): p. 589-594.

16.   Damjanovic, A. and V. Brusić, *Oxygen reduction at Pt-Au and Pd-Au alloy electrodes in acid solution.* Electrochimica Acta, 1967. **12**(9): p. 1171-1184.

17.   Ernest, Y., *Dioxygen electrocatalysis: mechanisms in relation to catalyst structure.* Journal of Molecular Catalysis, 1986. **38**(1–2): p. 5-25.

18.   Mahata, A., et al., *A free-standing platinum monolayer as an efficient and selective catalyst for the oxygen reduction reaction.* Journal of Materials Chemistry A, 2017. **5**(11): p. 5303-5313.

19.   Yeager, E., *Electrocatalysts for O2 reduction.* Electrochimica Acta, 1984. **29**(11): p. 1527-1537.

20.   J. K. Nørskov, J. Rossmeisl,A. Logadottir, and, L. Lindqvist, J. R. Kitchin, T. Bligaard, and H. Jónsson, *Origin of the Overpotential for Oxygen Reduction at a Fuel-Cell Cathode*. 2004: The Journal of Physical Chemistry B.

21.   El-Deab, M.S. and T. Ohsaka, *Electrocatalysis by nanoparticles: oxygen reduction on gold nanoparticles-electrodeposited platinum electrodes*. Journal of Electroanalytical Chemistry, 2003. **553**(0): p. 107-115.

22.   Sievers, G., et al., *Mesoporous Pt–Co oxygen reduction reaction (ORR) catalysts for low temperature proton exchange membrane fuel cell synthesized by alternating sputtering*. Journal of Power Sources, 2014. **268**: p. 255-260.

23.   Schenk, A., et al., *Platinum–cobalt catalysts for the oxygen reduction reaction in high temperature proton exchange membrane fuel cells – Long term behavior under ex-situ and in-situ conditions*. Journal of Power Sources, 2014. **266**: p. 313-322.

24.   Huang, Q., et al., *Carbon-supported Pt–Co alloy nanoparticles for oxygen reduction reaction*. Electrochemistry Communications, 2006. **8**(8): p. 1220-1224.

25.   Yang, D., et al., *Highly active and durable Pt–Co nanowire networks catalyst for the oxygen reduction reaction in PEMFCs*. International Journal of Hydrogen Energy, 2016. **41**(41): p. 18592-18601.

26.   Todoroki, N., et al., *Pt–Ni Nanoparticle-Stacking Thin Film: Highly Active Electrocatalysts for Oxygen Reduction Reaction*. ACS Catalysis, 2015. **5**(4): p. 2209-2212.

27.   Fu, S., et al., *Three-dimensional PtNi hollow nanochains as an enhanced electrocatalyst for the oxygen reduction reaction*. Journal of Materials Chemistry A, 2016. **4**(22): p. 8755-8761.

28.   Santos, L.G.R.A., et al., *Oxygen reduction reaction in acid medium on Pt–Ni/C prepared by a microemulsion method*. Journal of Electroanalytical Chemistry, 2006. **596**(2): p. 141-148.

29.   Chung, D.Y., et al., *Highly Durable and Active PtFe Nanocatalyst for Electrochemical Oxygen Reduction Reaction*. Journal of the American Chemical Society, 2015. **137**(49): p. 15478-15485.

30.   Li, W., et al., *Nano-stuctured Pt–Fe/C as cathode catalyst in direct methanol fuel cell*. Electrochimica Acta, 2004. **49**(7): p. 1045-1055.

31.   Du, X.X., et al., *Fine-grained and fully ordered intermetallic PtFe catalysts with largely enhanced catalytic activity and durability*. Energy & Environmental Science, 2016. **9**(8): p. 2623-2632.

32.   Wang, Y.-J., et al., *A highly efficient PtCo/C electrocatalyst for the oxygen reduction reaction*. RSC Advances, 2016. **6**(41): p. 34484-34491.

33.   Antolini, E., *Palladium in fuel cell catalysis*. Energy & Environmental Science, 2009. **2**(9).

34.   Wang, B., *Recent development of non-platinum catalysts for oxygen reduction reaction*. Journal of Power Sources, 2005. **152**: p. 1-15.

35.   Ben Liew, K., et al., *Non-Pt catalyst as oxygen reduction reaction in microbial fuel cells: A review*. International Journal of Hydrogen Energy, 2014. **39**(10): p. 4870-4883.

36.   Zhang, J., Z. Xia, and L. Dai, *Carbon-based electrocatalysts for advanced energy conversion and storage*. Science Advances, 2015. **1**(7).

37.   Alvarez, G.F., et al., *Preparation and characterisation of carbon-supported palladium nanoparticles for oxygen reduction in low temperature PEM fuel cells*. Journal of Applied Electrochemistry, 2011. **41**(8): p. 925-937.

38.   Zhang, R. and W. Chen, *Non-precious Ir-V bimetallic nanoclusters assembled on reduced graphene nanosheets as catalysts for the oxygen reduction reaction*. Journal of Materials Chemistry A, 2013. **1**(37): p. 11457-11464.

39.   Alexeyeva, N., et al., *Kinetics of oxygen reduction on gold nanoparticle/multi-walled carbon nanotube hybrid electrodes in acid media.* Journal of Electroanalytical Chemistry, 2010. **642**(1): p. 6-12.

40.   Lin, C., et al., *Rh nanoparticles supported on ultrathin carbon nanosheets for high-performance oxygen reduction reaction and catalytic hydrogenation.* Nanoscale, 2017. **9**(5): p. 1834-1839.

41.   Li, H., et al., *Nitrogen-doped carbon nanotubes with high activity for oxygen reduction in alkaline media.* International Journal of Hydrogen Energy, 2011. **36**(3): p. 2258-2265.

42.   Ryoo, R., et al., *Ordered Mesoporous Carbons.* Advanced Materials, 2001. **13**(9): p. 677-681.

43.   Wong, W.Y., et al., *Nitrogen-containing carbon nanotubes as cathodic catalysts for proton exchange membrane fuel cells.* Diamond and Related Materials, 2012. **22**(0): p. 12-22.

44.   Wu, G., et al., *High-Performance Electrocatalysts for Oxygen Reduction Derived from Polyaniline, Iron, and Cobalt.* Science, 2011. **332**(6028): p. 443-447.

45.   Costentin, C., H. Dridi, and J.-M. Savéant, *Molecular Catalysis of O2 Reduction by Iron Porphyrins in Water: Heterogeneous versus Homogeneous Pathways.* Journal of the American Chemical Society, 2015. **137**(42): p. 13535-13544.

46.   Seo, M.H., et al., *Theoretical insight into highly durable iron phthalocyanine derived non-precious catalysts for oxygen reduction reactions.* Journal of Materials Chemistry A, 2014. **2**(46): p. 19707-19716.

47.   Feng, Y., et al., *Chalcogenide metal centers for oxygen reduction reaction: Activity and tolerance.* Electrochimica Acta, 2011. **56**(3): p. 1009-1022.

48.   Cao, D., et al., *Oxygen Reduction Reaction on Ruthenium and Rhodium Nanoparticles Modified with Selenium and Sulfur.* Journal of The Electrochemical Society, 2006. **153**(5): p. A869-A874.

49.   Zhong, H., et al., *A novel non-noble electrocatalyst for PEM fuel cell based on molybdenum nitride.* Electrochemistry Communications, 2006. **8**(5): p. 707-712.

50.   Cao, B., et al., *Molybdenum Nitrides as Oxygen Reduction Reaction Catalysts: Structural and Electrochemical Studies.* Inorganic Chemistry, 2015. **54**(5): p. 2128-2136.

51.   Youn, D.H., et al., *A highly efficient transition metal nitride-based electrocatalyst for oxygen reduction reaction: TiN on a CNT-graphene hybrid support.* Journal of Materials Chemistry A, 2013. **1**(27): p. 8007-8015.

52.   Kielhorn, J., et al., *Palladium – A review of exposure and effects to human health.* International Journal of Hygiene and Environmental Health, 2002. **205**(6): p. 417-432.

53.   Demel, J., J. Čejka, and P. Štěpnička, *The use of palladium nanoparticles supported on MCM-41 mesoporous molecular sieves in Heck reaction: A comparison of basic and neutral supports.* Journal of Molecular Catalysis A: Chemical, 2007. **274**(1–2): p. 127-132.

54.   Machida, K.-i. and M. Enyo, *In Situ X-Ray Diffraction Study of Hydrogen Entry into Pd and Pd-Au Alloy Electrodes during Anodic HCHO Oxidation.* Journal of The Electrochemical Society, 1987. **134**(6): p. 1472-1474.

55.   Mustain, W.E. and J. Prakash, *Kinetics and mechanism for the oxygen reduction reaction on polycrystalline cobalt–palladium electrocatalysts in acid media.* Journal of Power Sources, 2007. **170**(1): p. 28-37.

56.   Chaston, J.C. and E.J. Sercombe, *Palladium-on-Charcoal Catalysts: SOME EFFECTS OF VARIABLES ON HYDROGENATION ACTIVITY.* Platinum Metal Reviews, 1961. **5**(4): p. 122-125.

57.   Moreira, J., et al., *Synthesis, characterization and application of a Pd/Vulcan and Pd/C catalyst in a PEM fuel cell.* International Journal of Hydrogen Energy, 2004. **29**(9): p. 915-920.

58.   Savadogo, O., et al., *New palladium alloys catalyst for the oxygen reduction reaction in an acid medium.* Electrochemistry Communications, 2004. **6**(2): p. 105-109.

59.   Fernández, J.L., et al., *Pd−Ti and Pd−Co−Au Electrocatalysts as a Replacement for Platinum for Oxygen Reduction in Proton Exchange Membrane Fuel Cells.* Journal of the American Chemical Society, 2005. **127**(38): p. 13100-13101.

60.   Raghuveer, V., P.J. Ferreira, and A. Manthiram, *Comparison of Pd–Co–Au electrocatalysts prepared by conventional borohydride and microemulsion methods for oxygen reduction in fuel cells.* Electrochemistry Communications, 2006. **8**(5): p. 807-814.

61.   Mustain, W.E., K. Kepler, and J. Prakash, *Investigations of carbon-supported CoPd3 catalysts as oxygen cathodes in PEM fuel cells.* Electrochemistry Communications, 2006. **8**(3): p. 406-410.

62.   Zhang, L., K. Lee, and J. Zhang, *Effect of synthetic reducing agents on morphology and ORR activity of carbon-supported nano-Pd–Co alloy electrocatalysts.* Electrochimica Acta, 2007. **52**(28): p. 7964-7971.

63.   Shao, M., *Palladium-based electrocatalysts for hydrogen oxidation and oxygen reduction reactions.* Journal of Power Sources, 2011. **196**(5): p. 2433-2444.

64.   Shao, M.-H., K. Sasaki, and R.R. Adzic, *Pd−Fe Nanoparticles as Electrocatalysts for Oxygen Reduction.* Journal of the American Chemical Society, 2006. **128**(11): p. 3526-3527.

65.   Tarasevich, M.R., et al., *Oxygen kinetics and mechanism at electrocatalysts on the base of palladium–iron system.* Electrochimica Acta, 2007. **52**(15): p. 5108-5118.

66.   Wang, X., et al., *Bimetallic Pd--Cu Oxygen Reduction Electrocatalysts.* Journal of The Electrochemical Society, 2008. **155**(6): p. B602-B609.

67.   Fouda-Onana, F., S. Bah, and O. Savadogo, *Palladium–copper alloys as catalysts for the oxygen reduction reaction in an acidic media I: Correlation between the ORR kinetic parameters and intrinsic physical properties of the alloys.* Journal of Electroanalytical Chemistry, 2009. **636**(1–2): p. 1-9.

68.   Xu, C., et al., *Nanotubular Mesoporous PdCu Bimetallic Electrocatalysts toward Oxygen Reduction Reaction.* Chemistry of Materials, 2009. **21**(14): p. 3110-3116.

69.   Walsh, D.A., J.L. Fernandez, and A.J. Bard, *Rapid Screening of Bimetallic Electrocatalysts for Oxygen Reduction in Acidic Media by Scanning Electrochemical Microscopy.* Journal of The Electrochemical Society, 2006. **153**(6): p. E99-E103.

70.   Fernández, J.L., D.A. Walsh, and A.J. Bard, *Thermodynamic Guidelines for the Design of Bimetallic Catalysts for Oxygen Electroreduction and Rapid Screening by Scanning Electrochemical Microscopy. M−Co (M: Pd, Ag, Au).* Journal of the American Chemical Society, 2004. **127**(1): p. 357-365.

71.   Ang, S.-Y. and D.A. Walsh, *Palladium–vanadium alloy electrocatalysts for oxygen reduction: Effect of heat treatment on electrocatalytic activity and stability.* Applied Catalysis B: Environmental, 2010. **98**(1–2): p. 49-56.

72.   Grdeń, M., et al., *Electrochemical behaviour of palladium electrode: Oxidation, electrodissolution and ionic adsorption.* Electrochimica Acta, 2008. **53**(26): p. 7583-7598.

73.   Rand, D.A.J. and R. Woods, *A study of the dissolution of platinum, palladium, rhodium and gold electrodes in 1 m sulphuric acid by cyclic voltammetry.* Journal of Electroanalytical Chemistry and Interfacial Electrochemistry, 1972. **35**(1): p. 209-218.

74.   Solomun, T., *The role of the electrolyte anion in anodic dissolution of the Pd(100) surface.* Journal of Electroanalytical Chemistry and Interfacial Electrochemistry, 1991. **302**(1): p. 31-46.

75. Juodkazis, K., et al., *Anodic Dissolution of Palladium in Sulfuric Acid: An Electrochemical Quartz Crystal Microbalance Study.* Russian Journal of Electrochemistry, 2003. **39**(9): p. 954-959.

76. McCafferty, E., *Thermodynamics of Corrosion: Pourbaix Diagrams*, in *Introduction to Corrosion Science*, E. McCafferty, Editor. 2010, Springer New York: New York, NY. p. 95-117.

77. Hsieh, B.-J., et al., *Platinum loaded on dual-doped TiO2 as an active and durable oxygen reduction reaction catalyst.* Npg Asia Materials, 2017. **9**: p. e403.

78. Finkelstein, N.P. and R.D. Hancock, *A new approach to the chemistry of gold.* Gold Bulletin, 1974. **7**(3): p. 72-77.

79. Pourbaix, M.J.N. and J.V. Muylder, *Electrochemical Properties of the Platinum Metals.* Platinum Metals Rev., 1959. **3**(2): p. 47.

80. Castanheira, L., et al., *Carbon Corrosion in Proton-Exchange Membrane Fuel Cells: Effect of the Carbon Structure, the Degradation Protocol, and the Gas Atmosphere.* ACS Catalysis, 2015. **5**(4): p. 2184-2194.

81. Shanmugam, S. and A. Gedanken, *Carbon-Coated Anatase TiO2 Nanocomposite as a High-Performance Electrocatalyst Support.* Small, 2007. **3**(7): p. 1189-1193.

82. M. Bhola, S. and B. Mishra, *Effect of ph on the electrochemical properties of oxides formed over β - Ti-15Mo and mixed Ti-6Al-4v alloys.* Int. J. Electrochem. Sci., 2013. **8**: p. 7075-7087.

83. Müllner, M., et al., *Self-Limiting Adsorption of WO3 Oligomers on Oxide Substrates in Solution.* The Journal of Physical Chemistry C, 2017. **121**(36): p. 19743-19750.

84. Banham, D., et al., *Effect of carbon support nanostructure on the oxygen reduction activity of Pt/C catalysts.* Journal of Materials Chemistry A, 2013. **1**(8): p. 2812-2820.

85. Antolini, E., *Carbon supports for low-temperature fuel cell catalysts.* Applied Catalysis B: Environmental, 2009. **88**(1–2): p. 1-24.

86. Ruiz Camacho, B., et al., *Enhancing oxygen reduction reaction activity and stability of platinum via oxide-carbon composites.* Catalysis Today, 2013. **202**: p. 36-43.

87. Li, W. and A.M. Lane, *Investigation of Pt catalytic effects on carbon support corrosion of the cathode catalyst in PEM fuel cells using DEMS spectra.* Electrochemistry Communications, 2009. **11**(6): p. 1187-1190.

88. Sun, X. and M.S. Saha, *Nanotubes, Nanofibers and Nanowires as Supports for Catalysts*, in *PEM Fuel Cell Electrocatalysts and Catalyst Layers: Fundamentals and Applications*, J. Zhang, Editor. 2008, Springer. p. 654-700.

89. Gunji, T., et al., *Enhanced Oxygen Reduction Reactions and Stable Long-term Activity on TiO2-supported Dealloyed PtCu Nanoparticles in Acidic Aqueous Solutions.* ECS Transactions, 2015. **66**(39): p. 1-8.

90. Estudillo-Wong, L.A., et al., *Enhanced oxygen reduction reaction stability on platinum nanoparticles photo-deposited onto oxide-carbon composites.* Applied Catalysis B: Environmental, 2016. **187**: p. 291-300.

91. Xu, W., Z. Wu, and S. Tao, *Recent progress in electrocatalysts with mesoporous structures for application in polymer electrolyte membrane fuel cells.* Journal of Materials Chemistry A, 2016. **4**(42): p. 16272-16287.

92. Guo, D.-J. and H.-L. Li, *High dispersion and electrocatalytic properties of palladium nanoparticles on single-walled carbon nanotubes.* Journal of Colloid and Interface Science, 2005. **286**(1): p. 274-279.

93. Smirnova, A., et al., *Novel carbon aerogel-supported catalysts for PEM fuel cell application.* International Journal of Hydrogen Energy, 2005. **30**(2): p. 149-158.

94. Liu, S.-H., et al., *Fabrication and electrocatalytic performance of highly stable and active platinum nanoparticles supported on nitrogen-doped ordered mesoporous carbons for oxygen reduction reaction.* Journal of Materials Chemistry, 2011. **21**(33): p. 12489-12496.

95.   Tripković, V., et al., *Metal Oxide-Supported Platinum Overlayers as Proton-Exchange Membrane Fuel Cell Cathodes.* ChemCatChem, 2012. **4**(2): p. 228-235.

96.   Liu, X., X. Wu, and K. Scott, *Study of niobium and tantalum doped titania-supported Pt electrocatalysts for methanol oxidation and oxygen reduction reactions.* Catalysis Science & Technology, 2014. **4**(11): p. 3891-3898.

97.   Zhu, W., et al., *Nanocrystalline tungsten carbide (WC) synthesis/characterization and its possible application as a PEM fuel cell catalyst support.* Electrochimica Acta, 2012. **61**(0): p. 198-206.

98.   Suzuki, Y., et al., *Sulfated-Zirconia as a Support of Pt Catalyst for Polymer Electrolyte Fuel Cells.* Electrochemical and Solid-State Letters, 2007. **10**(7): p. B105-B107.

99.   Bish, D.L., *Sample preparation for X-ray diffraction.* Modern Powder Diffraction, 1989.

100.   Birkholz, M., *Principles of X-ray Diffraction*, in *Thin Film Analysis by X-Ray Scattering*. 2006, Wiley-VCH Verlag GmbH & Co. KGaA. p. 1-40.

101.   Post, J.E., *Rietveld refinement of crystal structures using powder X-ray diffraction data.* Modern Powder Diffraction, 1989.

102.   Gregory, N.W., *Elements of X-Ray Diffraction.* Journal of the American Chemical Society, 1957. **79**(7): p. 1773-1774.

103.   Leontyev, I.N., et al., *XRD and electrochemical investigation of particle size effects in platinum-cobalt cathode electrocatalysts for oxygen reduction.* Journal of Alloys and Compounds, 2010. **500**(2): p. 241-246.

104.   Patterson, A.L., *The Scherrer Formula for X-Ray Particle Size Determination.* Physical Review, 1939. **56**(10): p. 978-982.

105.   Crozier, P.A. and T.W. Hansen, *In situ and operando transmission electron microscopy of catalytic materials.* MRS Bulletin, 2015. **40**(1): p. 38-45.

106.   Olivier, E.J. and J.H. Neethling, *TEM analysis of planar defects in β-SiC.* International Journal of Refractory Metals and Hard Materials, 2009. **27**(2): p. 443-448.

107.   Yano, H., et al., *Particle-size effect of nanoscale platinum catalysts in oxygen reduction reaction: an electrochemical and 195Pt EC-NMR study.* Physical Chemistry Chemical Physics, 2006. **8**(42): p. 4932-4939.

108.   Russ, J.C., *Chapter 1 - X-Ray Emission*, in *Fundamentals of Energy Dispersive X-ray Analysis*. 1984, Butterworth-Heinemann. p. 1-9.

109.   Alderucci, V., et al., *XPS study of surface oxidation of carbon-supported Pt catalysts.* Materials Chemistry and Physics, 1995. **41**(1): p. 9-14.

110.   Hofmann, S., *Auger- and X-Ray Photoelectron Spectroscopy in Materials Science.* 2013: Springer Berlin Heidelberg.

111.   Biesinger, M.C., et al., *Resolving surface chemical states in XPS analysis of first row transition metals, oxides and hydroxides: Sc, Ti, V, Cu and Zn.* Applied Surface Science, 2010. **257**(3): p. 887-898.

112.   Malmgren, S., et al., *Consequences of air exposure on the lithiated graphite SEI.* Electrochimica Acta, 2013. **105**: p. 83-91.

113.   Álvarez, G.F., M. Mamlouk, and K. Scott, *An Investigation of Palladium Oxygen Reduction Catalysts for the Direct Methanol Fuel Cell.* International Journal of Electrochemistry, 2011. **2011**: p. 12.

114.   Liu, X., E.H. Yu, and K. Scott, *Preparation and evaluation of a highly stable palladium yttrium platinum core–shell–shell structure catalyst for oxygen reduction reactions.* Applied Catalysis B: Environmental, 2015. **162**: p. 593-601.

115.   Gasteiger, H.A., et al., *Activity benchmarks and requirements for Pt, Pt-alloy, and non-Pt oxygen reduction catalysts for PEMFCs.* Applied Catalysis B: Environmental, 2005. **56**(1–2): p. 9-35.

116. Jirkovský, J.S., et al., *Single Atom Hot-Spots at Au–Pd Nanoalloys for Electrocatalytic H2O2 Production.* Journal of the American Chemical Society, 2011. **133**(48): p. 19432-19441.

117. Sarapuu, A., et al., *Electrochemical reduction of oxygen on thin-film Au electrodes in acid solution.* Electrochemistry Communications, 2001. **3**(8): p. 446-450.

118. Maye, M.M., et al., *Electrocatalytic reduction of oxygen: Gold and gold-platinum nanoparticle catalysts prepared by two-phase protocol.* Gold Bulletin, 2004. **37**(3): p. 217-223.

119. Shao, M.H., et al., *Palladium Monolayer and Palladium Alloy Electrocatalysts for Oxygen Reduction.* Langmuir, 2006. **22**(25): p. 10409-10415.

120. Zhang, J., et al., *Stabilization of Platinum Oxygen-Reduction Electrocatalysts Using Gold Clusters.* Science, 2007. **315**(5809): p. 220-222.

121. Koenigsmann, C., et al., *Size- and Composition-Dependent Enhancement of Electrocatalytic Oxygen Reduction Performance in Ultrathin Palladium–Gold (Pd1–xAux) Nanowires.* The Journal of Physical Chemistry C, 2012. **116**(29): p. 15297-15306.

122. Venkateswara Rao, C. and B. Viswanathan, *Microemulsion synthesis and electrocatalytic properties of carbon-supported Pd–Co–Au alloy nanoparticles.* Journal of Colloid and Interface Science, 2012. **367**(1): p. 337-341.

123. Shim, J.H., et al., *Porous Pd Layer-Coated Au Nanoparticles Supported on Carbon: Synthesis and Electrocatalytic Activity for Oxygen Reduction in Acid Media.* Chemistry of Materials, 2011. **23**(21): p. 4694-4700.

124. Chen, C.H., et al., *Palladium and Palladium Gold Catalysts Supported on MWCNTs for Electrooxidation of Formic Acid.* Fuel Cells, 2010. **10**(2): p. 227-233.

125. Ding, Y., et al., *Atomic Structure of Au−Pd Bimetallic Alloyed Nanoparticles.* Journal of the American Chemical Society, 2010. **132**(35): p. 12480-12486.

126. Sasaki, K., et al., *Highly stable Pt monolayer on PdAu nanoparticle electrocatalysts for the oxygen reduction reaction.* Nat Commun, 2012. **3**: p. 1115.

127. Rahul, R., et al., *The role of surface oxygenated-species and adsorbed hydrogen in the oxygen reduction reaction (ORR) mechanism and product selectivity on Pd-based catalysts in acid media.* Physical Chemistry Chemical Physics, 2015. **17**(23): p. 15146-15155.

128. Hsu, C., et al., *Au/Pd core-shell nanoparticles with varied hollow Au cores for enhanced formic acid oxidation.* Nanoscale Research Letters, 2013. **8**(1): p. 113.

129. Zhang, J., et al., *A gold nanoparticle-based chronocoulometric DNA sensor for amplified detection of DNA.* Nat. Protocols, 2007. **2**(11): p. 2888-2895.

130. Łukaszewski, M. and A. Czerwiński, *Selected electrochemical properties of Pd–Au alloys: hydrogen absorption and surface oxidation.* Journal of Solid State Electrochemistry, 2008. **12**(12): p. 1589-1598.

131. Łukaszewski, M. and A. Czerwiński, *Electrochemical behavior of palladium–gold alloys.* Electrochimica Acta, 2003. **48**(17): p. 2435-2445.

132. Xing, Y., et al., *Enhancing Oxygen Reduction Reaction Activity via Pd−Au Alloy Sublayer Mediation of Pt Monolayer Electrocatalysts.* The Journal of Physical Chemistry Letters, 2010. **1**(21): p. 3238-3242.

133. Saipanya, S., S. Lapanantnoppakhun, and T. Sarakonsri, *Electrochemical Deposition of Platinum and Palladium on Gold Nanoparticles Loaded Carbon Nanotube Support for Oxidation Reactions in Fuel Cell.* Journal of Chemistry, 2014. **2014**: p. 6.

134. Erikson, H., et al., *Oxygen Electroreduction on Electrodeposited PdAu Nanoalloys.* Electrocatalysis, 2015. **6**(1): p. 77-85.

135. Damjanovic, A., V. Brusic, and J.O.M. Bockris, *Mechanism of oxygen reduction related to electronic structure of gold-palladium alloy.* The Journal of Physical Chemistry, 1967. **71**(8): p. 2741-2742.

136.   Ju, W., et al., *Palladium Nanoparticles Supported on Highly Oriented Pyrolytic Graphite: Preparation, Reactivity and Stability.* ChemElectroChem, 2015. **2**(4): p. 547-558.

137.   Pires, F.I. and H.M. Villullas, *Pd-based catalysts: Influence of the second metal on their stability and oxygen reduction activity.* International Journal of Hydrogen Energy, 2012. **37**(22): p. 17052-17059.

138.   Shinagawa, T., A.T. Garcia-Esparza, and K. Takanabe, *Insight on Tafel slopes from a microkinetic analysis of aqueous electrocatalysis for energy conversion.* Scientific Reports, 2015. **5**: p. 13801.

139.   Sepa, D.B., et al., *Different views regarding the kinetics and mechanisms of oxygen reduction at Pt and Pd electrodes.* Electrochimica Acta, 1987. **32**(1): p. 129-134.

140.   Holewinski, A. and S. Linic, *Elementary Mechanisms in Electrocatalysis: Revisiting the ORR Tafel Slope.* Journal of The Electrochemical Society, 2012. **159**(11): p. H864-H870.

141.   Oishi, K. and O. Savadogo, *Electrochemical investigation of Pd–Co thin films binary alloy for the oxygen reduction reaction in acid medium.* Journal of Electroanalytical Chemistry, 2013. **703**: p. 108-116.

142.   Hoare, J.P., *Oxygen Overvoltage on Bright Palladium in Acid Solutions.* Journal of The Electrochemical Society, 1965. **112**(11): p. 1129-1133.

143.   Gnanamuthu, D.S. and J.V. Petrocelli, *A Generalized Expression for the Tafel Slope and the Kinetics of Oxygen Reduction on Noble Metals and Alloys.* Journal of The Electrochemical Society, 1967. **114**(10): p. 1036-1041.

144.   Song, W., et al., *Kinetic investigation of oxygen reduction reaction in sub-freezing acid media.* International Journal of Hydrogen Energy, 2008. **33**(18): p. 4844-4848.

145.   Parthasarathy, A., et al., *Temperature Dependence of the Electrode Kinetics of Oxygen Reduction at the Platinum/Nafion® Interface—A Microelectrode Investigation.* Journal of The Electrochemical Society, 1992. **139**(9): p. 2530-2537.

146.   Antoine, O. and R. Durand, *RRDE study of oxygen reduction on Pt nanoparticles inside Nafion®: H2O2 production in PEMFC cathode conditions.* Journal of Applied Electrochemistry. **30**(7): p. 839-844.

147.   Stamenković, V., et al., *Surface Composition Effects in Electrocatalysis: Kinetics of Oxygen Reduction on Well-Defined Pt3Ni and Pt3Co Alloy Surfaces.* The Journal of Physical Chemistry B, 2002. **106**(46): p. 11970-11979.

148.   Senthil Kumar, S.M., et al., *The effect of pretreatment of Vulcan XC-72R carbon on morphology and electrochemical oxygen reduction kinetics of supported Pd nano-particle in acidic electrolyte.* Journal of Electroanalytical Chemistry, 2010. **647**(2): p. 211-221.

149.   Siahrostami, S., et al., *Enabling direct H2O2 production through rational electrocatalyst design.* Nat Mater, 2013. **12**(12): p. 1137-1143.

150.   Li, Z., et al., *Surface segregation of gold for Au/Pd(1 1 1) alloys measured by low-energy electron diffraction and low-energy ion scattering.* Surface Science, 2008. **602**(5): p. 1084-1091.

151.   Wang, D., et al., *Spontaneous incorporation of gold in palladium-based ternary nanoparticles makes durable electrocatalysts for oxygen reduction reaction.* Nature Communications, 2016. **7**: p. 11941.

152.   Pizzutilo, E., et al., *Addressing stability challenges of using bimetallic electrocatalysts: the case of gold-palladium nanoalloys.* Catalysis Science & Technology, 2017. **7**(9): p. 1848-1856.

153.   Mittermeier, T., et al., *Activity, Stability and Degradation of Carbon Supported Palladium (Pd/C) Fuel Cell Electrocatalysts for the Oxygen Reduction.* ECS Transactions, 2015. **69**(17): p. 303-313.

154. Negro, E., et al., *Electrocatalytic Activity and Durability of Pt-Decorated Non-Covalently Functionalized Graphitic Structures.* Catalysts, 2015. **5**(3).

155. Tang, Y., et al., *In Situ and Ex Situ Studies on the Degradation of Pd/C Catalyst for Proton Exchange Membrane Fuel Cells.* Journal of Fuel Cell Science and Technology, 2014. **11**(5): p. 051004-051004-7.

156. Solla-Gullón, J., et al., *Synthesis and Electrochemical Decontamination of Platinum-Palladium Nanoparticles Prepared by Water-in-Oil Microemulsion.* Journal of The Electrochemical Society, 2003. **150**(2): p. E104-E109.

157. Cherevko, S., et al., *A Comparative Study on Gold and Platinum Dissolution in Acidic and Alkaline Media.* Journal of The Electrochemical Society, 2014. **161**(12): p. H822-H830.

158. Chen, D., et al., *Core-shell Au@Pd nanoparticles with enhanced catalytic activity for oxygen reduction reaction via core-shell Au@Ag/Pd constructions.* Scientific Reports, 2015. **5**: p. 11949.

159. Kang, Y., et al., *Multimetallic Core/Interlayer/Shell Nanostructures as Advanced Electrocatalysts.* Nano Letters, 2014. **14**(11): p. 6361-6367.

160. Antolini, E., *Iridium As Catalyst and Cocatalyst for Oxygen Evolution/Reduction in Acidic Polymer Electrolyte Membrane Electrolyzers and Fuel Cells.* ACS Catalysis, 2014. **4**(5): p. 1426-1440.

161. Reier, T., M. Oezaslan, and P. Strasser, *Electrocatalytic Oxygen Evolution Reaction (OER) on Ru, Ir, and Pt Catalysts: A Comparative Study of Nanoparticles and Bulk Materials.* ACS Catalysis, 2012. **2**(8): p. 1765-1772.

162. Ioroi, T. and K. Yasuda, *Platinum-Iridium Alloys as Oxygen Reduction Electrocatalysts for Polymer Electrolyte Fuel Cells.* Journal of The Electrochemical Society, 2005. **152**(10): p. A1917-A1924.

163. Antolini, E., *Iridium Application in Low-Temperature Acidic Fuel Cells: Pt-Free Ir-Based Catalysts or Second/Third Promoting Metal in Pt-Based Catalysts?* ChemElectroChem, 2014. **1**(2): p. 318-328.

164. Hwang, S.J., et al., *Facile synthesis of highly active and stable Pt-Ir/C electrocatalysts for oxygen reduction and liquid fuel oxidation reaction.* Chemical Communications, 2010. **46**(44): p. 8401-8403.

165. Hoare, J.P., *Oxygen overvoltage on bright iridium.* Journal of Electroanalytical Chemistry and Interfacial Electrochemistry, 1968. **18**(3): p. 251-259.

166. Yang, D., et al., *Kinetics and electrocatalytic activity of IrCo/C catalysts for oxygen reduction reaction in PEMFC.* International Journal of Hydrogen Energy, 2012. **37**(3): p. 2447-2454.

167. Li, B., et al., *The Mechanism of the Improvement in Catalytic Activity of Ir Modified by V Compared to Pure Ir/C.* ECS Transactions, 2013. **50**(2): p. 1739-1745.

168. Holt-Hindle, P., et al., *Electrocatalytic Activity of Nanoporous Pt – Ir Materials toward Methanol Oxidation and Oxygen Reduction.* Journal of The Electrochemical Society, 2008. **155**(1): p. K5-K9.

169. Wang, C.-H., H.-C. Hsu, and K.-C. Wang, *Iridium-decorated Palladium–Platinum core–shell catalysts for oxygen reduction reaction in proton exchange membrane fuel cell.* Journal of Colloid and Interface Science, 2014. **427**: p. 91-97.

170. Yang, T., et al., *Palladium–iridium nanowires for enhancement of electro-catalytic activity towards oxygen reduction reaction.* Electrochemistry Communications, 2015. **59**: p. 95-99.

171. Yang, T., et al., *Palladium–iridium nanocrystals for enhancement of electrocatalytic activity toward oxygen reduction reaction.* Nano Energy, 2016. **19**: p. 257-268.

172. Alia, S.M., et al., *Activity and Durability of Iridium Nanoparticles in the Oxygen Evolution Reaction.* Journal of The Electrochemical Society, 2016. **163**(11): p. F3105-F3112.

173. Bao, J., et al., *Composition-Dependent Electrocatalytic Activity of Palladium–Iridium Binary Alloy Nanoparticles Supported on the Multiwalled Carbon Nanotubes for the Electro-Oxidation of Formic Acid.* ACS Applied Materials & Interfaces, 2015. **7**(28): p. 15223-15229.

174. Kim, K. and J.-I. Han, *Carbon-supported bimetallic Pd–Ir catalysts for alkaline sulfide oxidation in direct alkaline sulfide fuel cell.* Journal of Applied Electrochemistry, 2015. **45**(6): p. 533-539.

175. Asanova, T.I., et al., *On formation mechanism of Pd–Ir bimetallic nanoparticles through thermal decomposition of [Pd(NH3)4][IrCl6].* Journal of Nanoparticle Research, 2013. **15**(10): p. 1-15.

176. Shafeev, G.A., et al., *Enhanced adherence of area-selective electroless metal plating on insulators.* Journal of Vacuum Science & Technology A, 1996. **14**(2): p. 319-326.

177. Hall, H.Y. and P.M.A. Sherwood, *X-ray photoelectron spectroscopic studies of the iridium electrode system.* Journal of the Chemical Society, Faraday Transactions 1: Physical Chemistry in Condensed Phases, 1984. **80**(1): p. 135-152.

178. Kahk, J.M., et al., *Understanding the Electronic Structure of ${\mathrm{IrO}}_{2}$ Using Hard-X-ray Photoelectron Spectroscopy and Density-Functional Theory.* Physical Review Letters, 2014. **112**(11): p. 117601.

179. You, D.J., et al., *Improvement of activity for oxygen reduction reaction by decoration of Ir on PdCu/C catalyst.* Catalysis Today, 2012. **185**(1): p. 138-142.

180. Lee, K., L. Zhang, and J. Zhang, *IrxCo1−x (x = 0.3–1.0) alloy electrocatalysts, catalytic activities, and methanol tolerance in oxygen reduction reaction.* Journal of Power Sources, 2007. **170**(2): p. 291-296.

181. Damjanovic, A., A. Dey, and J.O.M. Bockris, *Electrode Kinetics of Oxygen Evolution and Dissolution on Rh, Ir, and Pt-Rh Alloy Electrodes.* Journal of The Electrochemical Society, 1966. **113**(7): p. 739-746.

182. Dembinska, B., et al., *Selenourea-assisted synthesis of selenium-modified iridium catalysts: evaluation of their activity toward reduction of oxygen.* Electrochimica Acta, 2015. **185**: p. 162-171.

183. Aricò, A.S., et al., *An XPS study on oxidation states of Pt and its alloys with Co and Cr and its relevance to electroreduction of oxygen.* Applied Surface Science, 2001. **172**(1–2): p. 33-40.

184. Meku, E., et al., *Composition optimization of ternary palladium-iridium-iron alloy catalysts for oxygen reduction reaction in acid medium.* RSC Advances, 2016. **6**(27): p. 22754-22763.

185. Knupp, S.L., et al., *Platinum Monolayer Electrocatalysts for O2 Reduction: Pt Monolayer on Carbon-Supported PdIr Nanoparticles.* Electrocatalysis, 2010. **1**(4): p. 213-223.

186. Taylor, S., et al., *The Effect of Platinum Loading and Surface Morphology on Oxygen Reduction Activity.* Electrocatalysis, 2016. **7**(4): p. 287-296.

187. Ahluwalia, R.K., et al., *Dynamics of Particle Growth and Electrochemical Surface Area Loss due to Platinum Dissolution.* Journal of The Electrochemical Society, 2014. **161**(3): p. F291-F304.

188. Vion-Dury, B., et al., *Determination of Aging Markers and their Use as a Tool to Characterize Pt/C Nanoparticles Degradation Mechanism in Model PEMFC Cathode Environment.* ECS Transactions, 2011. **41**(1): p. 697-708.

189. Zhang, Z., et al., *An overview of metal oxide materials as electrocatalysts and supports for polymer electrolyte fuel cells.* Energy & Environmental Science, 2014. **7**(8): p. 2535-2558.

190. Elezovic, N.R., V.R. Radmilovic, and N.V. Krstajic, *Platinum nanocatalysts on metal oxide based supports for low temperature fuel cell applications.* RSC Advances, 2016. **6**(8): p. 6788-6801.

191. Bonakdarpour, A., et al., *Nanopillar niobium oxides as support structures for oxygen reduction electrocatalysts.* Electrochimica Acta, 2012. **85**(0): p. 492-500.

192. Estudillo-Wong, L.A., et al., *TiO2/C composite as a support for Pd-nanoparticles toward the electrocatalytic oxidation of methanol in alkaline media.* Electrochimica Acta, 2013. **112**: p. 164-170.

193. Kang, E., et al., *Ordered mesoporous WO3-X possessing electronically conductive framework comparable to carbon framework toward long-term stable cathode supports for fuel cells.* Journal of Materials Chemistry, 2010. **20**(35): p. 7416-7421.

194. Zhang, Z., et al., *Pd nanoparticles supported on WO3/C hybrid material as catalyst for oxygen reduction reaction.* Journal of Power Sources, 2008. **185**(2): p. 941-945.

195. Colmenares, J.C., et al., *Influence of the strong metal support interaction effect (SMSI) of Pt/TiO2 and Pd/TiO2 systems in the photocatalytic biohydrogen production from glucose solution.* Catalysis Communications, 2011. **16**(1): p. 1-6.

196. Lewera, A., et al., *Metal–Support Interactions between Nanosized Pt and Metal Oxides (WO3 and TiO2) Studied Using X-ray Photoelectron Spectroscopy.* The Journal of Physical Chemistry C, 2011. **115**(41): p. 20153-20159.

197. Yan, Z., et al., *An ion exchange route to produce WO3 nanobars as Pt electrocatalyst promoter for oxygen reduction reaction.* Journal of Power Sources, 2013. **222**: p. 218-224.

198. Huang, S.-Y., P. Ganesan, and B.N. Popov, *Titania supported platinum catalyst with high electrocatalytic activity and stability for polymer electrolyte membrane fuel cell.* Applied Catalysis B: Environmental, 2011. **102**(1–2): p. 71-77.

199. Huang, S.-Y., P. Ganesan, and B.N. Popov, *Electrocatalytic Activity and Stability of Titania-Supported Platinum–Palladium Electrocatalysts for Polymer Electrolyte Membrane Fuel Cell.* ACS Catalysis, 2012. **2**(5): p. 825-831.

200. Huang, D., et al., *Pt Catalyst Supported within TiO2 Mesoporous Films for Oxygen Reduction Reaction.* Electrochimica Acta, 2014. **130**: p. 97-103.

201. Fu, Y., et al., *Synthesis of Pd/TiO2 nanotubes/Ti for oxygen reduction reaction in acidic solution.* Journal of Power Sources, 2009. **189**(2): p. 982-987.

202. Yu, T.H., et al., *Improved Non-Pt Alloys for the Oxygen Reduction Reaction at Fuel Cell Cathodes Predicted from Quantum Mechanics.* The Journal of Physical Chemistry C, 2010. **114**(26): p. 11527-11533.

203. Li, W., F.-R.F. Fan, and A.J. Bard, *The application of scanning electrochemical microscopy to the discovery of Pd–W electrocatalysts for the oxygen reduction reaction that demonstrate high activity, stability, and methanol tolerance.* Journal of Solid State Electrochemistry, 2012. **16**(7): p. 2563-2568.

204. Li, Z., et al., *A Co3W3C promoted Pd catalyst exhibiting competitive performance over Pt/C catalysts towards the oxygen reduction reaction.* Chemical Communications, 2014. **50**(5): p. 566-568.

205. Park, Y., et al., *Carbon-doped TiO2 photocatalyst synthesized without using an external carbon precursor and the visible light activity.* Applied Catalysis B: Environmental, 2009. **91**(1–2): p. 355-361.

206. Tennakone, K., et al., *TiO 2 and WO 3 semiconductor particles in contact: photochemical reduction of WO 3 to the non-stoichiometric blue form.* Semiconductor Science and Technology, 1992. **7**(3): p. 423.

207. Li, Y., et al., *The effect of titania polymorph on the strong metal-support interaction of Pd/TiO2 catalysts and their application in the liquid phase selective hydrogenation of long chain alkadienes.* Journal of Molecular Catalysis A: Chemical, 2004. **216**(1): p. 107-114.

208. Feng, L., et al., *High activity of Pd–WO3/C catalyst as anodic catalyst for direct formic acid fuel cell.* Journal of Power Sources, 2011. **196**(5): p. 2469-2474.

209. Wiseman, P.J. and P.G. Dickens, *The crystal structure of cubic hydrogen tungsten bronze.* Journal of Solid State Chemistry, 1973. **6**(3): p. 374-377.
210. Sakurai, K. and M. Mizusawa, *X-ray Diffraction Imaging of Anatase and Rutile.* Analytical Chemistry, 2010. **82**(9): p. 3519-3522.
211. Jayaraman, S., et al., *Synthesis and Characterization of Pt−WO3 as Methanol Oxidation Catalysts for Fuel Cells.* The Journal of Physical Chemistry B, 2005. **109**(48): p. 22958-22966.
212. Diebold, U. and T.E. Madey, *TiO2 by XPS.* Surface Science Spectra, 1996. **4**(3): p. 227-231.
213. Liu, Y., S. Shrestha, and W.E. Mustain, *Synthesis of Nanosize Tungsten Oxide and Its Evaluation as an Electrocatalyst Support for Oxygen Reduction in Acid Media.* ACS Catalysis, 2012. **2**(3): p. 456-463.
214. Fabregat-Santiago, F., et al., *Cyclic Voltammetry Studies of Nanoporous Semiconductors. Capacitive and Reactive Properties of Nanocrystalline TiO2 Electrodes in Aqueous Electrolyte.* The Journal of Physical Chemistry B, 2003. **107**(3): p. 758-768.
215. Wolcott, A., et al., *Synthesis and Characterization of Ultrathin WO3 Nanodisks Utilizing Long-Chain Poly(ethylene glycol).* The Journal of Physical Chemistry B, 2006. **110**(50): p. 25288-25296.
216. Choi, M., et al., *Electrochemical Characterization of Nano-Sized Pd-Based Catalysts as Cathode Materials in Direct Methanol Fuel Cells.* Journal of Nanoscience and Nanotechnology, 2011. **11**(1): p. 738-741.
217. Ganesan, P., S. Huang, and B.N. Popov, *Preparation and Characterization of Pt/NbTiO2 Cathode Catalysts for Unitized Regenerative Fuel Cells (URFCs).* ECS Transactions, 2008. **16**(2): p. 1143-1150.
218. Yuan, X., et al., *Ti3+-Promoted High Oxygen-Reduction Activity of Pd Nanodots Supported by Black Titania Nanobelts.* ACS Applied Materials & Interfaces, 2016. **8**(41): p. 27654-27660.
219. Shim, J., et al., *Electrochemical characteristics of Pt–WO3/C and Pt–TiO2/C electrocatalysts in a polymer electrolyte fuel cell.* Journal of Power Sources, 2001. **102**(1–2): p. 172-177.
220. Kulesza, P.J. and L.R. Faulkner, *Reactivity and charge transfer at the tungsten oxide/sulfuric acid interfaces: Nonstoichiometric tungsten(VI,V) oxide films as powerful electroreduction catalysts.* Colloids and Surfaces, 1989. **41**(Supplement C): p. 123-134.
221. Shih, C.-C. and J.-R. Chang, *Pt/C stabilization for catalytic wet-air oxidation: Use of grafted TiO2.* Journal of Catalysis, 2006. **240**(2): p. 137-150.
222. Erikson, H., et al., *Enhanced electrocatalytic activity of cubic Pd nanoparticles towards the oxygen reduction reaction in acid media.* Electrochemistry Communications, 2011. **13**(7): p. 734-737.
223. Lee, A.F., et al., *Structural and Catalytic Properties of Novel Au/Pd Bimetallic Colloid Particles: EXAFS, XRD, and Acetylene Coupling.* The Journal of Physical Chemistry, 1995. **99**(16): p. 6096-6102.
224. Gatalo, M., et al., *Positive Effect of Surface Doping with Au on the Stability of Pt-Based Electrocatalysts.* ACS Catalysis, 2016. **6**(3): p. 1630-1634.
225. Xiao, L., et al., *Activating Pd by Morphology Tailoring for Oxygen Reduction.* Journal of the American Chemical Society, 2009. **131**(2): p. 602-608.
226. Dhanasekaran, P., et al., *Rutile TiO2 Supported Pt as Stable Electrocatalyst for Improved Oxygen Reduction Reaction and Durability in Polymer Electrolyte Fuel Cells.* Electrocatalysis, 2016. **7**(6): p. 495-506.

227. Mazumder, V., et al., *Core/Shell Pd/FePt Nanoparticles as an Active and Durable Catalyst for the Oxygen Reduction Reaction.* Journal of the American Chemical Society, 2010. **132**(23): p. 7848-7849.